The innovative use of the Zero Length Column for the measurement of water vapor adsorption equilibrium and kinetics on mesoporous solids at high relative humidity

Alessio Centineo

THE UNIVERSITY *of* EDINBURGH

Thesis submitted for the degree of

Doctor of Philosophy

University of Edinburgh

School of Engineering

Year of Submission 2018

Declaration

I hereby certify that I have composed this thesis and that the work presented is my own except where indicated. In addition, the work has not been previously submitted for any other degree or professional qualification.

Alessio Centineo

Acknowledgments

I would like to acknowledge the University of Edinburgh, Process Systems Enterprise Ltd and Energy Technology Partnership for funding this work.

I would like to thank my supervisor, Prof Stefano Brandani, for his constant support during this Ph.D. project.

I would like to thank all the technical staff at the School of Engineering of the UoE.

I would like to thank my family and my friends.

Contents

1 Abstract

The present work is an experimental and modeling study aimed to develop the use of the zero-length column (ZLC) technique for adsorption equilibrium and kinetic measurements of condensable vapors on solid adsorbents. Water vapor was used as adsorptive. Two silica-based materials with different pore structure were used as solid adsorbents. The ordered SBA-15 characterized by cylindrical independent pores and the amorphous silica-gel characterized by a disordered pore network.

The decision to use two solid adsorbents, with completely different pore structure and substantially different shape of the isotherm, was dictated by two factors. The first factor is related to the equilibrium and it is aimed to test the capabilities of the ZLC system for the measurement of adsorption-desorption isotherms characterized by different shapes. Due to the complex shape of the water vapor adsorption isotherms on mesoporous materials and due to the presence of a hysteresis loop, the use of these two solids represents a challenging and reliable benchmark for the evaluation of the ZLC capabilities. The second factor is related to the kinetic measurements. SBA-15 permits to study the kinetic transport mechanism of a condensing vapor in a well-defined straight cylindrical pore, meanwhile silica-gel represents a good example for the study of kinetics adsorption in a pore network.

The adsorption-desorption equilibrium isotherms were measured using the ZLC system and validated against a commercial gravimetric system designed for water vapor adsorption measurements. The ZLC system has shown innovative and extraordinary advantages for the measurement of the equilibrium isotherms: a) the possibility to obtain accurate and continuous adsorption-desorption isotherms for complexly shaped isotherms; b) the extremely small amount of time needed to complete an experiment.

The possibility to measure continuous adsorption-desorption isotherms is extremely useful, especially for isotherms characterized by nearly vertical branches as water on SBA-15. In a traditional discontinuous measurement system as the gravimetric or the volumetric systems, an optimal number of single step points is to be chosen to obtain an accurate isotherm. More points are needed in the nearly vertical condensation-evaporation parts of the isotherm and an extremely stable concentration of the gas phase is required to avoid irreversible change of the adsorbed amount.

The ZLC is a continuous measurement system which can potentially be fully automated. A continuous adsorption-desorption isotherm is obtained when switching the feed line from inert to adsorptive or vice versa. The only requirement to be fulfilled is given by the assessment of

the equilibrium control regime. The calculation of the adsorption-desorption isotherm is based on a simple and robust integration of the mass balance in the column which is assumed to be a perfectly mixed cell.

The advantages of the ZLC extend to the measurement of the scanning curves. Continuous adsorption and desorption scanning curves were obtained. The possibility to accurately observe the shape of a scanning curve represents an important advantage for the structural characterization of porous solids. The scanning curves are easily obtained if one considers that the shape of the isotherm can be continuously observed from the response concentration curves of the ZLC. The scanning curves can be measured by switching the feed line at the gas phase concentration chosen as starting point for the scanning curve.

The ZLC is intrinsically faster than the traditional discontinuous techniques. The water adsorption-desorption isotherm on SBA-15 was measured in 36 hours, meanwhile, 9 days were required by the commercial gravimetric system. Consequently, the ZLC technique is one order of magnitude less time consuming than the gravimetric system.

A theoretical analytical model for the adsorption-desorption equilibrium isotherm of vapors on mesoporous solids was formulated. The equilibrium model was designed to consider several possible adsorption mechanisms of vapors in a distribution of cylindrical pores from zero loading up to full saturation of the solid. The model was validated against the experimental data obtained with the different experimental systems. The model can be used for kinetics studies or for process simulations in adsorption columns.

The kinetics of water adsorption and desorption on SBA-15 and silica-gel was studied using the ZLC system. The study was aimed to understand the transport mechanism of condensing water in mesoporous solids. Large concentration steps going from full saturation up to dry solid and vice versa were used for the kinetic study. The adsorption and desorption response concentration curves, measured at different flowrates, were used for the study and the modeling of the adsorption kinetics. A simple theoretical procedure is suggested to assess if the kinetic can be well represented by a linear driving force model or if a more accurate kinetic model is needed.

A linear driving force (LDF) model and several diffusive models were formulated to predict the kinetic response curves of the ZLC for SBA-15 powder and silica-gel pellets. All the models have a concentration-dependent mass transfer coefficient and only one fitting parameter. The Darken equation and the derivative of the equilibrium isotherm were used to correlate the mass transfer coefficients with the amount adsorbed. In this view, the possibility given by the ZLC to obtain a continuous and accurate isotherm is crucial for the correct

prediction of the mass transfer coefficient. Only one parameter is needed to regress the experimental response curves measured at different flowrates for high concentration steps. The LDF model fails to predict the kinetic response curves for water vapor on SBA-15 and silica-gel. The diffusive models can better predict the adsorption kinetics for water on SBA-15 and silica-gel pellets.

2 Lay summary

The present work was aimed to extend the capabilities of the ZLC technique to the measurement of equilibrium and kinetics of condensable vapors on mesoporous solid adsorbents and potentially on any solid adsorbent. The innovative advantages of the ZLC technique are given by the possibility to obtain continuous adsorption-desorption isotherms for complexly shaped isotherms and the intrinsically short experiment duration. These characteristics can potentially be useful in many applications as characterization of porous materials, rapid screening of any solid adsorbent as food, drugs, construction materials, and others.

Due to the significant industrial and commercial interest in water vapor adsorption, it was decided to investigate the potentialities of the ZLC technique for the measurement of the equilibrium and kinetic properties of water vapor on two different mesoporous solids. The materials were first characterized using an independent commercial gravimetric system designed for water vapor adsorption on solid adsorbents. Afterward, the materials were studied using the ZLC technique. The ZLC has permitted to accurately measure the equilibrium adsorption-desorption isotherms and to study the kinetic mechanism for water uptake on SBA-15 and silica-gel.

The present thesis is structured as follow:

- **Chapter 5:** The physical and structural characteristics of the adsorbent materials used in this work are discussed in relation to the different equilibrium and kinetics adsorption properties.
- **Chapter 6:** The different experimental systems used for the adsorption measurements are discussed. The original theoretical assumptions formulated for the development of the ZLC technique are described. The possible control regimes for a ZLC are investigated in relation to the experimental parameters.
- **Chapter 7:** An analytical model for the adsorption-desorption equilibrium isotherm of a condensable vapor on a mesoporous solid is presented. The analytical formulation of the model and the prediction of the experimental data are reported. The theoretical ZLC adsorption and desorption response curves for a type IV equilibrium isotherm are reported and discussed under equilibrium control conditions.

- **Chapter 8:** The equilibrium measurements on SBA-15 and silica-gel are reported. A critical comparison between the gravimetric and the ZLC technique is presented. The advantages of the ZLC technique are discussed and emphasized.
- **Chapter 9:** The kinetic models describing the water adsorption-desorption uptake on the solids are discussed. Several models are investigated for the prediction of water vapor adsorption-desorption kinetics on SBA-15 powder and silica-gel pellets.
- **Chapter 10:** The experimental ZLC response curves under kinetic control conditions are reported for SBA-15 and silica-gel. The predicted response curves for the ZLC, using the kinetic models described in chapter 8, are shown.
- **Chapter 11:** Conclusions.

The key sections of this thesis can be found in Chapters 5, 7, 8 and 9 where the innovative advantages shown by the unprecedented use of the ZLC technique are fully presented and investigated. In Chapters 5 and 7 the experimental ZLC apparatus is described and the measured equilibrium isotherms are compared to the equilibrium isotherm measured on a commercial gravimetric system used as an independent reference. In Chapter 6 two different equilibrium models are derived and presented for the correlation of the adsorption-desorption equilibrium data. The models are capable of nearly-perfectly correlate the experimental equilibrium data for SBA-15 and silica-gel. In Chapters 8 and 9 the advantages of the ZLC are discussed for the measurement of the kinetics uptake. Chapter 5 shows the theoretical prediction of the ZLC response curve under equilibrium control and anticipates the experimental response curves discussed in the following Chapter.

3 Introduction – Carbon Capture

Carbon capture has been considered as a possible near future solution for the mitigation of the CO_2 concentration in the atmosphere and for the reduction of the CO_2 emitted by large industrial sources [1]. Several different capture processes have been proposed and some of them have already been tested and used to successfully capture CO_2 [2,3]. The key challenge of all the proposed technologies is not only to selectively capture CO_2 but also to have high energetic efficiency in the capturing process. This implies that the amount of energy consumed for the capturing process is to be minimized to encourage the addition of the capture units to industrial sources.

Power generation plants have been considered as the most suitable candidates for the application of large-scale carbon capture processes. Adsorption based processes represent a more efficient and flexible alternative to the traditional highly energy intensive processes based on CO_2 absorption by means of amine scrubbing. The flue gases produced by a power plant are always saturated in water vapor which is an intrinsic product of any fuel combustion. When using adsorption processes to selectively capture the CO_2, the presence of water vapor must be considered. Water vapor is a much stronger adsorptive than CO_2 for most of the solid adsorbents used to adsorb CO_2 and even small concentrations of water are sufficient to decrease significantly the selectivity and the capacity of the adsorbents for CO_2. Even in the case of hydrophobic carbon materials, high concentrations of water might lead to a significant decrease in CO_2 adsorption due to the complete filling of the pores with liquid condensed water. Water vapor in the flue gas can easily be condensed in a chiller. However, extremely low temperatures and consequential high cooling costs are needed to significantly reduce the amount of water in the gas stream. A pre-drying stage is therefore needed, and as well as for the CO_2 capture, an adsorption process can represent a cheaper and more flexible solution for the removal of water vapor before the CO_2 adsorption.

4 Introduction – Water vapor adsorption

Water vapor adsorption has already been utilized in the industry for many years as a drying process for wet gasses [4]. However, the commercial applications related to the study of water adsorption are numerous and they include food conservation, drugs preservation, construction materials, adsorption refrigeration cycles and, more recently, the characterization of porous materials.

4.1 Motivations

The interest in water adsorption equilibrium and kinetics related to the food and drug industries is mostly based on the quality and preservation of such products. The attention is focused on the possible physical or chemical modification deriving from the interaction of food or drugs with moisture. Therefore, it is particularly important to clearly investigate both the amount of water retained and the kinetics of water uptake of such products.

Heat pumps based on water adsorption cycles have recently gained interest thanks to the relevant advantages shown when compared to the traditional heat cycles based on CFCs refrigerants [5]. Water adsorption refrigeration cycles are environmentally friendly, and they can use low-grade heat coming from solar energy or waste heat sources. Water is used as the refrigerant fluid in a thermodynamic cycle in which the energy input is given by the heat provided to the solid adsorbent for the regeneration. The cooling power is provided by the latent heat of water. Silica gel has probably been the most common adsorbent used so far. In this scenario, the kinetic properties of water adsorption and desorption on the solid adsorbent are crucial for the correct modeling of continuous cycles and for the estimation of the cooling rate.

The interest in the utilization of water adsorption as an important tool for the surface chemistry and structural characterization of porous solids is quite recent [6]. The characteristics of water are due to the formidable force field of its molecules and to the possibility to form hydrogen bonding. This allows water to strongly interact with the surface of the solid and therefore it can be utilized as a probe molecule for surface chemistry investigation as well as for pore structure analysis. In addition, water adsorption experiments can be performed at room temperature. To understand the potential advantages of using water adsorption for pore structural characterization one can, for example, consider the typical water adsorption isotherm on a microporous carbon material [7]. Carbon-based materials are prevalently microporous and

either nitrogen or argon, at their respective saturation temperatures, show a type I isotherm. Water, instead, shows a type V isotherm with a relevant hysteresis loop due to different adsorption-desorption mechanisms and to capillary condensation. The possibility to have two distinct branches in the equilibrium isotherm potentially offers more elements for a more accurate characterization of the pore structure. The drawback, in this case, is due to the more complex interactions of the water molecules with surface groups. Therefore, a more complex understanding and modeling of the phase behavior of water on a molecular scale is needed for an accurate evaluation, not only of the surface chemistry but also of the pore width and structure.

4.2 How to measure water vapor adsorption

Water vapor adsorption measurements on solid adsorbents can be carried out using different techniques. The easiest method consists in measuring the mass change of a solid adsorbent when exposed to a gas phase in equilibrium with an over-saturated salt solution [8]. This technique is easy to set up, extremely inexpensive and the gas phase can reach extremely stable values of humidity. Nevertheless, the technique is not suitable for accurate measurements. The commercial instruments designed for water adsorption are mostly based on gravimetric or volumetric techniques. These techniques are accurate and well established. They operate in a discontinuous way and single discrete points are collected for the measurement of the equilibrium isotherm. The gravimetric systems are, however, usually fairly time-consuming even when using few mg of sample are used. More than a week is needed for the measurement of a complete adsorption-desorption isotherm on a mesoporous silica-gel with 30 single step points. In addition, it is not straightforward to measure the accurate shape of the isotherm at very low concentrations where the gas phase detectors are not very accurate. The volumetric systems are generally faster due to the intrinsic faster transport mechanism in the gas phase. These systems have better accuracy at low concentrations, but they might suffer a loss of accuracy at high concentrations where the systematic error, accumulated at each measured point, might become relevant. These techniques can also be used for the measurement of the water adsorption and desorption kinetics. However, secondary effects as heat generation, bed diffusion or valve effect are to be carefully avoided for the correct evaluation of the mass transfer coefficient.

Chromatographic techniques have been used for both equilibrium and kinetic measurements [9]. However, these techniques are not as simple as the gravimetric or volumetric ones and a

more complex mathematical modeling is needed to estimate the parameters. A simplified chromatographic technique, introduced as Zero Length Column, was developed for the straightforward measurement of the diffusive time constant of gas adsorptives in microporous solids [10]. The technique has later been extended to the measurement of the equilibrium isotherms for both single and multicomponent gas mixtures [11][12]. However, these works have been limited to the measurement of either linear or type I equilibrium isotherms of gaseous adsorptives in microporous solids.

5 Adsorbent materials

5.1 Introduction

Two silica-based materials with different pore structure and surface chemistry were chosen for the evaluation of the ZLC capabilities in the measurement of equilibrium and kinetic properties for condensable water vapor on mesoporous solids. Both solids were proved to be stable to repeated water vapor adsorption-desorption cycles conducted up to the saturation concentration of water in the solids. Some water strongly reacts with the solids during the first run on a fresh sample and this can be observed from the hysteresis at low concentration and from the increase of the dry weight of the solids after the first run. However, after the first runs both solids showed a near-perfect reproducibility of the adsorption-desorption isotherm. The different pore structure and surface chemistry, which results in a different shape of the equilibrium isotherm and water transport inside the pores, is convenient for the evaluation of the capabilities of the ZLC technique for both equilibrium and kinetic measurements of condensable vapors.

5.2 SBA-15

The ordered structured silica-based mesoporous material SBA-15 was synthesized twenty years ago for the first time [13]. Considering its innovative and promising characteristics, it has been one of the most studied mesoporous solids in the literature [14]. Its synthesis and preparation [15] are well-known, and the material has revealed some interesting differences when compared to the similarly structured precursor MCM-41 (Mobil Composition of Matter-41) [16]. Due to the possibility of obtaining a solid with an ordered structure made of independent cylindrical pores and customized pore size and length [17], SBA-15 has been used and tested for several different studies or applications. Adsorption, gas storage, catalysis, bio-sensing, and drug release are the most common fields in which the solid has been studied and evaluated. The interaction between SBA-15 and either liquid or vapor water has been extensively studied in the literature. These are mostly focused on three aspects: the phase behavior of water confined in mesoporous channels of well-known dimensions, the hydrothermal stability of SBA-15 when exposed to liquid or vapor water and the hydrophobicity-hydrophilicity nature of the solid surface. In this work, firstly, the stability of SBA-15 when exposed to repeated adsorption-desorption cycles up to high relative humidity at three different temperatures is investigated. Secondly, theoretical equilibrium models which

can be used for the prediction and regression of the equilibrium adsorption-desorption isotherm of water on SBA-15 are explored.

The stability of SBA-15 for adsorption applications has been studied under several different conditions, including in the presence of water vapor or when dispersed in liquid water. However, clear indications about the stability of the solid to high relative humidity are still missing. The main reasons might be due to the different procedures used in the synthesis of the solid, which leads to samples with different properties. As a general consideration, the main structure of SBA-15 seems to be stable when exposed to moisture or liquid water especially when compared to the similar structured MCM-41. However, minor modifications of the internal structure are also present in SBA-15. The micro-porosity usually present in SBA-15 samples has been considered as the main cause for the change in the structure of the solid when exposed to liquid water. An increase of the temperature synthesis up to 130 °C will eventually lead to a sample with no micropores and it will avoid a possible restructuring of the structure when the solid is exposed to water [18]. The modifications that affect the structure of SBA-15 in presence of micropores have been studied also at higher liquid and vapor water temperature up to 150 °C. The observed dissolution of silica and consequent re-deposition on the pores walls is present with both vapor and liquid water. However, the process occurs more rapidly in presence of liquid water. In both cases, most of the microporous volume of the material is lost and some water is permanently trapped in the microporous structure [19,20]. The same process of the dissolution of the pore surface silica in water has also been observed at 60 °C. In this case, the dissolution rate of silica in water has been observed to decrease until the dynamic equilibrium between dissolution and deposition is reached [21]. In some cases, repeated cycles of water vapor adsorption-desorption on SBA-15 performed at 5 °C have also shown strong modifications of the mesoporous structure. Not only does the permanently-trapped-in water drastically reduce the microporous volume, but the capillary pressure of liquid water is also responsible for the collapsing of some of the inner walls of the pores. Thus, this process can lead to even more water trapped within the mesoporous volume [22].

Ordered silica-based materials, such as MCM-41 and SBA-15, have been proved to be quite hydrophobic materials. This idea has clearly been demonstrated in a study in which the simultaneous adsorption of water and organic solvents, onto several ordered silica-based materials, has been investigated [23]. In such a study, the organic compound was able to displace the water from the inner surface of the mesopores and even from the smallest pores. The hydrophobicity of these materials depends mainly on the pores size [24,25], and on the superficial concentration of silanol and siloxane groups [26]. The diameter of the mesopores

can be tailored by adjusting the temperature adopted during the synthesis [27]. Whereas, the surface polarity can be tailored either by varying the synthesis conditions [26] or by changing the post-treatment temperature [27]. High post-treatment temperatures up to 500 °C will cause the condensation of the silanol groups and the increase of the hydrophobicity of the solid. This process can be spotted from a decrease in the amount of water adsorbed at low partial pressure [28]. The SBA-15 sample used in this study was prepared according to what reported in [29]. More details on the sample are reported in section 8.1.1.

5.3 Silica-gel

This silica-based material has been used for many decades in the industry and in commercial applications as a desiccant. The advantages of this solid adsorbent are due to the easy and cheap preparation, and to the long-term stability to repeated water adsorption-desorption cycles. Silica-gel is characterized by a disordered structure in which the pores are randomly oriented and interconnected in pore networks. The dimensions of the pores are typically in the range of 2 to 20 nm and this permits the capillary condensation of vapors. The pore structure of this solid is responsible for a pronounced hysteresis loop in which, differently from the SBA-15/water vapor isotherm, the adsorption and desorption branches are not parallel. Pore blocking phenomena and percolation desorption mechanisms, typical of randomly interconnected pores and disordered structures, can be observed and studied from the desorption branch of the isotherm and from the desorption scanning curves [30]. Although silica gel is characterized by the same chemical composition of SBA-15, the surface of the pores shows a substantially higher concentration of hydroxyl groups [25] which make the solid quite hydrophilic. The heat of adsorption of water on silica-gel is less pronounced than the heat of adsorption on the typical molecular sieves or zeolites. However, its pore volume is generally higher and this makes silica-gel as one of the best adsorbents for bulk separation of water vapor from gaseous streams. The silica-gel sample used in this study is a commercial sample acquired from GeeJay Chemicals Ltd. More details on the sample are reported in section 8.1.4.

6 Experimental systems and theory

6.1 Gravimetric systems

Two different gravimetric systems designed for vapor water adsorption were used for the measurement of the water equilibrium isotherms. A QUANTACHROME AQUADYNE DVS and a TA Instruments VTI-SA+ vapor sorption. Both instruments are dynamic vapor sorption systems in which a dry nitrogen flow is continuously mixed with a humid nitrogen flow to reach the desired humidity value. The AQUADYNE claims a weighing resolution of 0.1 μg, RH resolution of 0.1 %, RH accuracy of ±0.8 % at 20 °C and temperature accuracy of ±0.1 °C. The VTI-SA+ claims a weighing sensitivity of 0.1 μg, weighing accuracy of ±0.1 %, weighing precision of ±0.01 %, RH resolution of 0.1 %, RH accuracy of ±1 % and temperature accuracy of ±0.1 °C.

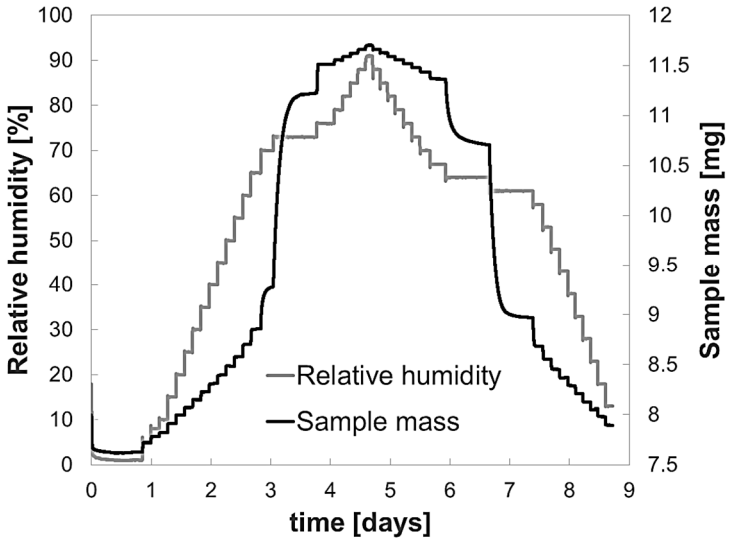

Figure 6.1 – Experimental uptake curves and relative humidity for water *vapor* on SBA-15 at 298K. Sample dry mass 7.6 mg.

For the experiments on the AQUADYNE system, the fresh sample was regenerated at 393K for 3h under vacuum in a separate system and then loaded on the crucible of the gravimetric system. Before starting the run, the sample was then held for 24h under pure nitrogen flow at the same temperature of the experimental run. For the following runs, the sample was regenerated in situ at the same temperature of the experiment and under nitrogen flow. For the experiments conducted on the VTI-SA+ system, the sample was regenerated on the crucible of the instrument at 393K for 3h under a constant flow of pure nitrogen before starting all the experiments. Each water adsorption measurement is fairly time-consuming and the time needed

to complete a measurement was never less than a week as it is possible to observe in fig. 6.1 where the uptake curves for a complete adsorption-desorption cycle on SBA-15 at 298K are reported. For the measurement of a complete adsorption-desorption isotherm on silica-gel beads at 318 K, a similar amount of time is needed as it is possible to observe in fig. 6.2 where the experimental uptake curves obtained on the AQUADYNE system are reported.

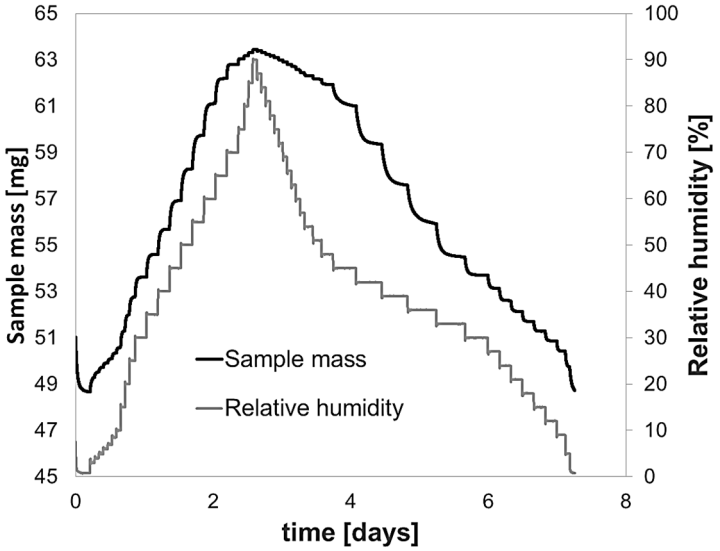

Figure 6.2 – Experimental uptake curves and relative humidity for water vapor on silica-gel at 298K. Sample dry mass 48 mg.

6.2 ZLC system

6.2.1 Introduction

The ZLC technique was initially presented and developed as a fast and reliable chromatographic method for the measurements of the diffusive time constant of adsorptives in microporous solids [10,31]. The evaluation of the diffusive time constant can be achieved through a simple straight-line regression of the long-time asymptote of the experimental desorption data. The main assumptions made for the formulation of the original model are a perfectly mixed gas phase, linear equilibrium isotherm, monodispersed and microcrystalline solid, intracrystalline or microporous diffusion, constant outlet flowrate equal to the carrier flowrate, negligible thermal effects and negligible pressure drops. During the subsequent years, the original model has been extended to take into account the non-linearity of the adsorption isotherm [32,33], bi-p-orous adsorbents [34], solids with particle or crystal size distribution [35] and non-constant outlet flowrate [36,37]. Until now the technique has been extensively and almost exclusively adopted for kinetic measurements. However, a ZLC system can work

both under kinetic control and dynamic equilibrium control and therefore it can provide either mass transfer coefficients or adsorption isotherms. The parameter which is experimentally used to achieve the transition from dynamic equilibrium control to kinetic control is the flowrate of the carrier gas. A simple graphical check showing the experimental desorption concentration curves measured at different flowrates, plotted versus the product of the time and flowrate, can assess whether the system is under equilibrium or kinetic control conditions [38,39].

The ZLC technique has already been modeled and tested for the measurement of the adsorption equilibrium isotherms for single and multicomponent systems [11,40]. Several gases on different microporous solids have been tested. Both linear and type I adsorption isotherms have been measured. The adsorption isotherm can theoretically be calculated in two separate ways. The easiest way consists in integrating the mass balance in Eq. (6.1) using the experimental concentration signal at the outlet of the column. The average amount adsorbed is directly obtained as a function of the gas phase concentration. This method is the most recommended because it provides the adsorption isotherm from a simple and robust integration of the experimental signal. It is also useful when the shape of the isotherm is not known a priori. The other method is based on the simulation and prediction the response of the ZLC system [41]. In such a case, a model for the adsorption equilibrium isotherm in needed in advance. A system of differential equations given by the total mass balance in the system and the mass balance in the solid is to be solved to simulate the gas phase concentration response. Under equilibrium conditions, the shape of the simulated response will depend only on the adsorption isotherm parameters. Therefore, the isotherm parameters are computed from the best regression of the experimental response. For experiments run under diluted conditions, where the adsorption isotherm can be considered linear, the Henry law constant is the only fitting parameter of the model. For the experiments conducted at higher concentration the Langmuir adsorption isotherm has been adopted with the associated parameters b and q_s. It has been demonstrated for both linear and type I isotherms that the ZLC can provide isotherm parameters in good agreement with the parameters measured in the same conditions and on the same solids with independent piezo-metric systems [11]. In addition, it has been possible to observe that the experiments conducted with the ZLC system are quite fast. A complete equilibrium isotherm can be measured in a few minutes. This advantage is due to the continuous way of operating of the chromatographic technique and to the very small amount of solid adsorbent that can be packed in a ZLC system.

In the following paragraphs and chapters, a discussion on the formulation of the ZLC model with particular attention to the experiments performed under equilibrium control conditions is

reported. The experimental part will be introduced with an overview of the modifications of the traditional ZLC experimental system for the adsorption measurements of high concentrated condensable vapors. The experimental results are presented, and the use of a ZLC system for the measurement of the complete adsorption-desorption isotherm of a condensable vapor on mesoporous solids will be discussed. The experimental results include the measurement of the complete water vapor adsorption-desorption isotherm and both adsorption and desorption scanning curves for SBA-15 at 308K and the measurement of the complete water vapor adsorption-desorption isotherm on silica gel at 308K. The geometrical characterization of the experimental system and its dynamic response to a stepwise input in the inlet gas phase concentration is investigated in relation to the amount of sample packed inside the column. The effect of the system dynamic response on the shape of the experimental signal and on the adsorption isotherm is discussed. A numerical deconvolution procedure is suggested for the correction of the experimental signal.

6.2.2 Operating mode

The experimental ZLC apparatus used in this work is as a traditional ZLC system [10,12] which was modified and upgraded to permit adsorption measurements with high concentrated vapors. The schematic flowsheet and a picture of the system with all the relevant sections are shown in figs 6.3-6.3a.

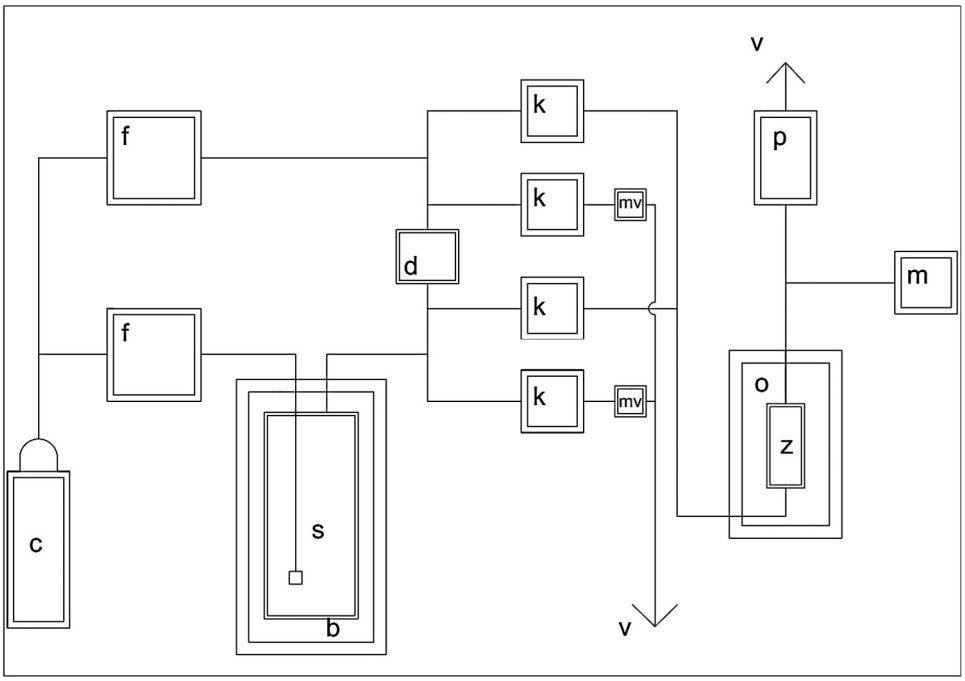

Figure 6.3 – Schematic flowsheet and components of the experimental ZLC system. c gas cylinder; f mass flow controllers; b water bath; s bubbler; d differential pressure transducer; k solenoid switching valve; mv metering valve; v vent; o ZLC oven; z ZLC; p humidity probe; m mass spectrometer;

The carrier gas coming from the gas cylinder was depressurized down to 5 bar and split into two lines going to the two mass flow controllers. The mass flow controller on the top (see fig. 6.3) is used to regulate the desorption flowrate, meanwhile, the mass flow controller on the bottom is used to regulate the adsorption flowrate. The latter is connected to the vapor dosing system represented by a bubbler (Dreschel bottle) filled with distilled water. The bubbler is immersed in a temperature-controlled water bath which is used to set the vapor concentration in the feed line. The dry carrier in the desorption line and the humid stream in the adsorption line are sent to four solenoid valves which operate the switch between adsorption and desorption at the inlet of the adsorption column. Each line is connected to two solenoid valves. For each line, one of the valves leads the flow to the column inlet while the other one directs the flow to a vent. The valves are simultaneously opened or closed in pairs. When two valves open, the other two valves close. If the adsorption line is sent to the column inlet, the desorption line is sent to the vent and *vice versa*. The vents can be connected to cold traps in case organic solvents are used. A differential pressure transducer and two meeting valves are used to equilibrate the pressure between the adsorption and desorption line before switching the valve. This permits one to avoid pressure changes which may condition the flow in the lines and/or alter the experimental signal recorded by the detector. Both detectors are sensitive to total pressure changes. A mass spectrometer and a humidity probe were connected to the column outlet for the measurement of the outlet concentration signal which is the experimentally measured variable.

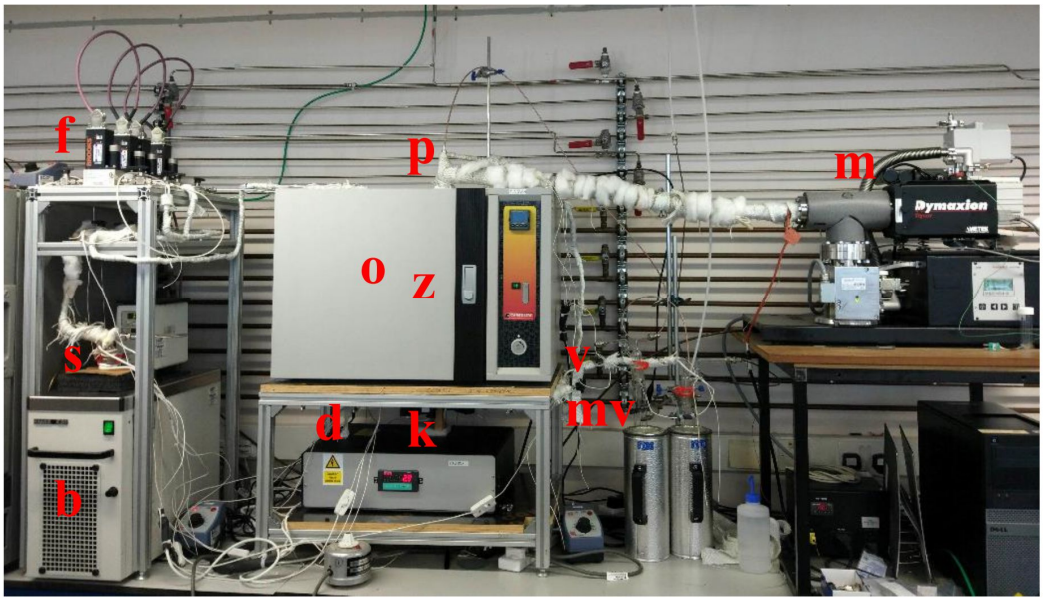

Figure 6.3a – Picture of the ZLC system. f mass flow controllers; b water bath; s bubbler; d differential pressure transducer; k solenoid switching valve; mv metering valve; v vent; o ZLC oven; z ZLC; p humidity probe; m mass spectrometer.

The usual operating procedure initially consists in activating or regenerating the solid with pure inert using the desorption line. When the solid is ready to adsorb, the inlet is switched to the adsorption line containing the humid stream and the solid is saturated for a given amount of time. The inlet is finally switched back to the desorption line and the process is performed until the adsorbed component is fully desorbed and the solid is regenerated. The operating procedure can, however, be changed according to the requirements of the experiment.

6.2.3 Detailed description of the system

All the lines of the ZLC system were made of 1/8-inch SS316L Swagelok tubing. For the connections of the lines, 1/8-inch Swagelok fittings were adopted. The bubbler was a 100 ml Dreschel bottle provided with a sparger and a demister for trapping the eventual droplets carried over by the gas flow. The bubbler was immersed in a HAAKE K20 temperature-controlled bath with a DC30 circulator. The temperature of the bath was used to set the relative humidity of the wet nitrogen at the inlet of the column. Dry nitrogen was used as carrier inert gas. The dry nitrogen flowrate is controlled by two 0-5 ml/min and two 0-250 ml/min SLA5850S BROOK mass flow controllers. All the lines containing humid nitrogen were carefully kept hot by using OMEGA ENGINEERING heating ropes powered by ELECTROTHERMAL MC5 heating controllers. The lines were insulated with fiberglass tape to avoid any condensation of water vapor. Two detectors were used for the analysis of the concentration at the outlet of the ZLC: the first is a quadrupole AMETEK DYCOR DIMAXION mass spectrometer which continuously samples a flowrate of about 0.02 ml/min of gas at the outlet of the ZLC through a silica fused capillary. The second detector is a ROTRONIC HC2-C04 humidity probe connected after the MS capillary and in series with the ZLC. The signal of the MS was used to integrate the mass balance given in Eq. (8.2) in section 8.2.3. The signal of the humidity probe was used to measure the absolute concentration of water at the inlet of the column. This value is relevant for the correct evaluation of the mass balance and for the position of the experimental isotherm respect to the x-axis. In most of the cases, the relative humidity value measured by the humidity probe was about 95% of the equilibrium humidity value expected from the bubbler. The adsorption column is inserted inside a CARBOLITE TYPE 3216 oven which can reach a max temperature of 350 C.

The differential pressure between the adsorption and desorption lines is measured by a GE UNIK 5000 differential pressure transducer. The switch between adsorption and desorption

line is operated by four SHAKO solenoid valves. An independent instrument was used to validate the experimental data obtained with the ZLC.

6.2.4 Equilibrium and kinetic control conditions

In the ZLC (zero length column) technique the length of the packed bed is small enough to consider the gradient of the gas phase concentration along the column practically negligible. In such a scenario the column can be considered as a perfectly mixed tank and the concentration is assumed to be the same in each point of the gas phase. The thermal effects and pressure drop in the columns are assumed negligible. Under these assumptions, the overall mass balance on the adsorptive and on the adsorbed phase inside the column reduces to a quite simple form expressed as:

$$V_s \frac{d\bar{q}}{dt} + V_f \frac{dc}{dt} = F_{in} c_{in} - F_{out} c \tag{6.1}$$

Where $\bar{q}$ is the average concentration of the adsorbed phase on the solid. c is the concentration of the adsorptive in the gas phase. c_{in} and c_{out} are respectively the gas concentrations of the adsorptive at the inlet and at the outlet of the column. V_s is the volume of the solid adsorbent in the column. V_f is the volume of the gas phase in the column. F_{in} and F_{out} are respectively the flowrate at the inlet and at the outlet of the column.

The ZLC system can work either under equilibrium or kinetics control conditions. The ZLC is a dynamic technique in which the concentration of both gas and adsorbed phase are continuously changing. For this reason, the equilibrium is to be interpreted as a series of infinitesimal equilibrium steps. To ensure that the system is working under equilibrium conditions, i.e. the concentration of adsorbed phase is at equilibrium with the concentration of the adsorptive in the gas phase at any time, at least two experiments at different flowrate must be performed. A simple and effective graphical check can be applied [39]. If the experimental desorption curves at different flowrates overlap on a c vs $F_{out}t$ plot (Ft-plot), the amount desorbed, i.e. the area underneath the curves, will only depends on the amount of inert gas passed through the column and the system can be considered under equilibrium conditions. This concept can be demonstrated starting from the mass balance in Eq. (6.1). In a traditional ZLC experiment, a feed stream containing the adsorptive is sent to the column and once the solid is saturated, a stream of pure inert is switched to the column to desorb the amount adsorbed. The mass balance in desorption conditions where $c_{in} = 0$ becomes:

$$V_s \frac{d\bar{q}}{dt} + V_f \frac{dc}{dt} = -F_{out} c \tag{6.2}$$

For the sake of simplicity, a linear isotherm can be considered. Under equilibrium conditions, the average amount adsorbed in the solid can be expressed as:

$$\bar{q} = Kc \tag{6.3}$$

Where K is the Henry's law constant. From the integration of Eq. (6.2) the theoretical response curve of the concentration in the gas phase can be analytical expressed as:

$$ln \frac{c}{c_0} = \frac{-F_{out} t}{KV_s + V_f} \tag{6.4}$$

With the following initial condition:

$$\bar{q}(t_0 = 0) = \bar{q}_0 = Kc_0 \tag{6.5}$$

It is immediately possible to spot that a plot of the $ln\left(\frac{c}{c_0}\right)$ vs $F_{out}t$ will result in a straight line with 1 as intercept and a slope of $-\frac{1}{KV_s+V_f}$. Therefore, under equilibrium conditions, the desorption response curves measured at different flowrates will overlap on a *Ft*-plot showing an equal amount of gas desorbed for the same amount of gas passed through the column. It is also evident from this simple case that under equilibrium control conditions the shape of the response signal will depend only on the shape of the isotherm. In the case of kinetic control conditions, the curves will eventually cross and the total area underneath each curve will remain constant and proportional to the initial amount adsorbed.

The experimental parameter used to switch from equilibrium to kinetic control conditions is the flowrate of the inert gas. This concept has been clearly demonstrated for a ZLC system under the main traditional assumptions of linear isotherm and micropore diffusion in a spherical solid [39]. The physical dimensionless parameter which determines whether the system is under equilibrium or kinetic control is defined by the ratio between the diffusive time constant of the gas in the solid $\frac{R^2}{D}$ and the washout time of the amount adsorbed in the solid $\frac{KV_s}{F}$. This parameter can be expressed as:

$$L = \frac{1}{3} \frac{FR^2}{DKV_s} \tag{6.6}$$

While the ratio between the initial amount of adsorptive in the gas phase and the initial amount in the adsorbed phase is expressed as:

$$\gamma = \frac{1}{3}\frac{V_f}{KV_s} \tag{6.7}$$

From the general analytical solution of a linear ZLC system [31], it is possible to demonstrate that when $L \ll 1$ the solution of the mass balance reduces to Eq. (6.4) and the system can be considered under equilibrium control. Under such conditions, the experimental concentration signal plotted in a $ln\left(\frac{c}{c_0}\right)$ vs time graph reveals the shape of the linear isotherm as a straight line.

This concept is always valid independently on the shape of the equilibrium isotherm. For the sake of simplicity, a ZLC system characterized by the Langmuir adsorption isotherm and a linear driving force model for the transport mechanism of the adsorbate in the solid can be considered. The mass balance in the gas phase was already expressed in Eq. (6.2) and it can be written in dimensionless form as:

$$\frac{d\bar{Q}}{d\tau} + \gamma\frac{dC}{d\tau} = -LC_{out} \tag{6.8}$$

While the mass balance in the solid phase is:

$$\frac{d\bar{Q}}{d\tau} = Q^* - \bar{Q} \tag{6.9}$$

And the Langmuir adsorption isotherm in dimensionless form is:

$$\frac{Q^*}{Q_s^*} = \frac{C}{\beta + C} \tag{6.10}$$

Where:

$$L = \frac{Fc_0}{V_s q_0 k_{ldf}} \tag{6.11}$$

$$\gamma = \frac{V_f c_0}{V_s q_0} \tag{6.12}$$

$$Q = \frac{q}{q_0} \tag{6.13}$$

$$Q^* = \frac{q^*}{q_0} \tag{6.14}$$

$$Q_s^* = \frac{q_s^*}{q_0} \tag{6.15}$$

$$C = \frac{c}{c_0} \tag{6.16}$$

$$\tau = tk_{ldf} \tag{6.17}$$

$$\beta = \frac{1}{bc_0} \tag{6.18}$$

The predicted desorption curve can be simulated with the following initial conditions:

$$C(t = 0) = 1 \tag{6.19}$$

$$Q(t = 0) = 1 \tag{6.20}$$

The parameters Q_s^* and β were chosen in order to give a strong non-linearity to the isotherm as shown in fig. 6.4. This will give a clear curvature to the ZLC simulated desorption curve under equilibrium control conditions. The system of equations can be solved numerically and the desorption curves can be plotted for different values of the L parameter as shown in fig. 6.5. The different values of the L parameter are due to different values of flowrates. The x-axis is scaled in such a way that, at each flowrate, the area under the curves is proportional to the amount of the adsorptive removed from the column divided by the total amount of adsorptive-adsorbate present in the column at the beginning of the desorption. This permits to have a consistent comparison among the curves obtained at different flowrate. The x-axis can therefore be expressed as:

$$\frac{Ftc_0}{V_s q_0 + V_f c_0} \tag{6.21}$$

Or in dimensionless form as:

$$\tau \frac{L}{1+\gamma} \tag{6.22}$$

The use of a linear driving force model allows to clearly show the transition between kinetic control and equilibrium control conditions also for a nonlinear equilibrium isotherm as the Langmuir equation [33]. A more traditional system characterized by a Langmuir isotherm and micropore diffusion kinetic model could have been considered in a similar manner [32]. However, in such a case the desorption curves will maintain almost the same shape when moving from kinetic control to equilibrium control conditions. Therefore, the system with the LDF model permits to more easily understand how to correlate the shape of the equilibrium isotherm with the shape of the experimental response curve.

The transition from kinetic to equilibrium control conditions respectively from higher values to lower values of the L parameter can be graphically spotted in fig. 6.5 from two main aspects. Firstly the disappearance of the “knee” typical of the linear driving force model. Secondly the

overlapping of the curves for values of $L < 1$. Therefore it is quite clear that, although the validation of the equilibrium control condition has historically been demonstrated for linear systems, the equilibrium approach and the graphical check will still be valid for any kind on equilibrium relationship.

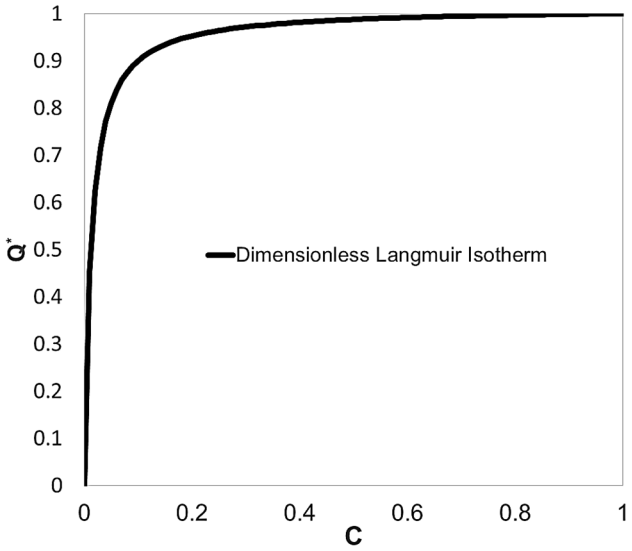

Figure 6.4 – Dimensionless Langmuir isotherm used for the simulation of the ZLC desorption curves.

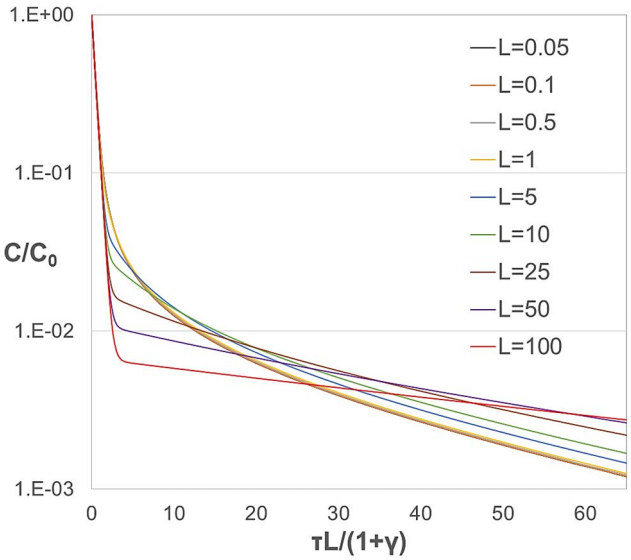

Figure 6.5 – Simulated ZLC desorption curves at different flowrates using the Langmuir model for the equilibrium isotherm and the linear driving force model for the kinetics.

The advantage of plotting the y-axis in logarithmic scale rather than in linear scale is useful when running both kinetic and equilibrium experiments. The magnification effect at low values of concentration and at longer times allows a more accurate extrapolation of the slope of the long-time asymptote which gives the diffusive time constant of the gas molecule into the solid. The advantage is also relevant when performing runs under equilibrium control conditions. The logarithmic scale permits to spot a priori the shape of the equilibrium isotherm. Therefore, the

experimental signal will eventually be linear for linear isotherm and in general it will show the same shape of the equilibrium isotherm.

The same analysis can be done using a more complex adsorption isotherm as the BET model. This will allow the reader to clearly identify the shape of the equilibrium isotherm from the ZLC simulated desorption curves obtained under equilibrium control conditions. This time the simulations were always performed under equilibrium control conditions and the starting point on the adsorption isotherm was changed in order to show the correspondent change in the shape of the simulated desorption curve. The typical shape of the BET isotherm is a good example to show a typical response curve of a ZLC system under equilibrium control conditions for different initial concentrations. In fig. 6.6, the BET adsorption isotherm is shown for different starting points in the dimensionless and normalized form which can be expressed as:

$$\frac{Q^*}{Q_m^*} = \frac{\beta_{BET}\, C}{(1-c_0 C)[1+(\beta_{BET}-c_0)C]} \tag{6.23}$$

Where:

$$Q_m^* = \frac{q_m^*}{q_0} \tag{6.24}$$

$$C = \frac{c}{c_0} \tag{6.25}$$

$$\beta_{BET} = C_{BET} c_0 \tag{6.26}$$

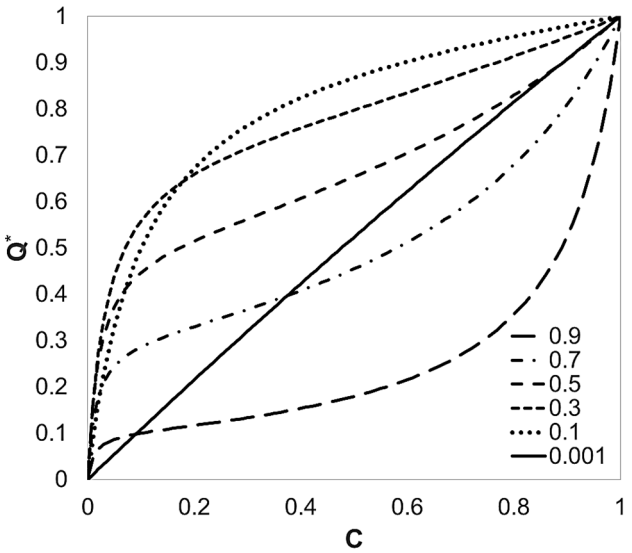

Figure 6.6 – Dimensionless BET isotherm with different initial concentration used for the simulation of the ZLC desorption curves.

In this case, the L and γ parameters will change because of the different initial concentrations in the gas and adsorbed phase. In order to plot the simulated desorption curves in the same plot,

consistently with the initial amount adsorbed, the L parameters should be kept constant by changing the k_{ldf} value. This can be avoided by simply running the simulation with the same value of L and then by expressing the x-axis in fig. 6.7 as $\tau L q_0$. In such a way the area below the curves is proportional to the initial amount adsorbed for each different starting point. A magnification at low times of fig. 6.7 is reported in fig. 6.8 in order to visualize the linearization of the predicted response curve when approaching linear equilibrium isotherm.

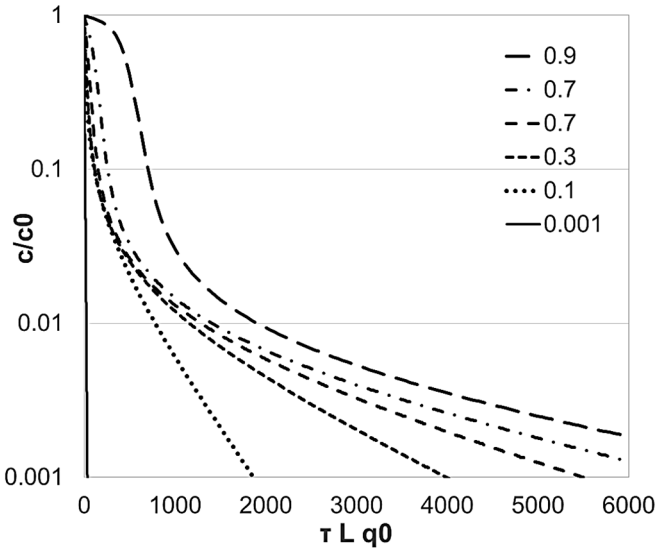

Figure 6.7 – Simulated ZLC desorption curves using the BET model for the equilibrium (see fig. 6.6) and the linear driving force for the kinetics. The curves are simulated under equilibrium control conditions.

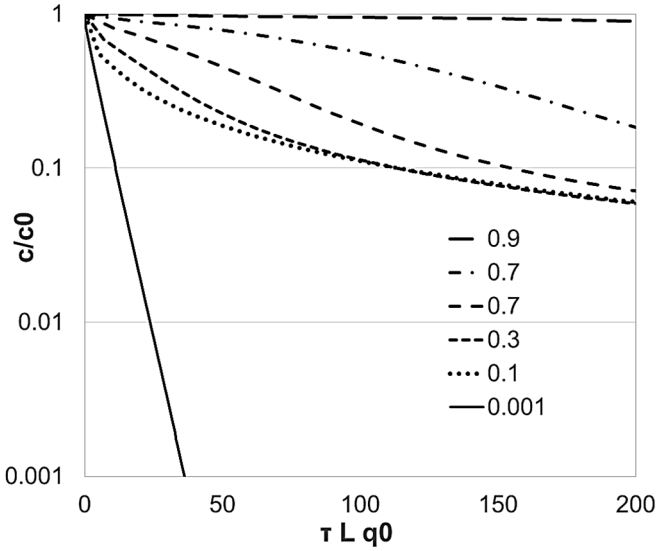

Figure 6.8 – Magnification of fig. 6.7 at low times. The linearity of the isotherm can be better observed.

The BET isotherm permits to simulate alternatively type II, type I and linear isotherm by changing the initial concentration in the gas phase. The effect of the starting point of the equilibrium isotherm is quite evident in fig. 6.7 where the shape of the isotherm can be spotted in advance from the shape of the desorption curves. It can be seen from fig. 6.7 how the

desorption curves change from an s-shaped curve with two inflection points for an initial relative concentration in the gas phase of 0.9 to an almost linear desorption curve for a starting concentration of 0.001.

A step forward can be achieved by simulating the ZLC adsorption and desorption curves for a type IV isotherm under equilibrium conditions. This case is analyzed for a better understanding of the experiments carried out in this project. For the sake of simplicity, the linear driving force model can be assumed for the transport mechanism of the adsorbate. Indeed, any kinetic model will lead to the same results if the system is run under equilibrium control. The adsorption-desorption equilibrium model adopted for the simulation is presented in chapter 6. This case probably represents one of the best examples due to the complex shape of the equilibrium isotherm and due to the presence of a hysteresis loop which provides two different paths for adsorption and desorption. The mass balance in the gas phase was already expressed in Eq. (6.2) in dimensionless form as:

$$\frac{d\bar{Q}}{d\tau} + \gamma \frac{dC}{d\tau} = -LC \tag{6.27}$$

While the mass balance in the solid phase was expressed in Eq. (6.9) as:

$$\frac{d\bar{Q}}{d\tau} = Q^* - \bar{Q} \tag{6.28}$$

As seen beforehand, in the case of nonlinear isotherm, the L and γ parameters are to be slightly redefined. However, their physical meaning remains the same as expressed beforehand. The flowrate was calculated according to Eq. (6.32). The dimensionless parameters, in this case, are defined as well as they were defined before for a Langmuir isotherm as:

$$L = \frac{Fc_0}{k_{ldf} V_s q_0} \tag{6.29}$$

$$\gamma = \frac{V_f c_0}{V_s q_0} \tag{6.30}$$

$$\tau = t k_{ldf} \tag{6.31}$$

Where c_0 is the initial concentration in the gas phase. q_0 is the initial concentration of the adsorbed phase. k_{ldf} is the linear driving force coefficient. The equilibrium isotherm and the simulated ZLC experiment are shown respectively in fig. 6.9 and fig. 6.10. The shape of the predicted ZLC curves is clearly related to the shape of the equilibrium isotherm. The almost horizontal parts in the adsorption and desorption curves correspond to the almost vertical condensation and evaporation branches of the equilibrium isotherm.

The hysteresis loop can, therefore, be spotted from the different position respect to the y-axis of the horizontal parts in the predicted adsorption and desorption curves. For the qualitative evaluation of the Henry law constant, the first part of the adsorption curve can be used. Alternatively, a semi-log plot of the desorption curve will provide the experimental value of the Henry law constant from the long-time slope of the signal.

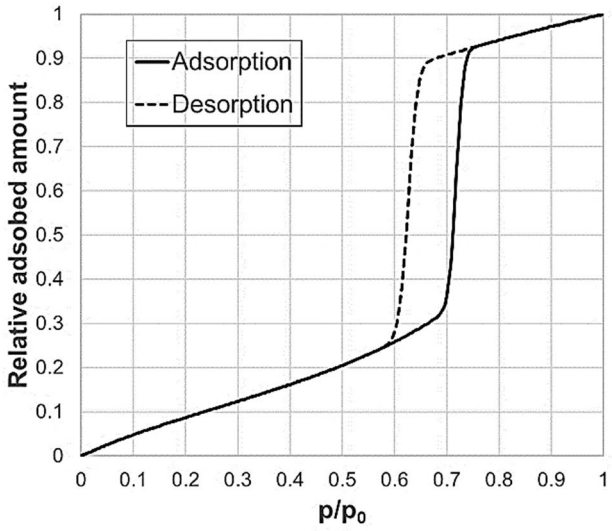

Figure 6.9 – Type IV adsorption-desorption equilibrium isotherm used to run the ZLC simulation.

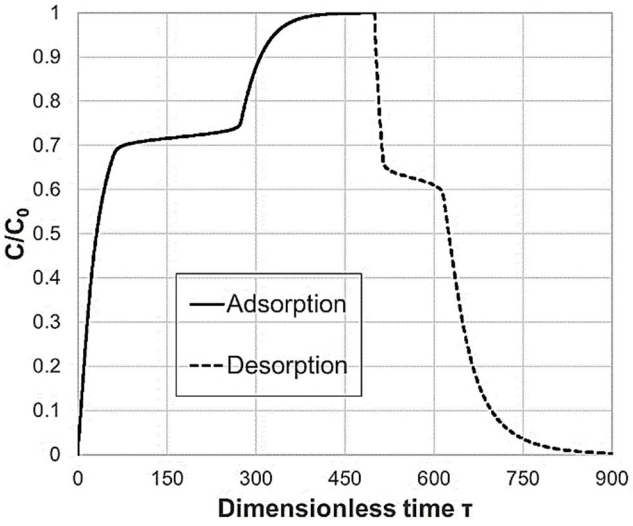

Figure 6.10 – Simulation of the ZLC adsorption and desorption response curves under equilibrium control conditions for a type IV isotherm. The isotherm model shown in fig. 6.9 was used for the simulation.

6.2.5 Flowrate corrections

For the calculation of the mass balance reported in Eq. (6.2), it must be considered that the flowrate at the outlet of the column is generally not constant and it can be assumed constant only under diluted conditions. In the literature, many different approaches have been used for the approximation of the outlet flowrate [11,36,37]. The simplest approximation for the outlet

flowrate assumes that the inert mass flowrate entering the column is equal to the inert mass flowrate leaving the column. Following this approach, the outlet mass flowrate can be expressed as:

$$F_{out}(t) = \frac{F_{in}(1-y_{in})}{1-y(t)} = \frac{F_{in}(1-y_{in})}{1-C_{norm}(t)y_0} \tag{6.32}$$

A different approximation of the flowrate which has been used for the calculation of the correct Henry law constant from breakthrough experiments is the $\Delta F_{carrier}$ approximation [36]. In this case, it was assumed that the change in the carrier flowrate along the column monotonically decreases to zero as the outlet gas concentration reaches the value of concentration at the inlet of the column, i.e. the gas is fully adsorbed or desorbed in the column. This can be expressed as:

$$\Delta F_{carrier} = -V_f(y_{in} - y_0)\frac{y-y_{in}}{\int_0^{\infty}(y-y_{in})dt} \tag{6.33}$$

The total flowrate at the outlet of the column is expressed as:

$$F_{out} = \frac{F_{in}(1-y_{in})+\Delta F_{carrier}}{1-y} \tag{6.34}$$

This expression is still an approximation of the exact value of F_{out} and it might not be valid under all the experimental conditions and very large steps of concentration. If the carrier gas is a pure inert and does not adsorb, the complete mass balance on the carrier in a ZLC can be written as:

$$F_{in}c_{in} - F_{out}c_{out} = V_f\frac{dc_{out}}{dt} \tag{6.35}$$

For a ZLC system the temperature and the pressure change between the inlet and the outlet can be considered negligible, i.e. the total concentration does not change along the column. Therefore, the mass balance on the carrier gas becomes:

$$F_{in}y_{in}^{carrier} - F_{out}y_{out}^{carrier} = V_f\frac{dy_{out}^{carrier}}{dt} \tag{6.36}$$

For a desorption experiment $y_{in}^{carrier} = 1$ and for a two components system in which $y_{out}^{carrier} = 1 - y$ the outlet flowrate can be expressed as:

$$F_{out} = \frac{F_{in}}{1-y} - V_f\frac{dln(1-y)}{dt} = \frac{F_{in}}{1-y} + \frac{V_f}{1-y}\frac{dy}{dt} \tag{6.37}$$

While for an adsorption experiment:

$$F_{out} = \frac{F_{in}(1-y_{in})}{1-y} - V_f \frac{dln(1-y)}{dt} = \frac{F_{in}(1-y_{in})}{1-y} + \frac{V_f}{1-y}\frac{dy}{dt} \quad (6.38)$$

From this expression, it results immediately clear that the difference between Eq. (6.38) and Eq. (6.32) can be observed in case of high concentration of the gas phase and for rapid gas phase concentration changes. It is theoretically possible to investigate the difference on the computed isotherm when using all the flowrate corrections mentioned so far. In doing this the simulated data points shown in fig. 6.10 were used for the integration of the mass balance given in Eq. (6.1). In this analysis, the approximation of the outlet flowrate for diluted systems was also considered. This can be expressed as:

$$F_{out} = F_{in} \quad (6.39)$$

In this theoretical analysis, the molar fraction of water in the feed stream is 3% which is also the feed molar fraction of water in the experimental runs presented in this work. From fig. 6.11 it is possible to notice that all the correlations used for F_{out} give almost the same isotherm at low values of concentration as expected. The constant flowrate correlation in Eq. (6.39) diverges significantly only at high values of concentrations while the other correlations are quite well matched in all the range of concentrations. Therefore, for the calculation of the isotherms, it was decided to use the correlation in Eq. (6.32).

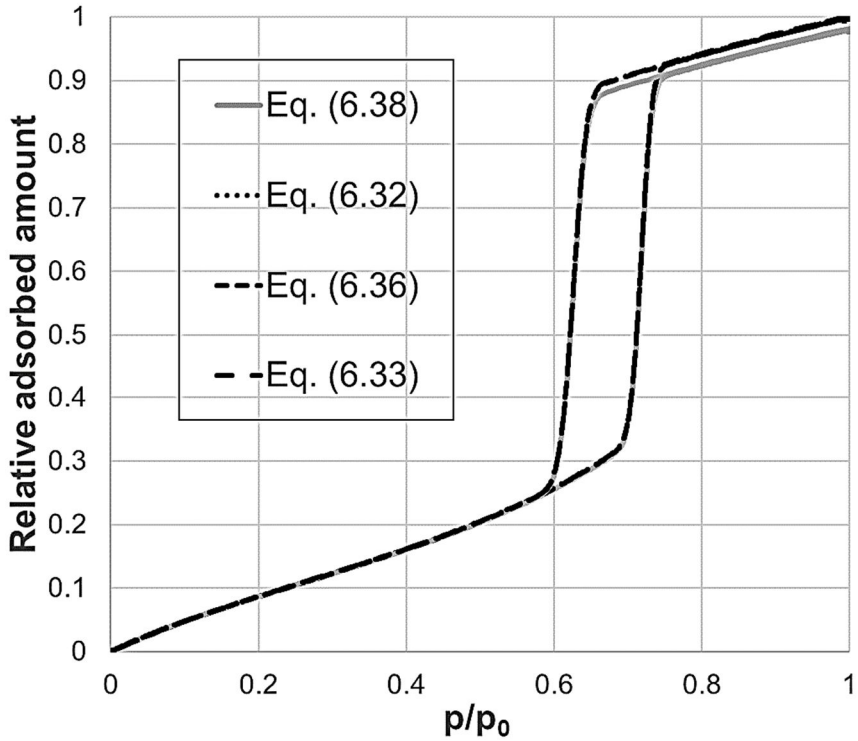

Figure 6.11 – Calculated adsorption and desorption isotherms from the ZLC simulated data using all the outlet flowrate expressions discussed.

6.2.6 Analysis of the blank and deconvolution of the experimental signal

In this paragraph, the mathematical procedure used to perform the blank response analysis of the system and the deconvolution of the detector signal are reported and described. The flowsheet of the experimental ZLC system and the section of the system examined are shown in figs 6.3 and 6.12.

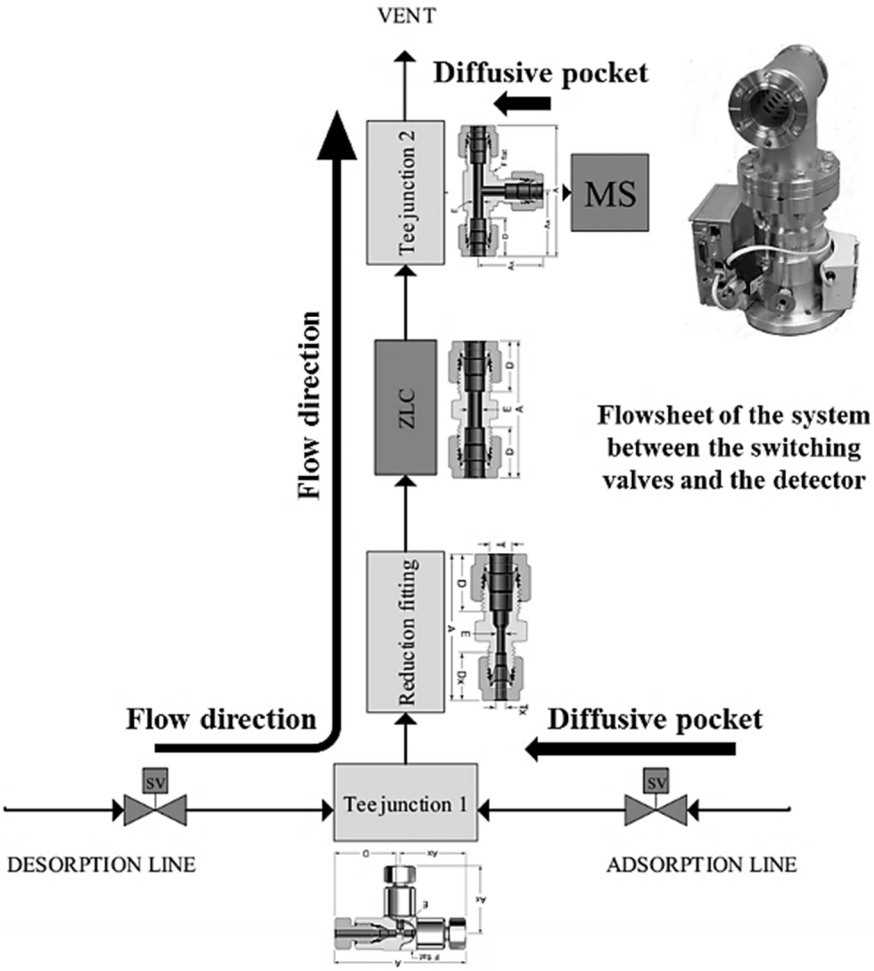

Figure 6.12 – Schematic flowsheet of the experimental system after the two switching valves (see fig. 6.3).

The straight reducing fittings and the blank ZLC were considered as perfectly mixed volumes and the mathematical model can simply be expressed as:

$$V_{mix}\frac{dc}{dt} = F(c_{in} - c) \tag{6.40}$$

Where V is the mixing volume of the fitting, F is the volumetric flowrate, c_{in} is the inlet concentration and c is the outlet concentration. Equation (40) can be converted in dimensionless form and written in the Laplace domain as:

$$\tilde{G}(s) = \frac{\tilde{C}(s)}{\tilde{C}_{in}(s)} = \frac{a}{s+a} \tag{6.41}$$

Where $G(s)$ is the transfer function between the inlet and outlet concentration. a is the inverse of the time constant of the mixing volumes and it can be expressed as:

$$a = \frac{F}{V} \tag{6.42}$$

The tee-junctions were considered as made of a perfectly mixed volume plus a slab diffusive side pocket. The transfer function between the inlet and outlet concentration can be expressed as:

$$\tilde{G}(s) = \frac{\tilde{C}(s)}{\tilde{C}_{in}(s)} = \frac{L}{\alpha\sqrt{\frac{s}{\alpha}}tanh\left(\sqrt{\frac{s}{\alpha}}\right)+\gamma s+L} \tag{6.43}$$

Where

$$\alpha_{fitting} = \frac{D}{X^2} \tag{6.44}$$

$$L_{fitting} = \frac{F}{V_{diff}} \tag{6.45}$$

$$\gamma_{fitting} = \frac{V_{mix}}{V_{diff}} \tag{6.46}$$

Where $\alpha_{fitting}$ is the inverse of the time constant; D is the water vapour diffusivity in nitrogen; X is the diffusive length; V_{diff} is the volume of the diffusive pocket; V_{mix} is the mixing volume; $\gamma_{fitting}$ is the relative accumulation parameter of the fitting. The detector response has already been modelled in the literature as an equivalent ZLC system characterized by a Langmuir isotherm and a linear driving force for the expression of the kinetics in the diffusive pocket [41]. Considering that the pressure at which the vacuum chamber is maintained is about 10^{-6} torr, the Langmuir isotherm might be a strong assumption to justify and even an eventual adsorption of the gas on the inner wall of the chamber seems to be highly doubtful. Moreover, the assumption of a linear driving force might represent an incorrect approximation of the transport mechanism in the diffusive volume. In this work, the detector was considered as made of a perfectly mixed volume in which the gas molecules are continuously aspirated by the turbomolecular pump and a diffusive side volume. The ionizing quadrupole is located at the entrance of the mixing volume, while the filament is immersed in the mixing volume. Considering the uncertainty about the flow pattern inside the detector, a diffusive transport in spherical geometry was assumed for the side pocket. The mass balance in the mixing volume

of the detector is the same of the one expressed in Eq. (6.43). Considering the spherical diffusion in the side pocket and converting the dimensionless mass balance in the Laplace domain, the transfer function between the concentration in the mixed volume and the concentration at the inlet of the detector is given by:

$$\tilde{G}_{detector}(s) = \frac{\tilde{C}_{detector}(s)}{\tilde{C}_{in}(s)} = \frac{L}{3\alpha\sqrt{\frac{s}{\alpha}}coth\left(\sqrt{\frac{s}{\alpha}}\right) - 3\alpha + \gamma s + L} \tag{6.47}$$

Where $\tilde{C}_{detector}(s)$ is the experimental signal provided by the detector in the Laplace domain and $\tilde{C}_{in}(s)$ is the concentration at the inlet of the detector (tee-junction 2). The parameters are defined in the same way as the parameters in Eq. (6.43). The dynamic response of the system to a stepwise concentration change is obtained by multiplying the transfer functions of all the components by the forcing function.

$$\tilde{C}_{detector}(s) = \tilde{G}_{tee-junction\,1}(s)\tilde{G}_{reducing\ fitting}(s)\tilde{G}_{ZLC}(s)\tilde{G}_{tee-junction\,2}(s)\tilde{G}_{detector}(s)\tilde{C}_{in}(s) \tag{6.48}$$

The forcing function which corresponds to a stepwise change of the inlet concentration of the tee-junction 1 is expressed as:

$$\tilde{C}_{in}(s) = \frac{1}{s} \tag{6.49}$$

The inversion of the $\tilde{C}_{detector}(s)$ in the time domain was performed using the method of residues. The simulated responses of all the fittings are reported in section 8.2.6. As already mentioned beforehand, the response of all the fittings is essentially a stepwise drop. Most of the blank response is due to the residence time of water in the detector. Therefore, the concentration at the outlet of the ZLC can be approximated by the concentration at the tee-junction 2. A numerical procedure can be adopted for the deconvolution the experimental signal acquired by the detector. The deconvolution procedure is aimed to obtain the experimental signal at the inlet of the detector. Using the properties of the convolution integral, the concentration of the detector can be expressed as:

$$C_{detector}(t) = \int_0^t G_{detector}(t-u)\, C_{in}(u)du \tag{6.50}$$

The experimental concentration $C_{detector}(t)$ is known and the aim is to calculate $C_{in}(t)$ at the inlet of the detector. The convolution integral can be numerically approximated with an algebraic equation which can be solved implicitly for different intervals of time to calculate $C_{in}(t)$. The easiest numerical approximation is the trapezoidal rule. The convolution integral can therefore be written for each generic interval of time $\Delta t = (t_2 - t_1)$ as:

$$\Delta C_{detector}(t_2 - t_1) = \int_{t_1}^{t_2} G_{detector}(t-u)\, C_{in}(u)du =$$

$$= [G_{detector}(t_2 - t_1)C_{in}(t_1) + G_{detector}(t_2 - t_2)C_{in}(t_2)]\frac{(t_2-t_1)}{2} \quad (6.51)$$

Then for a generic time t_2:

$$C_{detector}(t_2) = \int_0^{t_2} G_{detector}(t_2-u)\, C_{in}(u)du = \Delta C_{detector}(t_2 - t_1)$$

$$+ \sum_{i=0}^{\frac{t_2}{\Delta t}-1} \Delta C_{detector}\,(t_{i+1} - t_i) \quad (6.52)$$

Considering the first time interval which goes from $t = 0$ to $t = \Delta t$, $C_{in}(0)$ is known and it is the initial concentration of the system at the beginning of the desorption. $C_{in}(\tau_2)$ can be calculated by solving Eq. (6.52) and the same procedure is applied for the subsequent steps. The time interval Δt, chosen for the deconvolution iteration, must be small enough to ensure the numerical stability. However, extremely small values of Δt might lead to unnecessary computational times. The same values of the parameters L, γ and α used for the prediction of the blank response are to be used for the deconvolution calculation. The other procedure which can be used to perform the deconvolution consist in approximating the forcing function $C_{in}(u)$ with a linear function in the interval Δt [42]. The convolution integral can be written as:

$$\Delta C_{detector}(t_2 - t_1) = \int_{t_1}^{t_2} G_{detector}(t-u)\, C_{in}(u)du =$$

$$= \int_{t_1}^{t_2} G_{detector}(t-u)\left[C_{in1} + \frac{C_{in2}-C_{in1}}{t_2-t_1}(u - t_1)\right]du \quad (6.53)$$

$C_{in}(\tau_2)$ can be calculated as already shown in Eq. (6.52). This approach permits to use the adaptive quadrature formulas implemented on the mathematical software packages. These formulas are more accurate and stable compared to the trapezoidal approximation and this results in faster computational times.

7 Equilibrium models

7.1 Introduction

The adsorption-desorption equilibrium isotherm of vapors on silica-based mesoporous materials such as MCM-41, SBA-15, and similarly ordered solids has been modeled by following several approaches. Historically, this modeling has been particularly challenging due to the complex shape of the equilibrium isotherm, which contains a characteristic hysteresis loop [43]. Today, it is quite clear that the shape of the adsorption isotherm is mainly correlated to three factors: the geometric structure of the solid, the surface chemistry of the solid, and the physical status of the adsorptive inside the pores. The modern molecular simulation approaches, e.g., GCMC and DFT, represent the state of the art in the field of porous solid characterization via adsorption and they can consider all these factors. Indeed, these techniques are capable of microscopically simulating the interactions that occur when considering an adsorptive molecule confined inside a nanoporous solid [30,44,45]. However, simple analytical expressions for these theories do not exist and they cannot be easily incorporated into the simulations of traditional adsorption processes, e.g., PSA (pressure swing adsorption) or TSA (temperature swing adsorption).

One of the first attempts to predict type IV or type V isotherms [43] was presented in the latest modification of the BET theory [46]. The model was proposed as an alternative to the capillary condensation phenomena with the more general intent of covering all the types of isotherms present in literature. This model has then been replaced by more accurate models based on the widely accepted capillary condensation theory. Later, the systematic study conducted by Everett [47] on the hysteresis phenomena gave birth to the “independent domain theory”. This theory has so far been used for the interpretation of the hysteresis loops arising from adsorption of condensable vapors on ordered mesoporous solids made of independent pores. The theory is based on the main assumption that any physical system showing hysteresis can be considered as made of non-interacting domains. Each domain can be characterized by a distribution function in which only two discrete conditions are permitted, completely empty or completely full in case of adsorption phenomena. The amplitude and shape of the distribution functions give a particular shape to both the boundary and scanning curves of the hysteresis loop. This approach is quite accurate for ordered solids made of perfect cylindrical and independent pores, such as MCM-41 and SBA-15. The adsorption equilibrium isotherms of vapours on these types

of solids are generally characterized by a hysteresis loop with parallel adsorption and desorption branches. This confirms the main assumption of Everett's theory. The shape of the scanning curves can be used to collect exceptional and crucial indications about the internal structure of the solid [48]. For solids made of perfectly cylindrical independent pores, these curves are supposed to depart from one branch of the isotherm, cross the hysteresis loop and join the other branch in an almost straight line. However, this behavior has rarely been observed experimentally in the literature [49]. The independent domain theory has been extended by considering a solid made of independent pores with different diameters along the same pore. This attempt is meant to represent the probable roughness on the inside pore surface of SBA-15 [50–52]. In this view, the domains inside the same pore are no longer independent of each other. To account for the interactions among the domains, the new phenomena of advanced adsorption and pore blocking have been introduced respectively for the adsorption and desorption mechanisms. The advantage of this innovative approach, which was already partially introduced in Everett's theory [53], is due to enhanced flexibility in predicting the different behavior of the scanning curves and sub-loops.

Relatively simpler analytical equilibrium adsorption models have been developed to interpret the adsorption of condensable vapors on ordered mesoporous solids [54–56]. The key point of these models is to consider a multilayer surface adsorption sequentially followed by the capillary condensation of the liquid inside a distribution of mesopores. Oh et al. [57] implemented an even simpler approach by using more traditional expressions for the adsorption isotherms. In this case, two distinct types of isotherms have been combined for a good fit of the experimental data: a linear isotherm from low concentration to the onset of capillary condensation combined with the Sips isotherm for the capillary condensation and saturation part of the equilibrium isotherm. However, the equilibrium isotherm of water on SBA-15 is not perfectly linear up to the condensation threshold, as it shows a small curvature in the Henry law region. Other authors have used the Dubinin-Astakhov model for both the main adsorption curves and the scanning curves [58]. The weak point of this approach is given by the lack of the Henry law constant of the equilibrium model and by the limited applicability at very low concentration. In addition, this approach generates mathematical discontinuities between the adsorption and desorption branches at the upper and lower closure points of the hysteresis loop. Firstly, such discontinuities are not observed experimentally. Secondly, these discontinuities can result in mathematical instabilities when used in dynamic adsorption simulations. The scanning curves can be predicted by the same model although a set of different parameters is required for each scanning curve.

In this Chapter, three different analytical models for the prediction of water vapor adsorption on SBA-15 and silica gel were formulated and derived. The first formulation of the model considers an adsorbent made of regular independent cylindrical pores. The second formulation of the model considers non-regular independent cylindrical pores for a better prediction of the scanning curves. The last formulation of the model considers the adsorption and desorption of condensable vapors in a disordered solid made of pore networks. The models for SBA-15 were designed to simultaneously consider the adsorption in micro-pores, multilayer adsorption in mesopores, capillary condensation phenomena, advanced capillary condensation and pore blocking effect during the evaporation in the mesopores [23]. The model for silica-gel introduces the possibility of a percolation desorption mechanism for the main desorption curve and for the desorption scanning curves.

7.2 Literatures models

As discussed in the introduction section, there have been many attempts in the literature to introduce analytical models able to predict either type IV or type V isotherms. The key challenge is to provide a reasonably simple analytical model able to accurately predict the experimental data throughout the range of concentration. The task is not easy if one considers the complex shape of the isotherm and the presence of a hysteresis loop. In addition, it would be useful to have the same analytical expression for the main adsorption-desorption branches and the scanning curves.

The analytical models in the literature most likely to be able to reproduce the main adsorption-desorption branches and the scanning curves for water vapor on SBA-15 [54] are the ones formulated by Brunauer et al. [59]; Rajniak et al. [60]; Moore et al. [61]; Liu et al. [54]. The analytical expressions of these models can be found in table 7.1.

Table 7.1 – Analytical expressions for the literature isotherm models considered in this study.

Ref.	Model expression
Brunauer et al. [59]	$V_{ml} = V_m \frac{Cx}{(1-x)} \frac{1 + (0.5n_{max}g - n)x^{n_{max}-1} - (n_{max}g - n_{max} + 1)x^{n_{max}} + 0.5n_{max}gx^{n_{max}+1}}{1 + (C-1)x + (0.5Cg - C)x^{n_{max}} - 0.5Cgx^{n_{max}+1}}$
Rajniak et al. [60]	$V_{ads} = V_{sat} \exp\left[-\left(Kln\left(\frac{1}{x}\right)\right)^n\right]$
Moore et al. [61]	$q_{ads} = q_{s1}x^{k_1 T} + (q_{s2} - q_{s1})x^{k_2 T}$
Liu et al. [54]	$q_{ads} = q_m x^{k_m T} + (q_s - q_m)\,\mathrm{erf}\left[\frac{-k_c}{Tln(x)}\right]$

The models formulated by Rajniak et al. [60] and Liu et al. [54] have been used for the simulation of pressure swing adsorption processes in packed beds for water vapor removal [62–65]. Therefore, such models are probably considered the most appropriate analytical expressions for the correlation of type IV isotherms.

Figures 7.1-7.4 show the experimental data and the correlation obtained by using the models of Brunauer et al. [59], Rajniak et al. [60], and Liu et al. [54] for several concentration ranges. In general, these models are capable of reproducing a limited range of adsorbed phase concentrations, but all fail in describing the entire adsorption isotherm.

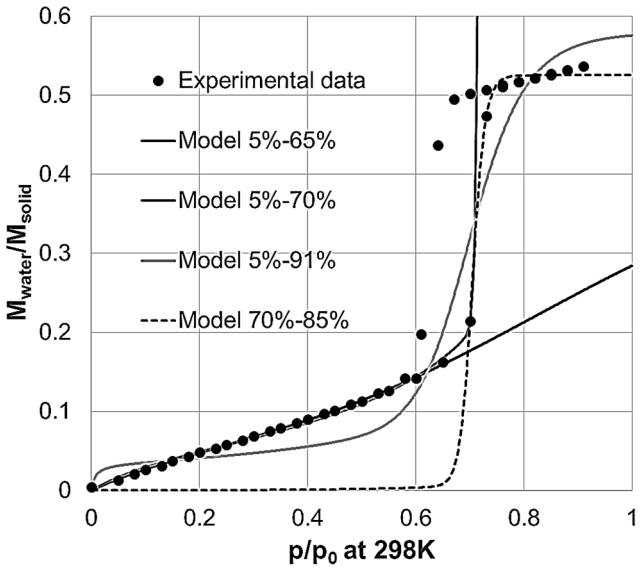

Figure 7.1 – Correlation of the experimental data with the BET model [59] for different concentration ranges.

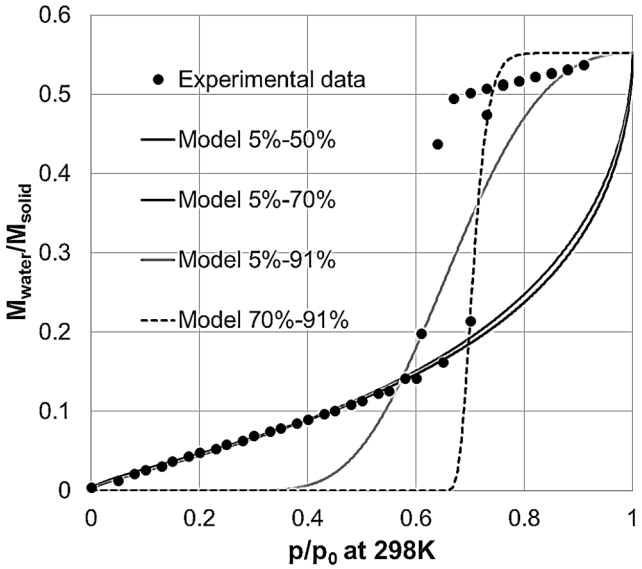

Figure 7.2 – Correlation of the experimental data with the model of Rajniak et al. [60] for different concentration ranges.

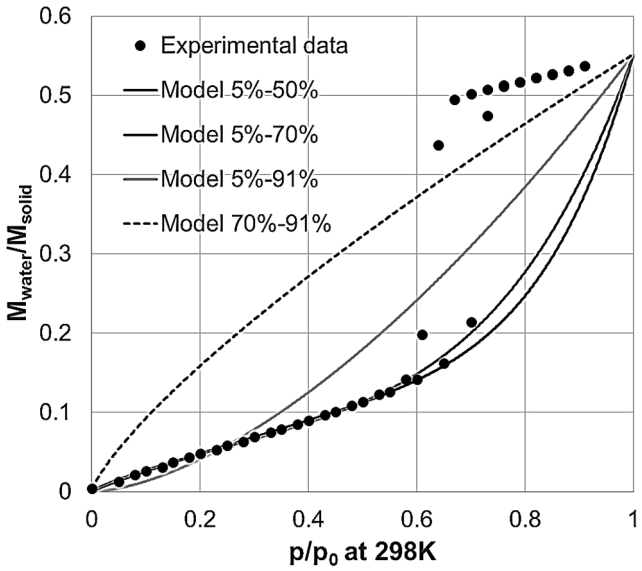

Figure 7.3 – Correlation of the experimental data with the model of Moore et al. [61] for different concentration ranges.

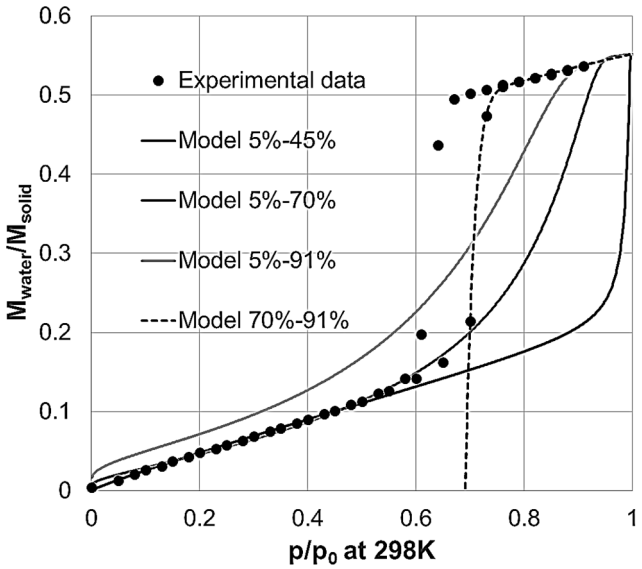

Figure 7.4 – Correlation of the experimental data with the model of Liu et al. [54] for different concentration ranges.

7.3 Independent pores model

The adsorption of condensable vapors on a micro-mesoporous solid can be described through different adsorption mechanisms depending on the relative saturation value of the vapor phase $x = p/p_0$ in equilibrium with the adsorbed phase.

In general, at very low pressures ($p/p_0 < 0.05$), the micropores will be filled first and a prevalently monolayer adsorption will occur in the mesopores. All the adsorptive molecules will therefore adsorb on the free surface. These adsorption mechanisms can be represented with

the Langmuir model for the micropores and the BET model for the mesopores. At values of $p/p_0 > 0.05$, the adsorptive molecules will simultaneously adsorb on the free surface and on the adsorbate phase in the mesopores. The multilayer adsorption described by the BET model will be the predominant adsorption mechanism. By increasing the value of p/p_0 in the gas phase, the thickness of the multilayer adsorbed phase or clusters will increase and at a given value of partial pressure, the pores will be filled with a capillary condensed phase. The condensation pressure will mainly depend on the size of the mesoporous channel. A specular mechanism can be considered for a desorption scenario in which the pores are initially filled with capillary condensed liquid. The evaporation pressure will again mainly depends on the size of the mesoporous channels.

Two analytical expressions for the adsorption-desorption equilibrium isotherm of water vapor on SBA-15 were derived. The mathematical derivations of the models are reported in the following sections. The first model considers a solid made of perfectly cylindrical independent pores. In this model, the pores are filled and emptied in an ordered sequence from the smallest to the largest and *vice versa*. The mathematical formulation of the first model can be expressed as:

$$\frac{m_{ads}}{m_{sat}} = \frac{d\frac{Cx}{(1-Jx)[1+(C-1)x]}\int_{r_c(x)}^{r_{max}} f_r(2r-d)dr + \rho_r(x)\int_{r_{min}}^{r_c(x)} f_r r^2 dr}{\int_{r_{min}}^{r_{max}} f_r r^2 dr} + \frac{m_{res}}{m_{sat}} \tag{7.1}$$

Where m_{ads} is the amount of water adsorbed divided by the dry mass of the solid. m_{sat} is the amount of water adsorbed at saturation, i.e. $x = p/p_0 = 1$, divided by the dry mass of the solid. m_{res} is the mass of residual water trapped inside the solid. C is the equilibrium constant of the BET model and takes into account the temperature and the difference between the heat of adsorption on the free surface and the heat of condensation of the vapour. C is responsible for the slope of the isotherm at low concentration. J is the surface reduction coefficient introduced by Anderson [66]. J influences the shape of the multilayer adsorption region and it also limits the amount adsorbed at medium-high concentrations. d is the thickness of the first adsorbed layer. f_r is the pore size distribution of the mesopores expressed as a numerical fraction of pores with radius r. For the radii of the mesopores, a truncated log-normal pore size distribution (PSD) was adopted with r_{min} and r_{max} respectively as lower and upper bounds of the distribution. The two parameters of the pore size distribution σ and μ influence the slope and the position of the capillary condensation and evaporation branches with respect to the x-axis. $r_c(x)$ is the radius of the pore condensing at the relative pressure x.

The condensation and evaporation pressures are calculated using the Kelvin equation respectively for cylindrical and hemispherical meniscus as reported in Eq. (7.22) and Eq. (7.28). $\rho_r(x)$ is the relative density of the capillary condensed liquid and it is expressed in Eq. (7.33). $\rho_r(x)$ influences the slope of the top part of the isotherm after the capillary condensation and before the onset of capillary evaporation. The relative density change depends on the packing factor of the liquid condensed phase inside the pores which is defined in the following section as κ. The desorption branch of the model is represented by the same mathematical expression of Eq. (7.1). $r_c(x)$ is replaced by $r_e(x)$ which gives the radius of the pore evaporating at the relative pressure x.

For the desorption branch, there is one more parameter given by the evaporation angle θ between the solid surface and the liquid hemispherical meniscus. The parameter θ is defined in Eq. (7.27) and influences the position of the desorption evaporation branch with respect to the x-axis. An angle θ equal to 0° corresponds to a semi-spherical equilibrium meniscus, while, an angle θ equal to 90° corresponds to a flat equilibrium meniscus. Consequently, the desorption evaporation branch will respectively be shifted to the lowest and the highest possible evaporation pressures. The effect of the model parameters on the shape of the calculated equilibrium isotherm are shown in figs 7.5-7.11.

- The J parameter (fig. 7.5) influences the thickness of the multilayer adsorbed phase. Lower values of J correspond to thinner multilayers at the same value of relative pressure. The shift in the condensation pressures is due to the higher value of pressure requested to reach the critical multilayer thickness for the condensation to occur.
- The d parameter (fig. 7.6) represents the thickness of the first adsorbed layer and influences the multilayer adsorbed amount as well as the condensation and evaporation pressures.
- The C parameter (fig. 7.7) clearly changes the shape of the first part of the isotherm and it also influences the condensation pressures.
- The θ angle (fig. 7.8) only influences the evaporation pressures.
- The σ parameter (fig. 7.9) changes the dispersion of the pore size distribution and influences the shape of the capillary condensation and evaporation branches.
- The μ parameter (fig. 7.10) changes the mean value of the pore size distribution and influences the position of the hysteresis loop with respect to the x-axis. The parameter also changes the multilayer adsorption part of the isotherm due to the different pore sizes.
- The parameter κ (fig. 7.11) influences the slope of the top part of the isotherm.

A more detailed description and derivation of the isotherm parameters is given in section 7.5.

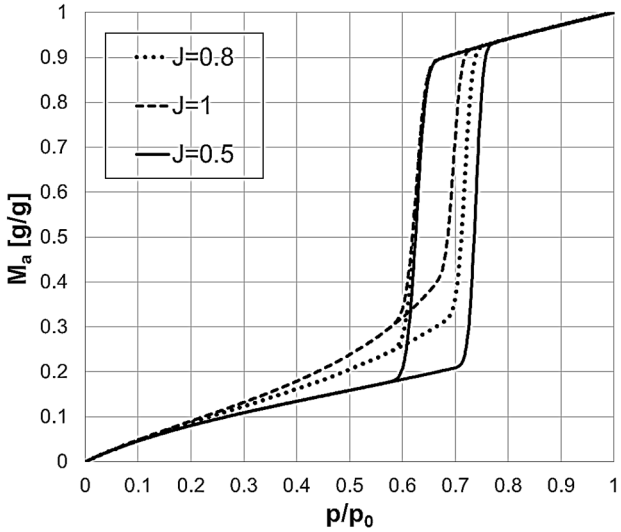

Figure 7.5 – Effect of the parameter J on the shape of the equilibrium isotherm model.

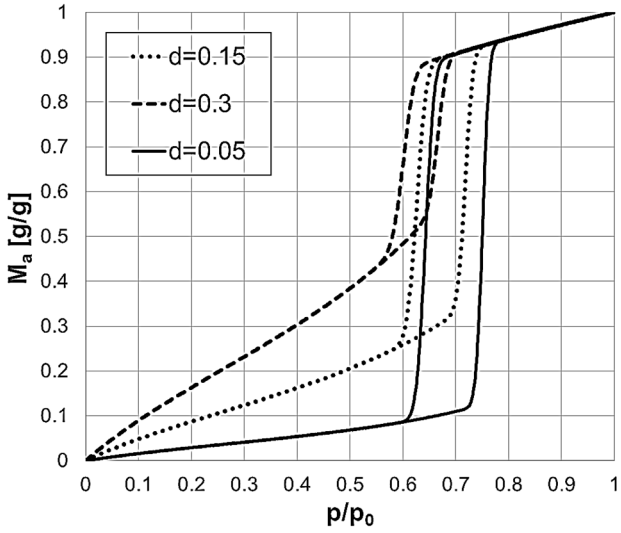

Figure 7.6 – Effect of the first layer thickness d on the shape of the equilibrium isotherm model.

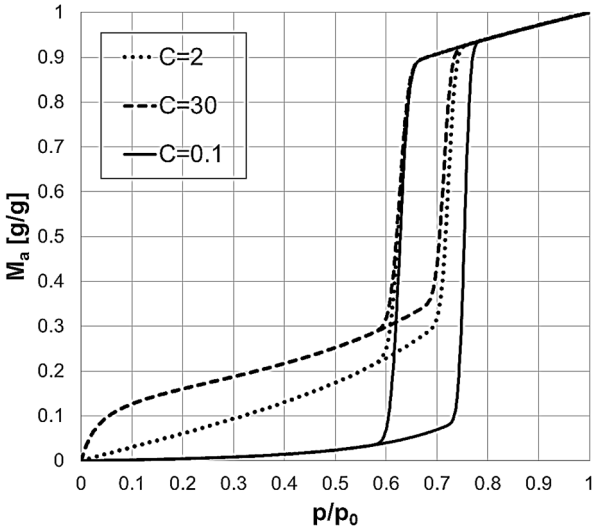

Figure 7.7 – Effect of the BET equilibrium constant C on the shape of the equilibrium isotherm model.

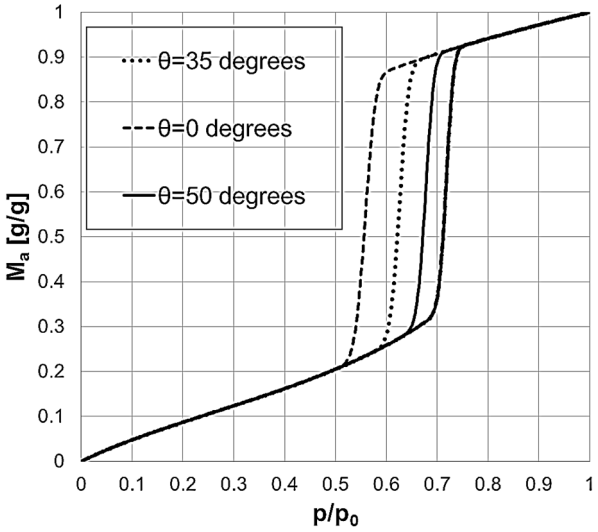

Figure 7.8 – Effect of the desorption angle θ on the shape of the equilibrium isotherm model.

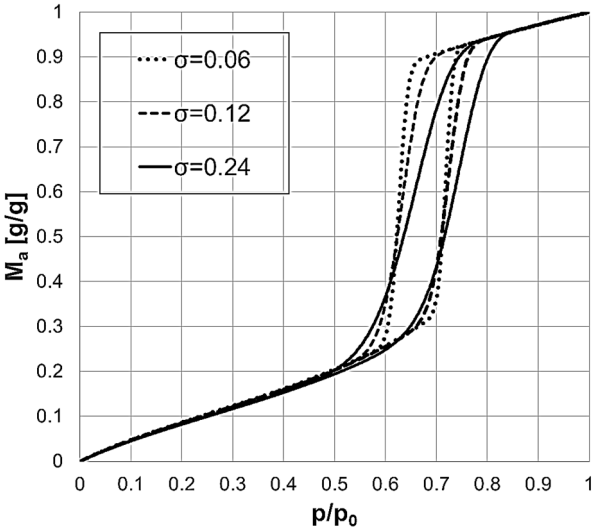

Figure 7.9 – Effect of the PSD dispersion σ on the shape of the equilibrium isotherm model.

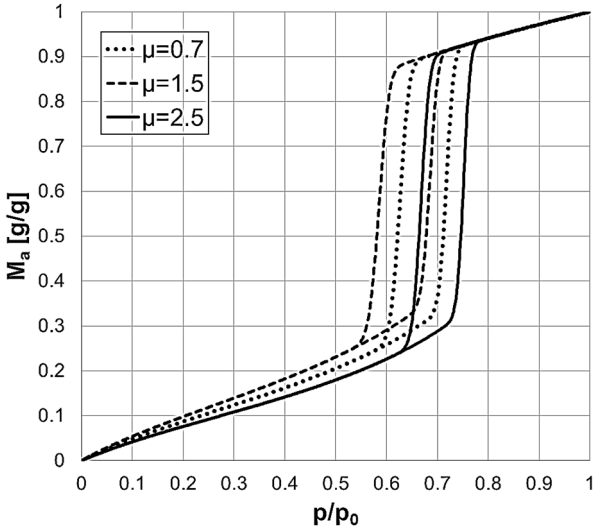

Figure 7.10 – Effect of the PSD mean value μ on the shape of the equilibrium isotherm model.

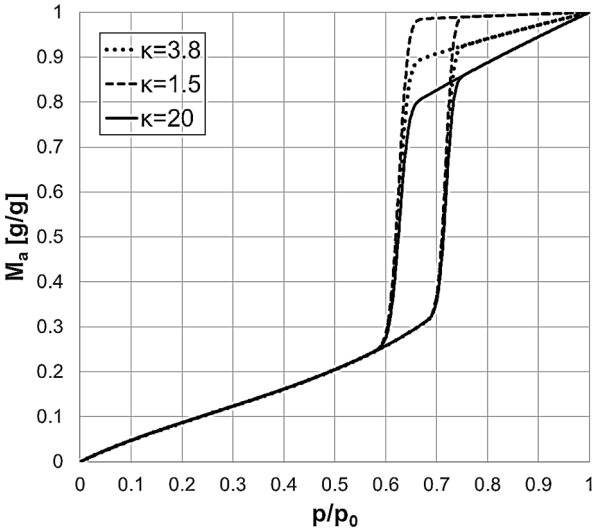

Figure 7.11 – Effect of the compressibility parameter κ on the shape of the equilibrium isotherm model.

These plots clearly demonstrate that while Eq. (7.1) contains several physical parameters, each parameter influences in a clear way different portions of the adsorption isotherm. This facilitates the evaluation of the parameters since each one can be determined independently by focussing on different regions in sequence. Once good estimates for all the parameters are obtained, a final non-linear regression ensures a close match with the experimental results. The model in Eq. (7.1) was used to regress the experimental data at three different temperatures as shown in fig 7.12.

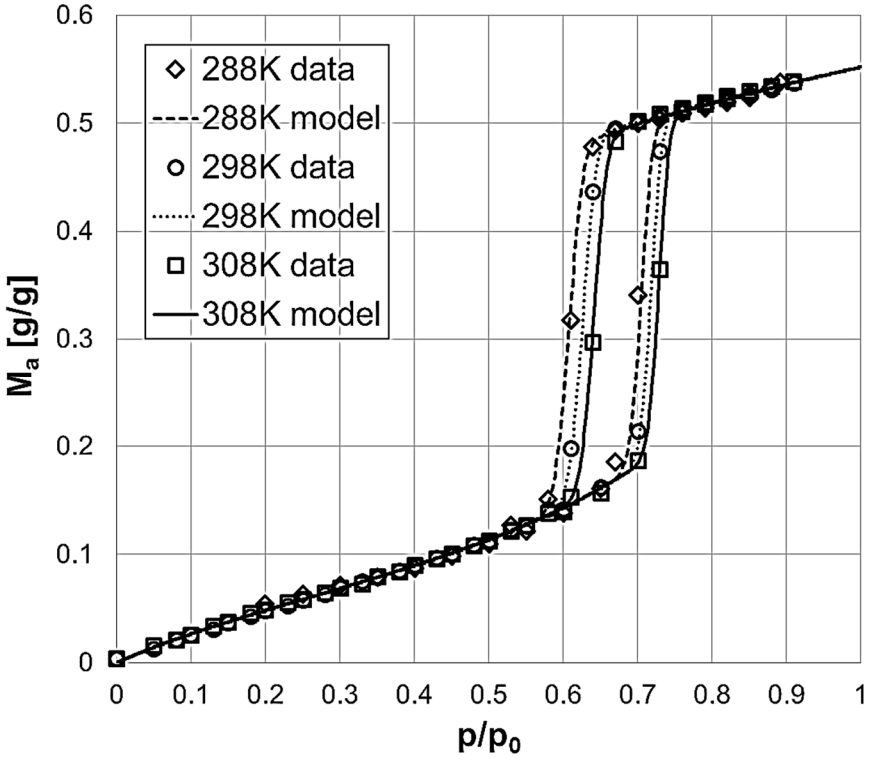

Figure 7.12 – Experimental adsorption-desorption data and model correlation for water *vapor* on SBA-15 at 288 K, 298 K, and 308 K.

The parameters of the model, reported in table 7.2, were calibrated by using the data at 298 K. The same temperature independent parameters were then used to predict the experimental data at 308 K and 288 K with an excellent agreement. m_{res} is set equal to zero given that in process applications only the reversibly adsorbed water contributes. If for completeness one wishes to include this, m_{res} can be measured independently from the first adsorption-desorption run.

Table 7.2 – Parameters used for the regression of the experimental data with the model expressed in Eq. (7.1). The parameters σ and μ refer to a log-normal pore size distribution.

	298 K
$\boldsymbol{d}$ **(nm)**	0.153
$\boldsymbol{J}$	0.839
$\boldsymbol{C}$	3.66
$\boldsymbol{\theta}$° ($\boldsymbol{desorption}$)	36.5
$\boldsymbol{\sigma}$	0.045
$\boldsymbol{\mu}$	0.663
$\boldsymbol{m_{sat}}$ **(g/g)**	0.55
$\boldsymbol{\kappa}$ **(Pa^{-1})**	$4.42*10^{-9}$

The theoretical modeling of the scanning curves is quite straightforward under the assumption of a solid made of perfectly cylindrical independent pores. This basic assumption permits one to model the adsorption process in a single pore independently from all the other pores. For each pore, the condensation and the evaporation pressures will only be a function of the radius of the specific pore. Each pore is allowed to condense and evaporate independently of the status of the other pores. A given point on the vertical part of the adsorption branch corresponds to a point in which only part of the pores are filled with condensed liquid and the rest of the pores still have a multilayer adsorbed phase on the pore walls. If a desorption process is originated from that specific point, the amount adsorbed will not go back reversibly on the adsorption branch, but it will rather cross the hysteresis loop and eventually join the desorption branch. When doing this, the pores will evaporate independently from each other. The first pore to evaporate will be the last pore condensed during the adsorption process. Therefore, as long as the partial pressure of water does not reach the evaporation pressure of that specific pore, the only desorption mechanism happening will be the shrinkage of the liquid condensed phase in the condensed pores and the decrease of the multilayer adsorbed phase in the non-condensed pores. The amount adsorbed will theoretically follow a trajectory similar to the multilayer and saturation part of the isotherm. The scanning curves will eventually cross the hysteresis loop

and join the main desorption branch at the evaporation pressure of the last pore condensed. A specular scenario can be considered for the adsorption scanning curves.

This theoretical behavior predicts a discontinuity at the contact point between the scanning curves and the main branches. However, such a behavior has not been observed experimentally unless some cavitation phenomenon is present [44,67]. Indeed, it has been observed in the literature that the most common behavior for experimental scanning curves on solids made of cylindrical independent pores is to approach the desorption curve with a smoother curvature instead of a straight crossing line. The difference between the experimental data and the model prediction has been attributed to not perfectly cylindrical pores [50,52,68].

7.4 Quasi-independent pores model

The presence of imperfections or restrictions on the internal surface of the cylindrical pore has theoretically been demonstrated to give a different behavior to the scanning curves and to the main adsorption and desorption curves. An increase of either the number or the amplitude of the distribution of imperfections along the pore leads to scanning curve characterized by a less crossing and more converging behavior. The converging behavior of the scanning curves can be confirmed from our data. The comparison between the theoretical prediction using Eq. (7.1) and the experimental desorption and adsorption scanning curves is shown in fig. 7.13 and fig. 7.14. The theoretical model for perfect cylindrical independent pores is not able to capture the actual behavior of the scanning curves in the entire range of concentration, yet it provides a good match.

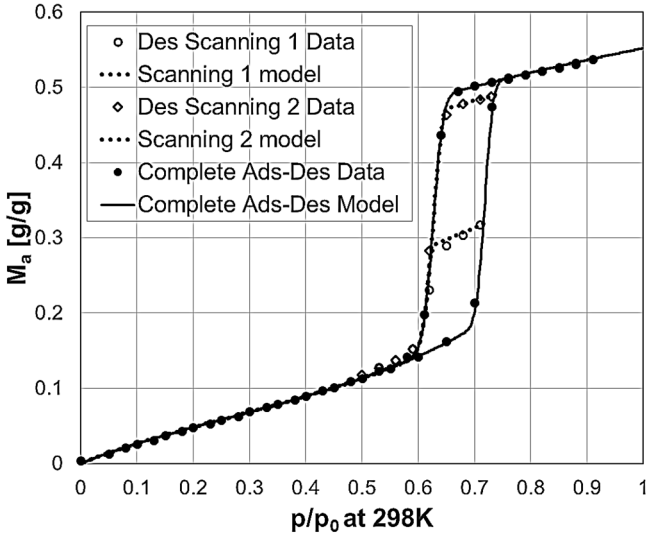

Figure 7.13 – Experimental desorption scanning curves and perfectly cylindrical pores model correlation (Eq. 7.1) at 298 K.

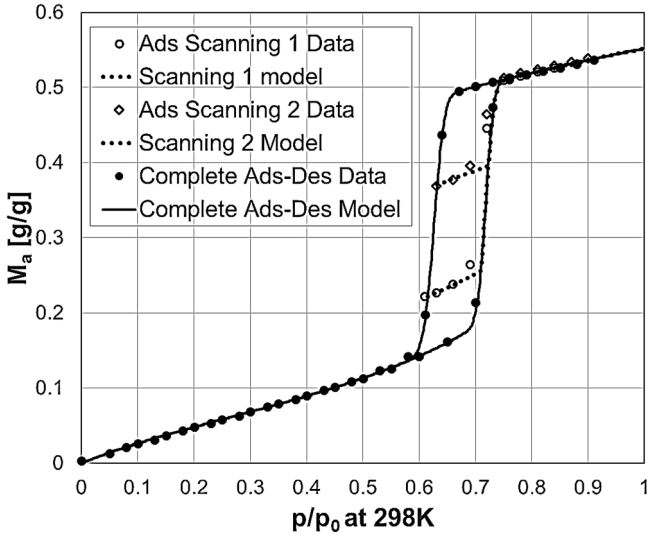

Figure 7.14 – Experimental adsorption scanning curves and perfectly cylindrical pores model correlation (Eq. 7.1) at 308 K.

The second derivation of the equilibrium isotherm was designed considering the particular structure of SBA-15. The adsorption in the interconnecting microporous channels was neglected, and it is assumed that the solid is made of independent cylindrical mesopores, which are defined in this work as the main pores. The mesopores are not perfectly cylindrical, indeed they are made of an ensemble of cylindrical constrictions or sub-pores as illustrated in fig. 7.15.

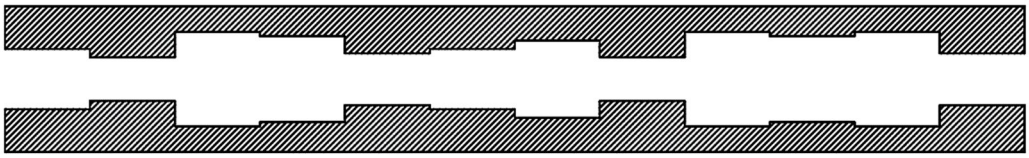

Figure 7.15 – Qualitative representation of the sub-pores inside each main pore of SBA-15.

The amount of mass adsorbed as a function of the relative humidity $x = p/p_0$ is given by:

$$\frac{m_{ads}}{m_{sat}} = \frac{d\frac{Cx}{(1-Jx)[1+(C-1)x]}\sum_{i=0}^{n} f_i \sum_{j=0}^{N} g_j F_j (2r_j - d) + \rho_r \sum_{i=0}^{n} f_i \sum_{j=0}^{N} g_j (1-F_j) r_j^2}{\sum_{i=0}^{n} f_i \sum_{j=0}^{N} g_j r_j^2} + \frac{m_{res}}{m_{sat}} \qquad (7.2)$$

Where f_i is the fraction in number of the main pore i. g_j is the fraction in number of the sub-pore j inside each main pore i. A normal distribution was assumed for the average radii of the main pores. A normal distribution was also assumed for the radii of the sub-pores inside each main pore. The average radius of each main pore was used as mean for the normal distributions of the sub-pores correlated to each main pore. The radius and the sequence of the sub-pores inside each main pore were chosen randomly after imposing a standard deviation value. The same standard deviation was used for the distributions of all the sub-pores inside each main pore. F_j is the function used to designate whether a sub-pore is filled with capillary condensed

liquid or with a multilayer adsorbed phase. F_j is zero if the sub-pore j is filled with condensed adsorbate while it is one for non-condensed sub-pores. In this scenario, the sub-pores are no longer independent of each other and a collaborative effect is assumed for both the condensation and evaporation mechanisms of a sub-pore. The condensation of liquid in a sub-pore occurs in the following scenarios [50]: a) if both adjacent sub-pores are empty and the pressure is equal or higher than the equilibrium pressure given by the Kelvin equation for a cylindrical meniscus; b) if one of the two adjacent sub-pores is already filled and the pressure is equal or higher than the equilibrium pressure given by the Kelvin equation for a hemispherical meniscus. Point a is the only condensation requirement for independent pores and it is always valid. Point b is called advanced condensation and it allows a sub-pore to get filled with liquid condensate although the pressure is less than its condensation pressure. The advanced condensation implies a dependence of the status of a pore on the status of the contiguous pores. The evaporation from a condensed pore occurs if at least one of the two adjacent sub-pores is empty and the pressure is equal or less than the equilibrium pressure given by the Kelvin equation for a hemispherical meniscus. If both the adjacent sub-pores are filled and the pressure is equal or less to the equilibrium pressure, the pore will not empty according to the pore blocking mechanism. The cavitation mechanism was not considered in this work.
In fig. 7.16 and fig. 7.17 it is possible to observe the prediction of the second formulation of the model given in Eq. (7.2). The new model can qualitatively represent the correct behavior of the scanning curves.

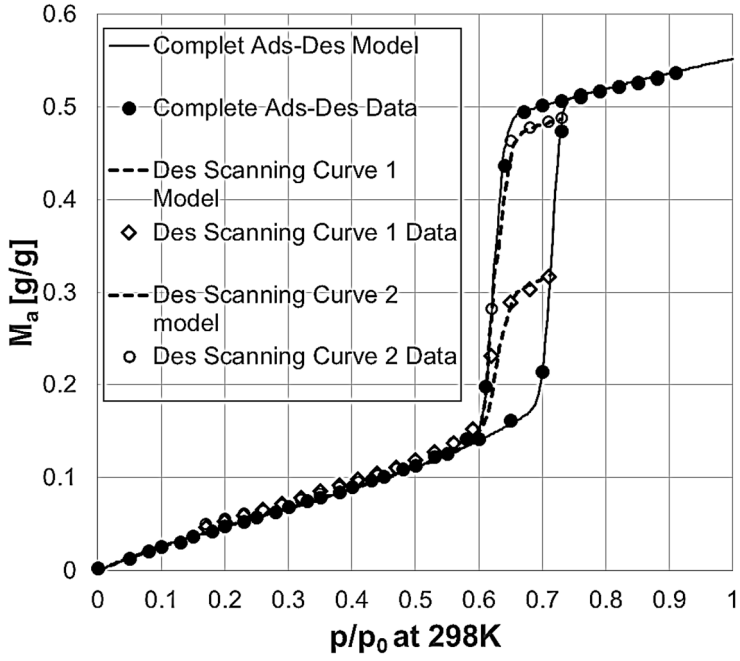

Figure 7.16 – Desorption scanning curve and model prediction (Eq. 7.2) at 298 K.

The minor inconsistency between the model prediction and the experimental data can be explained by the main assumptions about the geometrical structure used for the formulation of the model. It is reasonable to assume that the solid is characterized by a discrete distribution of main pores or in this case by a distribution of the average size of the main pores. It is also reasonable to assume that each of the main pores has the same length. Cylindrical shape and same length are the assumptions used also for the geometry of the sub-pores. These assumptions are mathematically convenient for the modeling of the adsorption in the sub-pores. However, it is probably more realistic to assume defects of different lengths. Secondly, it is probably more common to find smoother and gradual transitions between each constriction rather than a sudden change in the diameter of the pore. These two factors might influence the trajectory of the theoretical scanning curves and give a better prediction of the experimental data.

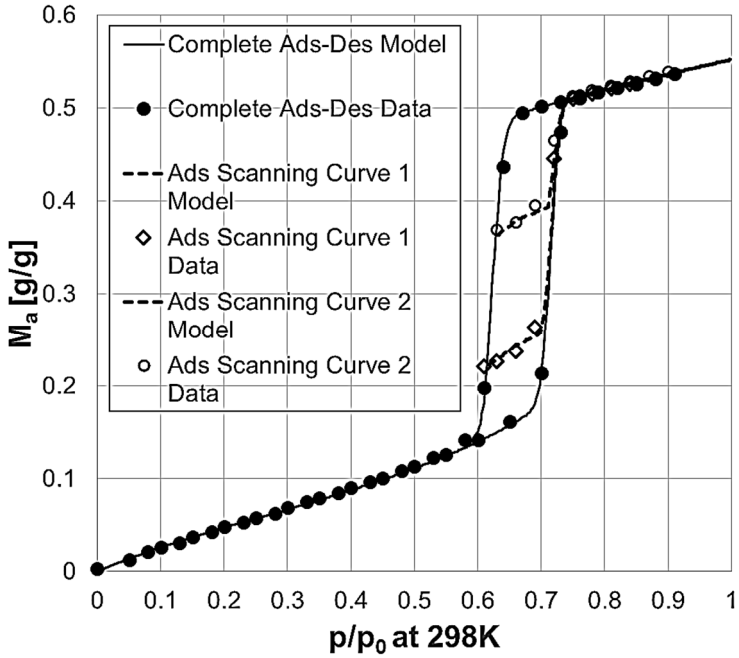

Figure 7.17 – Adsorption scanning curves and model prediction (Eq. 7.2) at 298 K.

The parameters of the equilibrium model expressed in Eq. (7.2), used for the regression of the experimental data shown in fig. 7.16 and fig. 7.17, are reported in table 7.3. A detailed description of the parameters is given in sections 7.5-7.6.

Table 7.3 – Parameters used for the regression of the experimental data with the model given by Eq. (7.2). The parameters σ and μ refer to a log-normal distribution.

	298 K
d **(nm)**	0.153
J	0.839

$\boldsymbol{C}$	3.66
$\boldsymbol{\theta°}$	39.5
$\boldsymbol{r_{min}}$ **(nm)**	1.72
$\boldsymbol{r_{max}}$ **(nm)**	2.06
$\boldsymbol{\sigma\ main\ pores}$	0.06
$\boldsymbol{\mu\ main\ pores}$	1.89
$\boldsymbol{\sigma\ sub-pores}$	0.08
$\boldsymbol{n}$	50
$\boldsymbol{N}$	60
$\boldsymbol{m_{sat}}$ **(g/g)**	0.55
$\boldsymbol{\kappa}$ **(Pa^{-1})**	$4.42*10^{-9}$

7.5 Mathematical derivation of the independent pores model

In this section, the mathematical derivation of the two analytical equilibrium models used in this contribution is reported. The models are based on traditional macroscopic approaches to the adsorption phenomena. These methods are likely obsolete if used for the fully accurate characterization of porous materials. However, they provide a reasonable representation of the real adsorption mechanisms and more significantly, they allow for the introduction of a relatively simple but accurate analytical expression for type IV and type V equilibrium isotherms.

In the first instance, it is feasible to assume a solid made of micropores and mesopores. The mesopores are assumed to be perfectly cylindrical with the same diameter and length. The saturation capacity of such a solid is:

$$V_{s-tot} = V_{meso} + V_{micro} = NL_m\pi r^2 + V_{micro} \tag{7.3}$$

Where N is the number of mesopores; L_m is the length of the mesopores and r is the radius of the mesopores. If the adsorbed phase is uniformly distributed on the surface of the mesopores, the multilayer phase adsorbed on the wall of each pore will be given by the difference between the total volume of the pore and the volume of the empty part of the pore. If $t(x)$ is the thickness of the adsorbed phase on the wall, the volume of the multilayer adsorbed phase V_{ml} as a function of the relative partial pressure $x = p/p_0$ can be expressed as:

$$V_{ml}(x) = N\pi L_m\left[r^2 - \left(r - t(x)\right)^2\right] = N\pi L_m t(x)[2r - t(x)] \tag{7.4}$$

From Eq. (7.1), the thickness of the multilayer adsorbed phase can be found as a function of the partial pressure x. Equation (2) has two roots. Only one root can physically be valid, as the thickness of the amount adsorbed cannot be greater than the radius of the pore. The thickness of the multilayer adsorbed phase can be expressed as:

$$t(x) = r - \frac{\sqrt{\pi(NLr)^2 - L_m N V_{ml}(x)}}{L_m N \sqrt{\pi}} \tag{7.5}$$

The multilayer adsorption can be theoretically represented with one of the many multilayer adsorption models present in the literature. The original BET model [59] represents an extension of the monolayer Langmuir model in which the molecules can adsorb both on the free surface and on the molecules already adsorbed. This model assumes a perfectly flat surface and an infinite adsorbed amount at saturation. The model was later modified by several authors to consider a more realistic adsorption process in a confined environment. The total amount of adsorbed phase was limited to a certain value using different approaches: limited adsorption volume [46], different energetic interactions between the first adsorbed layer and the following layers [69,70], and a continuously decreasing surface [69,71].

The assumptions made for the formulation of the original BET theory can be modified to model the adsorption process on a cylindrical surface. The original BET theory assumes the adsorption to occur on a flat surface and that the surface available for all the layers remains constant. The multilayer volume of the adsorbed phase V_{ml} can be calculated as:

$$V_{ml} = \sum_{i=0}^{\infty} v_i i S_{i-equi} = \sum_{i=1}^{\infty} \frac{V_i}{S_{i-geom}} i S_{i-equi} \tag{7.6}$$

Where v_i is the specific volume of an adsorbate molecule. V_i is the absolute volume occupied by an adsorbate molecule. S_{i-geom} is the actual geometrical surface occupied by a molecule of adsorbate. S_i is the equilibrium surface covered only by the i layers of adsorbate. S_i is given by the dynamic equilibrium relationship for each layer. For flat surfaces v_i is constant and Eq. (7.6) leads to the BET model expressed as:

$$V_{ml} = \frac{V_0}{S_{0-geom}} \sum_{i=1}^{\infty} i S_{i-equi} \tag{7.7}$$

If the adsorption occurs inside cylindrical channels and the adsorbed layer has constant thickness d, as represented in fig. 7.18, the specific volume v_i will depend on the specific layer i. The specific volume v_i of the generic layer i is given by:

$$v_i = \frac{d[2r-(2i-1)d]}{2[r-(i-1)d]} \tag{7.8}$$

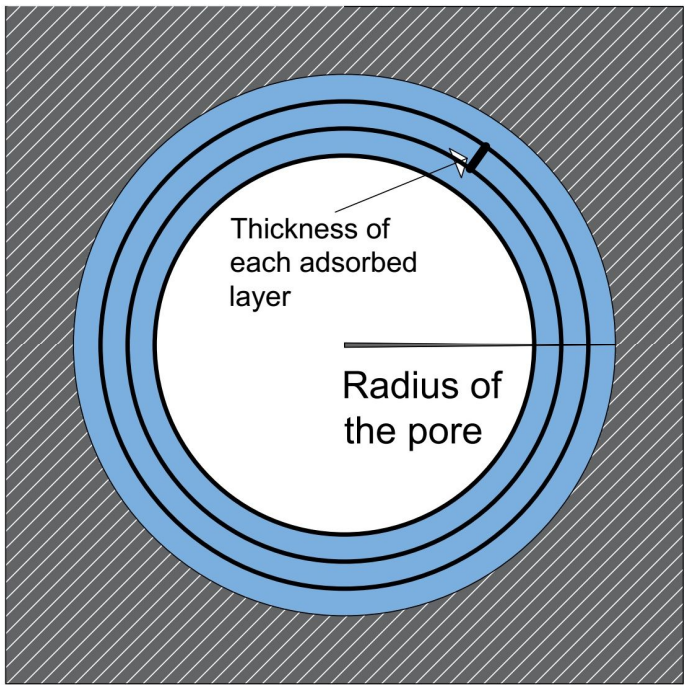

Figure 7.18 – Representation of the adsorbed layers on a cylindrical surface.

By combining Eq. (7.6) and Eq. (7.8), the multilayer adsorbed amount can be expressed as:

$$V_{ml} = \sum_{i=0}^{N_{max}} v_i i S_{i-equi} = \sum_{i=1}^{N_{max}} \frac{d[2r-(2i-1)d]}{2[r-(i-1)d]} i S_{i-equi} \tag{7.9}$$

Where N_{max} is the maximum number of adsorption layers permitted in the pore. N_{max} can easily be calculated if d is known. From a comparison between Eq. (7.7) and Eq. (7.9), the amount adsorbed is now limited to a certain amount and it also depends on the size of the channel. In the same way, the amount adsorbed on the cylindrical pore surface when this is completely covered by a single layer of adsorbate can be defined as:

$$V_m = \sum_{i=0}^{N_{max}} v_i S_{i-equi} = v_0 S_{0-equi} + \sum_{i=1}^{N_{max}} \frac{d[2r-(2i-1)d]}{2[r-(i-1)d]} S_{i-equi} \tag{7.10}$$

From the derivation of the original BET model [72], S_{i-equi} is given by the dynamic equilibrium relationship for each layer i and can be expressed as a function of the relative saturation pressure $x = p/p_0$ as:

$$S_{i-equi}(x) = C S_{0-equi} x^i \tag{7.11}$$

Where C is the equilibrium constant of the BET model defined as:

$$C = exp\left(\frac{\Delta H_{first\ layer} - \Delta H_{condensation}}{RT}\right) \tag{7.12}$$

By combining Eqs (7-9) the multilayer amount adsorbed can be expressed as:

$$\frac{V_{ml}}{V_m} = \frac{\sum_{i=0}^{Nmax} \frac{r}{r-(i-1)d} i S_{i-equi}}{\sum_{i=0}^{Nmax} \frac{r}{r-(i-1)d} S_{i-equi}} = \frac{C S_{0-equi} \sum_{i=0}^{Nmax} \frac{d[2r-(2i-1)d]}{2[r-(i-1)d]} i x^i}{v_0 S_{0-equi} + C S_{0-equi} \sum_{i=1}^{Nmax} \frac{d[2r-(2i-1)d]}{2[r-(i-1)d]} x^i} \tag{7.13}$$

Dividing by S_{0-equi} and considering the explicit expression for v_0:

$$\frac{V_{ml}}{V_m} = \frac{C \sum_{i=0}^{Nmax} \frac{d[2r-(2i-1)d]}{2[r-(i-1)d]} i x^i}{\frac{d(2r-d)}{2r} + C \sum_{i=1}^{Nmax} \frac{d[2r-(2i-1)d]}{2[r-(i-1)d]} x^i} \tag{7.14}$$

By expressing V_m as a function of the radius of the pore and thickness of the adsorbed layer, the final expression for the multilayer adsorbed amount for N pores of radius r is given by:

$$V_{ml}(x,r) = N\pi L_m d(2r-d) \frac{C \sum_{i=0}^{Nmax} \frac{d[2r-(2i-1)d]}{2[r-(i-1)d]} i x^i}{\frac{d(2r-d)}{2r} + C \sum_{i=1}^{Nmax} \frac{d[2r-(2i-1)d]}{2[r-(i-1)d]} x^i} \tag{7.15}$$

A comparison between the traditional BET model and Eq. (7.15) is shown in fig. 7.19. The multilayer adsorption model presented in this study and the original BET model [59] are compared using the same parameters, assuming a pore radius of 2 nm and a thickness of the adsorbed layer of 0.3 nm. As expected, the two models provide the same results at low pressures. At higher pressures, Eq. (7.15) diverges due to the cylindrical adsorption surface which limits the volume available for each following layer.

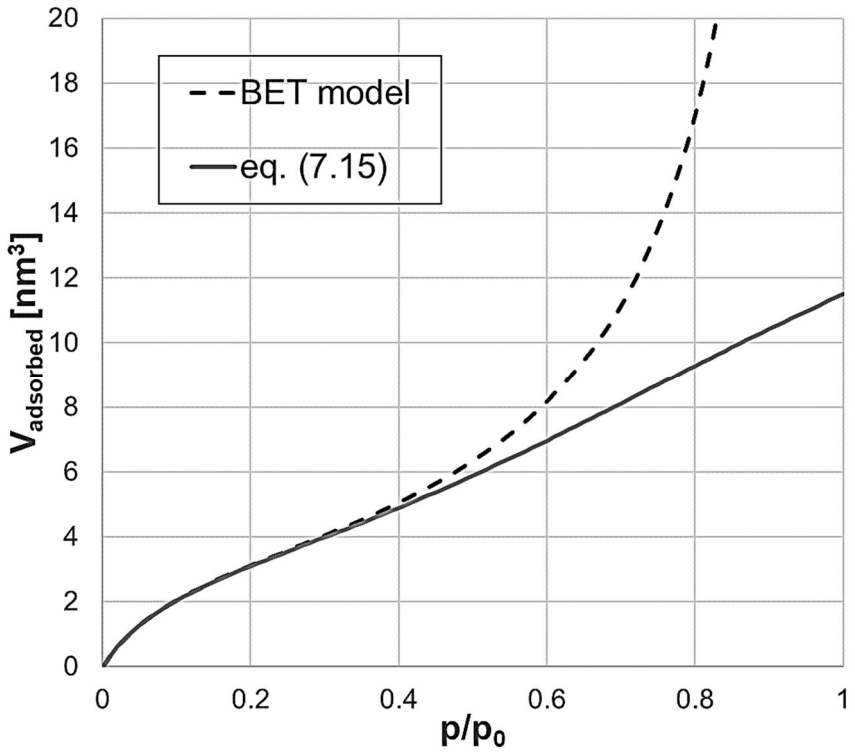

Figure 7.19 – Comparison between the original BET model and the multilayer adsorption model on a cylindrical surface given in Eq. (7.15).

The thickness of the multilayer adsorbed amount for a pore of radius r will be:

$$t(x) = r - \frac{\sqrt{\pi(NLr)^2 - L_m N V_{ml}(x)}}{L_m N\sqrt{\pi}} = r - \sqrt{r - d(2r-d)\frac{C\sum_{i=0}^{Nmax}\frac{d[2r-(2i-1)d]}{2[r-(i-1)d]}ix^i}{\frac{d(2r-d)}{2r}+C\sum_{i=1}^{Nmax}\frac{d[2r-(2i-1)d]}{2[r-(i-1)d]}x^i}} \tag{7.16}$$

If the solid is characterized by a discrete size distribution of mesopores and N_r is the number of mesopores with radius r and same length L_m, the saturation capacity of the solid will be:

$$V_{s-tot} = V_{micro} + \sum_{i=1}^{n} V_{mesoi} = V_{micro} + L_m\pi\sum_{r_{min}}^{r_{max}} N_r r^2 \tag{7.17}$$

Where n is the total number of mesopores. The multilayer adsorbed amount for a solid characterized by a discrete distribution of mesopores N_r of different radius r and same length L will be:

$$V_{ml}(x) = \sum_{i=1}^{n} V_{mli} = \pi L_m d\sum_{r_{min}}^{r_{max}}\left[N_r(2r-d)\frac{C\sum_{i=0}^{Nmax}\frac{d[2r-(2i-1)d]}{2[r-(i-1)d]}ix^i}{\frac{d(2r-d)}{2r}+C\sum_{i=1}^{Nmax}\frac{d[2r-(2i-1)d]}{2[r-(i-1)d]}x^i}\right] \tag{7.18}$$

At a given value or relative pressure, each pore will eventually be filled with capillary condensed liquid. For the evaluation of the condensation pressure, the Kelvin equation can be used considering a cylindrical interface between the gas phase and the multilayer adsorbed phase as shown in fig. 7.20.

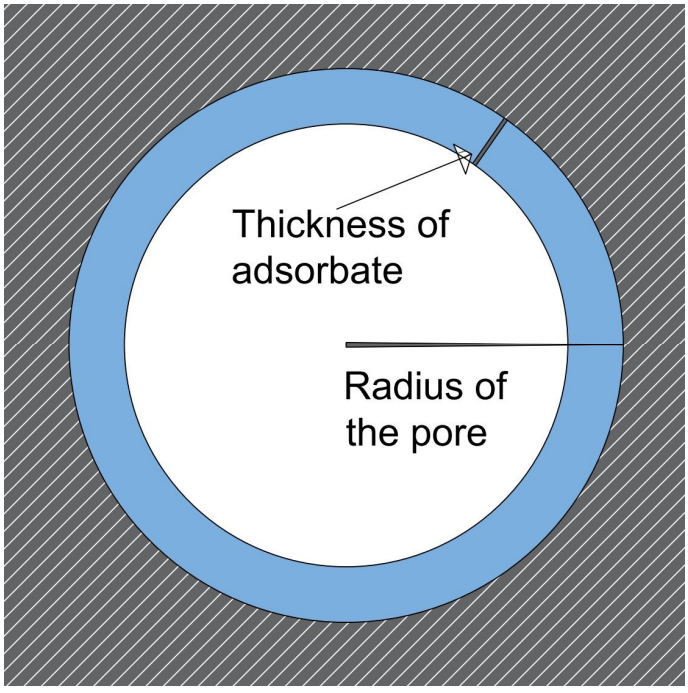

Figure 7.20 – Cylindrical meniscus of the multilayer adsorbed phase.

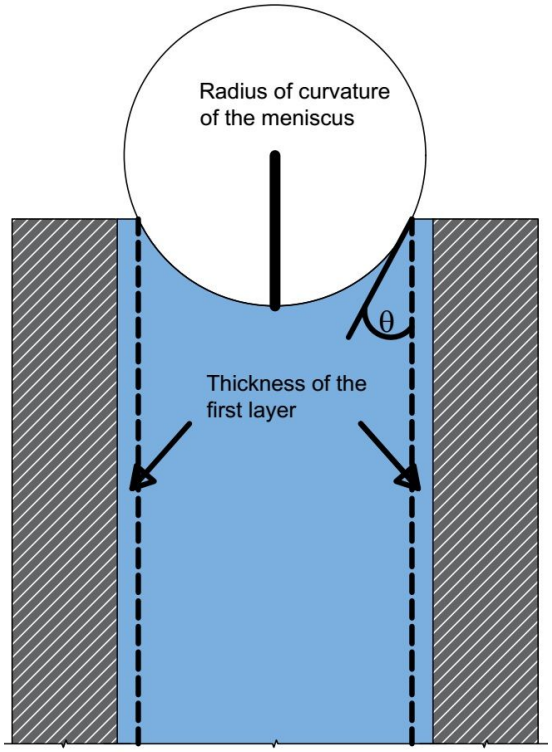

Figure 7.21 – Hemispherical meniscus of the capillary condensed phase

Therefore, the condensation pressure is obtained from:

$$\frac{\frac{dV}{dt(x)}}{\frac{dA}{dt(x)}} = -\frac{\gamma_s V_{mol}}{RTln(x)} \tag{7.19}$$

Where dV and dA are respectively the differential volume and the differential surface of the cylindrical meniscus. The derivative of the volume is given by:

$$\frac{dV}{dt(x)} = \frac{d\left(\pi L_m \left(r-t(x)\right)^2\right)}{dt(x)} = 2\pi L_m \left(r - t(x)\right) \tag{7.20}$$

The derivative of the surface is given by:

$$\frac{dA}{dt(x)} = \frac{d\left(2\pi L_m \left(r-t(x)\right)\right)}{dt(x)} = 2\pi L_m \tag{7.21}$$

As a result, the condensation pressures for each pore will be given by the solution of the following equation:

$$\frac{\frac{dV}{dt(x)}}{\frac{dA}{dt(x)}} = r - t(x) = -\frac{\gamma_s V_{mol}}{RTln(x)} \tag{7.22}$$

For the calculation of the evaporation pressure, the Kelvin equation can be used considering a hemispherical meniscus as shown in fig. 7.21. The evaporation pressure is obtained from:

$$\frac{\frac{dV}{d(r_m)}}{\frac{dA}{d(r_m)}} = -\frac{\gamma_s V_{mol}}{RTln(x)} \tag{7.23}$$

Where r_m is the radius of curvature of the meniscus. The derivative of the volume is given by:

$$\frac{dV}{d(r_m)} = \frac{d\left(4/3\pi {r_m}^3\right)}{d(r_m)} = 4\pi {r_m}^2 \tag{7.24}$$

The derivative of the surface is given by:

$$\frac{dA}{d(r_m)} = \frac{d\left(4\pi {r_m}^2\right)}{d(r_m)} = 8\pi r_m \tag{7.25}$$

As a result, the evaporation pressures for each pore will be given by the solution of the following equation:

$$\frac{\frac{dV}{d(r_m)}}{\frac{dA}{d(r_m)}} = \frac{r_m(x)}{2} = -\frac{\gamma_s V_{mol}}{RTln(x)} \tag{7.26}$$

Where $r_m(x)$ is given by:

$$\frac{r_m(x)}{2} = \frac{r}{2cos(\theta)} = -\frac{\gamma_s V_{mol}}{RTln(x)} \tag{7.27}$$

θ is the angle between the solid and liquid surface. If the first layer of adsorbate is assumed to behave as a stationary adsorbed layer, the evaporation pressure can be obtained from:

$$\frac{r_m}{2} = \frac{r-d}{2\,cos(\theta)} = -\frac{2\gamma_s V_{mol}}{RTln(x)} \tag{7.28}$$

In a particular concentration range, some of the pores will have a multilayer adsorbed phase and others a condensed liquid phase inside. To distinguish between the two groups, a function $r_c(x)$ is needed. This function gives the value of the pore radius condensing at each relative pressure x. If the solid is made of perfectly cylindrical independent pores, at a given pressure x, all the pores with a radius less or equal to $r_c(x)$ will be filled with capillary condensed liquid, while, the pores with a radius higher than $r_c(x)$ will have multilayer adsorbed phase. The same mechanism can be considered for the desorption using a similar function $r_e(x)$. To evaluate the functions $r_c(x)$ and $r_e(x)$, Eq. (7.22) and Eq. (7.28) can respectively be used. The volume of capillary condensed liquid inside the pores can be expressed as:

$$V_{cond} = \pi L_m \sum_{r_{min}}^{r_c(x)} N_r r^2 \tag{7.29}$$

Therefore, the total amount of adsorbate inside the mesopores is given by:

$$V_{total} = V_{ml}(x) + V_{cond} \tag{7.30}$$

Dividing the total amount of adsorbate in the mesopores by the total volume of the mesopores, the following expression for the relative amount adsorbed in the mesopores is obtained:

$$v_{ads-meso}(x) = \frac{d\sum_{r_c(x)}^{r_{max}}\left[N_r(2r-d)\frac{C\sum_{i=0}^{N_{max}}\frac{d[2r-(2i-1)d]}{2[r-(i-1)d]}ix^i}{\frac{d(2r-d)}{2r}+C\sum_{i=1}^{N_{max}}\frac{d[2r-(2i-1)d]}{2[r-(i-1)d]}x^i}\right]+\sum_{r_{min}}^{r_c(x)}N_r r^2}{\sum_{r_{min}}^{r_{max}}N_r r^2} \tag{7.31}$$

This can be rearranged by dividing both numerator and denominator by the total number of pores. In this way, the equation will contain the numerical fraction of pores of radius r as f_r rather than the absolute amount N_r. f_r can be considered as the pore size distribution of the solid.

$$v_{ads-meso}(x) = \frac{d\sum_{r_c(x)}^{r_{max}}\left[f_r(2r-d)\frac{C\sum_{i=0}^{N_{max}}\frac{d[2r-(2i-1)d]}{2[r-(i-1)d]}ix^i}{\frac{d(2r-d)}{2r}+C\sum_{i=1}^{N_{max}}\frac{d[2r-(2i-1)d]}{2[r-(i-1)d]}x^i}\right]+\sum_{r_{min}}^{r_c(x)}f_r r^2}{\sum_{r_{min}}^{r_{max}}f_r r^2} \tag{7.32}$$

The relative mass of adsorbate is obtained by multiplying and dividing Eq. (7.32) by the density of the adsorbed phase. The density of the multilayer adsorbed phase is assumed to be equal to the bulk liquid density ρ_0. The density of the capillary condensed phase is assumed to depend on the relative pressure according to the ideal liquid law [73]. The capillary condensed phase density reaches the bulk liquid density value when $p/p_0 = 1$. The relative liquid density ρ_r of the capillary condensed phase can be expressed as:

$$\rho_r(x) = \frac{\rho(x)}{\rho_0} = exp\left[\frac{\kappa\gamma}{-r_m(x)}\right] \tag{7.33}$$

Where $\rho(x)$ is the density of the capillary condensed phase as a function of the relative pressure x. κ is the isothermal compressibility of the liquid which, in this case, can be considered as a packing coefficient of the liquid condensed phase inside the solid. γ is the surface tension at the interface. r_m is the radius of curvature of the meniscus expressed in Eq. (7.27). For a real solid, the pore size distribution will be a discrete stepwise function. However, for practical aims, the discrete pore size distribution can be approximated with a continuous function f_r and the sum operator can be substituted with a continuous integral as follows:

$$m_{ads-meso}(x) = \frac{d\int_{r_c(x)}^{r_{max}}f_r(2r-d)\frac{C\sum_{i=0}^{N_{max}}\frac{d[2r-(2i-1)d]}{2[r-(i-1)d]}ix^i}{\frac{d(2r-d)}{2r}+C\sum_{i=1}^{N_{max}}\frac{d[2r-(2i-1)d]}{2[r-(i-1)d]}x^i}dr+\rho_r(x)\int_{r_{min}}^{r_c(x)}f_r r^2 dr}{\int_{r_{min}}^{r_{max}}f_r r^2 dr} \tag{7.34}$$

The desorption branch can be defined in the same way by substituting $r_e(x)$ to $r_c(x)$. If the solid contains also micropores, the Langmuir equation can be introduced for a better prediction of the adsorbed amount at low pressures. The amount adsorbed in the micropores can be expressed as:

$$m_{ads-micro}(x) = m_{s-micro}\frac{K_L x}{\frac{1}{p_0}+K_L x} \tag{7.35}$$

The total relative amount adsorbed in the solid is given by:

$$m_{ads}(x) = \frac{m_{s-micro}\frac{K_L x}{\frac{1}{p_0}+K_L x} + d\int_{r_c(x)}^{r_{max}} f_r(2r-d)\frac{C\sum_{i=0}^{Nmax}\frac{d[2r-(2i-1)d]}{2[r-(i-1)d]}ix^i}{\frac{d(2r-d)}{2r}+C\sum_{i=1}^{Nmax}\frac{d[2r-(2i-1)d]}{2[r-(i-1)d]}x^i}dr + \rho_r(x)\int_{r_{min}}^{r_c(x)} f_r r^2 dr}{m_{s-micro}\frac{K_L}{\frac{1}{p_0}+K_L} + \int_{r_{min}}^{r_{max}} f_r r^2 dr} \tag{7.36}$$

Where $m_{s-micro}$ is the capacity of the micropores and K is the equilibrium constant. Eq. (7.36) is similarly structured to other models already present in the literature [55,74]. However, the model presented in Eq. (7.36) is more detailed and the complete analytical expression is reported. The model includes the possibility of having micropores in the solid structure as in the case of SBA-15 and its applicability can be extended to other adsorptives other than water. The multilayer adsorption is limited by the size of the cylindrical pore and it is also consistent with the cylindrical surface and pore size distribution of the mesopores. In addition, the increase in the adsorbed amount after the capillary condensation can be predicted by the shrinkage or expansion of the liquid condensed phase.

The model is very accurate and flexible and it can predict type IV and type V isotherms for vapors adsorption in perfect cylindrical pores. Some assumptions can be made to obtain a simpler analytical expression, while the model can still provide an excellent correlation of the experimental data. The multilayer adsorption can be assumed to occur on a surface which constantly decreases by a factor J [69]. For the case of water vapour adsorption on SBA, the most of the microporosity of the solid is lost during the first experiment on a fresh sample. Therefore, considering only the adsorption in the mesopores can provide a good prediction of the experimental data. According to these assumptions, Eq. (7.36) can be modified to provide the amount of water adsorbed as:

$$\frac{m_{ads}(x)}{m_{sat}} = \frac{d\frac{Cx}{(1-Jx)[1+(C-1)x]}\int_{r_c(x)}^{r_{max}} f_r(2r-d)dr + \rho_r(x)\int_{r_{min}}^{r_c(x)} f_r r^2 dr}{\int_{r_{min}}^{r_{max}} f_r r^2 dr} \tag{7.37}$$

$$\frac{m_{ads}(x)}{m_{sat}} = \frac{d\frac{Cx}{(1-Jx)[1+(C-1)x]}\int_{r_c(x)}^{r_{max}} f_r(2r-d)dr}{\int_{r_{min}}^{r_{max}} f_r r^2 dr} \tag{7.37a}$$

Where m_{sat} is the amount adsorbed at saturation and $m_{ads}(x)$ is the amount adsorbed. The prediction of the model expressed in Eq. (7.37a) for the multilayer adsorption part of the isotherm is shown in fig. 7.22.

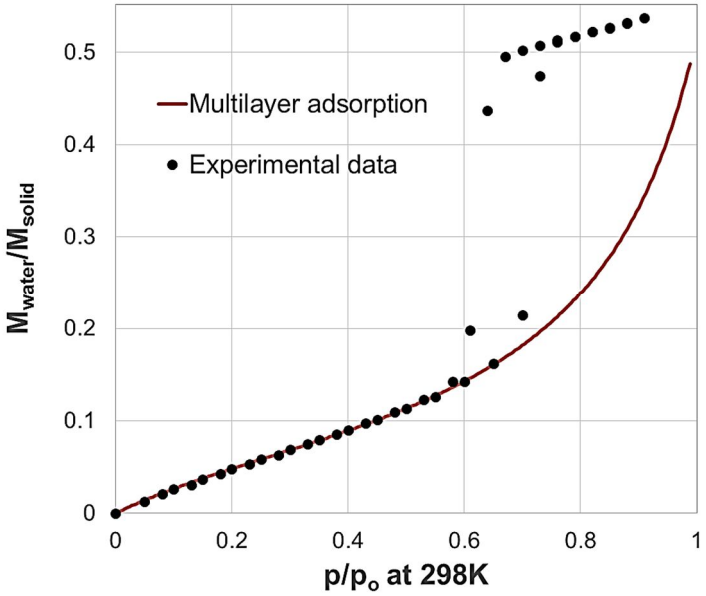

Figure 7.22 – Experimental adsorption-desorption equilibrium isotherm for water vapor on SBA-15 and prediction of the multilayer adsorbed amount.

Equation (37) does not consider the empty hemispherical volumes generated by the equilibrium liquid menisci at the two ends of the pores. For SBA-15, these volumes are negligible as the diameter of the pores is much smaller than the pores lengths [17]. In a scenario in which the menisci volumes are not negligible compared to the total volume of the pores, Eq. (7.35) needs to be modified. If the first layer of adsorbate is assumed to behave as a stationary adsorbed layer, the distance $h(x)$ in between the pore end and the lowest point of the liquid meniscus is given by:

$$h(x) = r_m(x) - \sqrt{r_m(x)^2 - (r-d)^2} \tag{7.38}$$

The empty volume of the hemispherical menisci at the pore ends can be expressed as:

$$V_{menisci}(x) = \frac{2\pi}{3}\int_{r_{min}}^{r_c(x)} f_r h(x)^2\big(3r_m(x) - h(x)\big)dr \tag{7.39}$$

Therefore, Eq. (7.37) can be simply rearranged and expressed as:

$$\frac{m_{ads}(x)}{m_{sat}} = \frac{d\frac{Cx}{(1-Jx)[1+(C-1)x]}\int_{r_c(x)}^{r_{max}} f_r(2r-d)dr + \rho_r(x)\int_{r_{min}}^{r_c(x)} f_r\left[r^2 - 2\frac{h(x)^2}{3L_m}\big(3r_m(x)-h(x)\big)\right]dr}{\int_{r_{min}}^{r_{max}} f_r r^2 dr} \tag{7.40}$$

Where L_m is the pore length and, therefore, one more parameter is introduced in the model.

7.6 Mathematical derivation of the quasi-independent pores model

The adsorption model for perfectly cylindrical independent pores can be modified to consider the converging behavior of the experimental scanning curves. This kind of scanning curves is typical of disordered solids characterized by a pore structure made of interconnected channels or pore networks [30,48]. However, considering the pore structure of SBA-15, a three-dimensional pore network effect can certainly be excluded for such a solid. Also, the eventual microporous connections between the mesoporous cylindrical channels are permanently filled with strongly adsorbed water as discussed beforehand. The most likely theoretical explanation able to predict the non-crossing behavior of the scanning curves is given by the presence of cylindrical constrictions along the longitudinal axis of the pore. Therefore, the solid can be assumed as made of n non-perfectly cylindrical main mesopores. Each single main mesopore of average radius $\bar{r}$ can be considered as an ensemble of N cylindrical sub-pores or constrictions of different radius r and same length L_m . In this view, the mechanisms of adsorption and desorption can be represented as in figs 7.23-7.24.

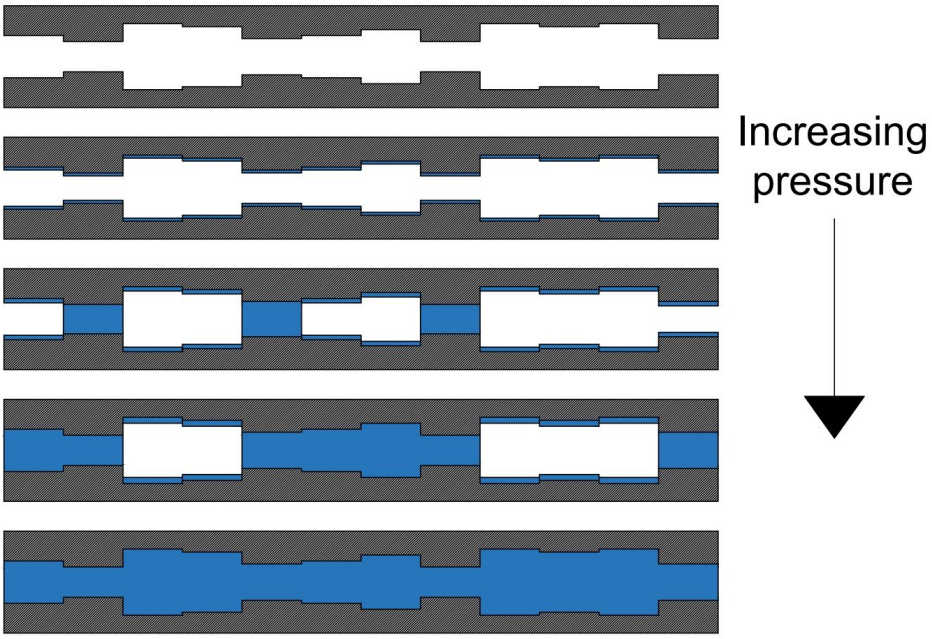

Figure 7.23 – Representation of the adsorption-condensation mechanism when increasing the partial pressure of water vapor.

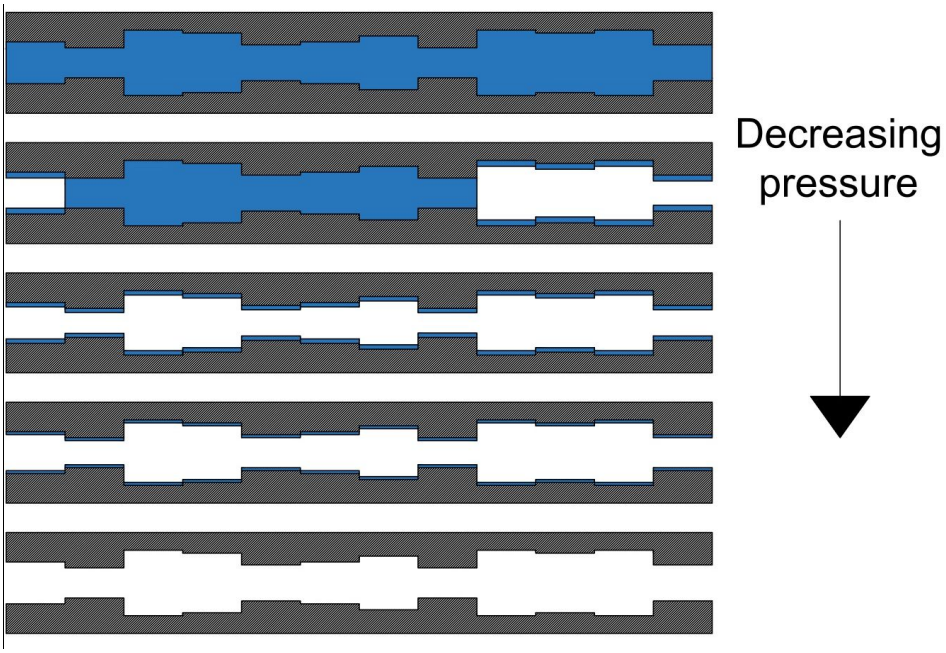

Figure 7.24 – Representation of the desorption-evaporation mechanism when decreasing the partial pressure of water vapor

In such a scenario Eq. (7.37) can be rewritten as:

$$\frac{m_{ads}(x)}{m_{sat}} = \frac{d\frac{cx}{(1-Jx)[1+(c-1)x]}\sum_{i=0}^{n} f_i \sum_{j=0}^{N} g_j F_j (2r_j - d) + \rho_r \sum_{i=0}^{n} f_i \sum_{j=0}^{N} g_j (1-F_j) r_j^2}{\sum_{i=0}^{n} f_i \sum_{j=0}^{N} g_j r_j^2} \tag{7.41}$$

Where f is the size distribution of the main mesopores, g is the sub-pores size distribution and F is a function that can assume only two values: 1 for the non-condensed pores and 0 for the condensed pores. The function F is designed to consider the adsorption-condensation and the desorption-evaporation mechanisms. The latter also includes the pore blocking effect. The role of the function F was introduced in the previous section.

7.7 Silica-gel: Pore network and percolation model

The formulation of the equilibrium model for independent pores expressed in Eq. (7.37) can be used to predict also the experimental adsorption-desorption isotherm of water vapor on silica-gel. The experimental data for water vapor on silica-gel is reported and discussed in chapter 7. From the experimental equilibrium isotherm, it is possible to observe that the adsorption and the desorption branches are not parallel due to the pore blocking effect acting on the desorption branch. Therefore, the first model expressed in Eq. (7.37) could still be applied for the prediction of the data if two different pore size distributions are considered for the adsorption and desorption branch. However, this would result in an inconsistent prediction of the experimental data.

For a rigorous formulation of a consistent adsorption-desorption equilibrium model for water vapor on silica-gel, the pore blocking effect resulting in the percolation desorption mechanism must be considered for both the desorption branch and for the desorption scanning curves. Pore blocking effects, which are typical of solids made of interconnected pores in a disordered network, have been widely investigated in the literature [75–82]. The resulting percolation phenomena have been modeled using either probabilistic Monte Carlo approaches in regular lattices or analytical solutions for Bethe lattices.

The use of Bethe lattices permits to have analytical functions which correlate the fraction of sites (pores for adsorption) which is actually empty to the fraction of pores which would be empty if all the sites had access to the vapor phase. These analytical functions depend on the coordination number of the lattice and on the initial fraction of empty pores. The coordination number is the number of pores interconnected at each node. For the main desorption curve, the initial fraction of empty pore is zero while for the secondary desorption curves (desorption scanning curves) the initial fraction of empty pores depends on the starting point of the curve located on the adsorption branch. In the latest formulation of the analytical solution of the Bethe lattice [76], the possibility of vapor nucleation has been included for both main desorption and secondary desorption scanning curves. The vapor nucleation can be either homogeneous or heterogeneous. The nucleation is the formation of a vapor phase inside the liquid phase due to the approach of the thermodynamic stability limit of the liquid phase. The phenomenon of nucleation has been later investigated using approaches based on molecular dynamics and grand canonical Monte Carlo simulations. These studies have confirmed the possibility that density fluctuations in the liquid phase can give birth to a cavitation phenomenon and formation of a vapor phase inside an existing liquid phase. This phenomenon eventually represents the emptying process of the pore [45,83]. The evidence of cavitation phenomena has also been confirmed experimentally [84].

In the current derivation, the adsorption branch can still be considered as made of independent pores in which the vapor condenses at a value of pressure characteristic of the dimensions of the isolated pore. As a starting point, it is interesting to use the equilibrium model expressed in Eq. (7.37) for the prediction of the experimental adsorption and desorption data of water vapor on silica gel. The parameters of the model and the pore size distribution can be tuned for the prediction of the adsorption branch and the resultant desorption branch can be visualized in fig. 7.25. In this scenario, the desorption branch is defined as the one resulting from the hysteresis in the single isolated pores while the percolation-desorption branch is defined as the one which includes also the percolation desorption mechanism in the pore network.

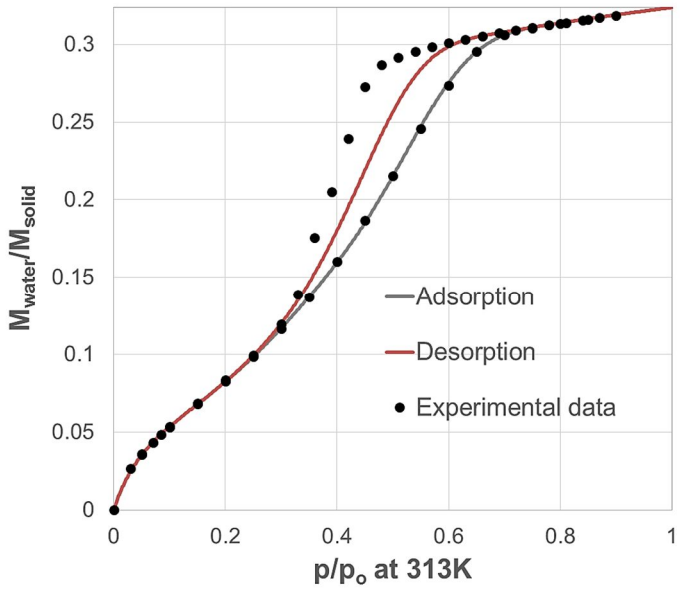

Figure 7.25 – Experimental adsorption-desorption equilibrium isotherm for water vapor on silica-gel and correlation of the model for independent pores (Eq. 7.1).

For the implementation of the percolation theory, several functions must be introduced and defined. The fraction of empty pores along the adsorption branch which also corresponds to the fraction of empty pores at the beginning of a desorption curve can be defined as:

$$p_{ads}(x) = 1 - \frac{m_{ads}(x) - m_{ads}(x_{c_{min}})}{m_{max}(x) - m_{ads}(x_{c_{min}})} \tag{7.42}$$

Where x is the relative equilibrium pressure, $m_{ads}(x)$ is the equilibrium isotherm relative to the adsorption branch, $m_{ads}(x_{c_{min}})$ is the amount adsorbed at the lowest relative condensation pressure $x_{c_{min}}$ and $m_{max}(x)$ is the saturation amount adsorbed which also depends on the partial pressure of water. According to Eq. (7.37), $m_{max}(x)$ can be expressed as:

$$m_{max}(x) = m_{sat}\rho_r(x) \tag{7.43}$$

The function $m_{max}(x)$ is shown in fig. 7.26. The fraction of empty pores along the desorption branch can be defined in a similar manner as:

$$p_{des}(x) = 1 - \frac{m_{des}(x) - m_{des}(x_{e_{min}})}{m_{max}(x) - m_{des}(x_{e_{min}})} \tag{7.44}$$

Where $m_{des}(x)$ is the equilibrium isotherm relative to the desorption branch, $m_{des}(x_{e_{min}})$ is the amount desorbed at the lowest relative evaporation pressure $x_{e_{min}}$. $p_{des}(x)$ represents the fraction of pores that would be empty if they had access to the vapour phase. The analytical solution of the percolation theory in a Bethe lattice gives the fraction of pores which are actually empty for a given value of $p_{des}(x)$, initial fraction of empty pores $p_{ads}(x_0)$ and fraction of

pores f_c which undergo a liquid-vapour transition via nucleation or cavitation. The analytical solution is called accessibility function $P_{des}(x)$ and for a bond percolation desorption mechanism is given by:

$$P_{des}(x) = p_{des}(x) - (1 - f_c)\left(p_{des}(x) - p_{ads}(x_{0des})\right)\left[\frac{1-p_{des}(x)}{1-X_{aux}}\right]^{2(z-1)} \tag{7.45}$$

Where x_{0des} is the concentration in the gas phase at the starting point of the percolation-desorption curve, z is the coordination number of the lattice and X_{aux} is the solution in the interval $\left[0, \frac{1}{z-1}\right]$ of the following auxiliary equation:

$$X_{aux}(1 - X_{aux})^{z-2} - (1 - f_c)\left(p_{des}(x) - p_{ads}(x_{0des})\right)\left(1 - p_{des}(x)\right)^{z-2} \tag{7.46}$$

For the main percolation-desorption curve $p_{ads}(x_{0des})$ is equal to zero while for the secondary desorption scanning curves $p_{ads}(x_{0des})$ depends on the starting point x_{0des} of the particular desorption scanning curve, located on the adsorption branch. For the adsorption scanning curves, the initial fraction of empty pores is given by $P_{des}(x_{0ads})$ where x_{0ads} is the concentration in the gas phase at the beginning of the adsorption scanning curve, located on the percolation-desorption curve. The fraction of empty pores along an adsorption scanning curve can be calculated as:

$$P_{ads}(x) = \frac{P_{des}(x_{0ads})}{p_{ads}(x_{0ads})} p_{ads}(x) \tag{7.47}$$

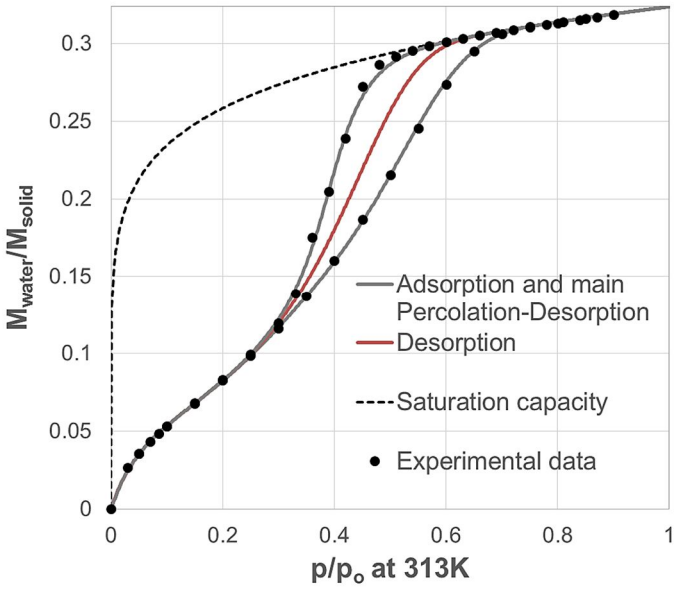

Figure 7.26 – Experimental adsorption-desorption equilibrium isotherm for water vapor on silica-gel and correlation of the model for independent pores (adsorption-desorption) and percolating pore network (percolation-desorption).

The calculated accessibility functions for the main percolation-desorption branch, desorption scanning curves, and adsorption scanning curves can then be used for the calculation of the corresponding amount adsorbed. The amount adsorbed along the main percolation-desorption branch can, therefore, be calculated as:

$$m_{p-des}(x) = m_{des}(x_{e_{min}}) + (1 - P_{des}(x))\left(m_{max}(x) - m_{des}(x_{e_{min}})\right) \tag{7.48}$$

The calculation of the percolation-desorption branch in shown in fig. 7.26. For the calculation of the accessibility function relative to the desorption scanning curves, the fraction of pores allowed to empty is given by Eq. (7.42) while the fraction of pores which are actually empty is given by Eq. (7.45). Therefore, the amount adsorbed along the desorption scanning curves can be calculated as:

$$m_{des-scan}(x) = m_{ads}(x_{c_{min}}) + (1 - P_{des}(x))\left(m_{max}(x) - m_{ads}(x_{c_{min}})\right) \tag{7.49}$$

The amount adsorbed along the adsorption scanning curves can be calculated as:

$$m_{ads-scan}(x) = m_{des}(x_{e_{min}}) + (1 - P_{ads}(x))\left(m_{max}(x) - m_{des}(x_{e_{min}})\right) \tag{7.50}$$

The prediction of the adsorption and desorption scanning curves is shown respectively in fig. 7.27 and fig. 7.28.

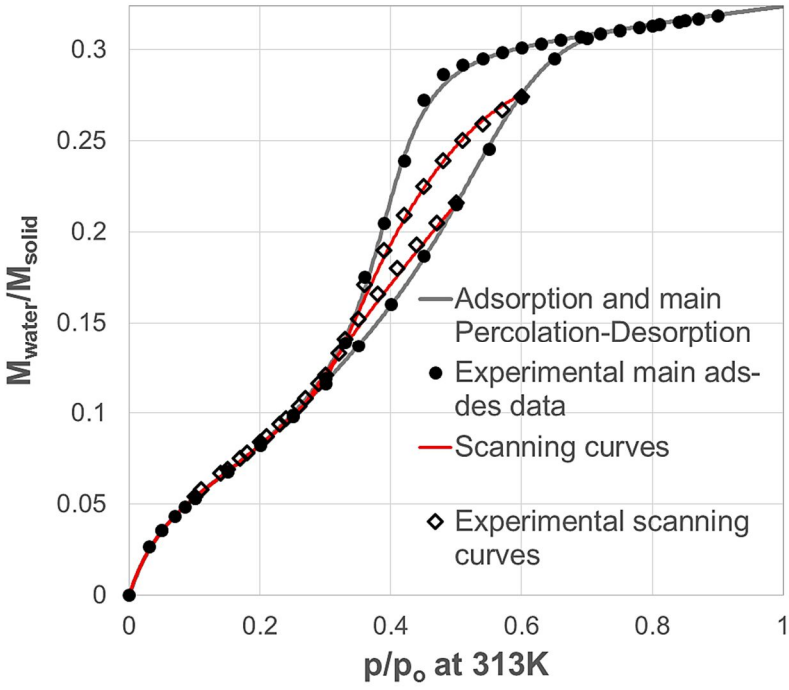

Figure 7.27 – Experimental adsorption-desorption equilibrium isotherm and desorption scanning curves for water vapor on silica-gel and correlation of the model for percolating pore network.

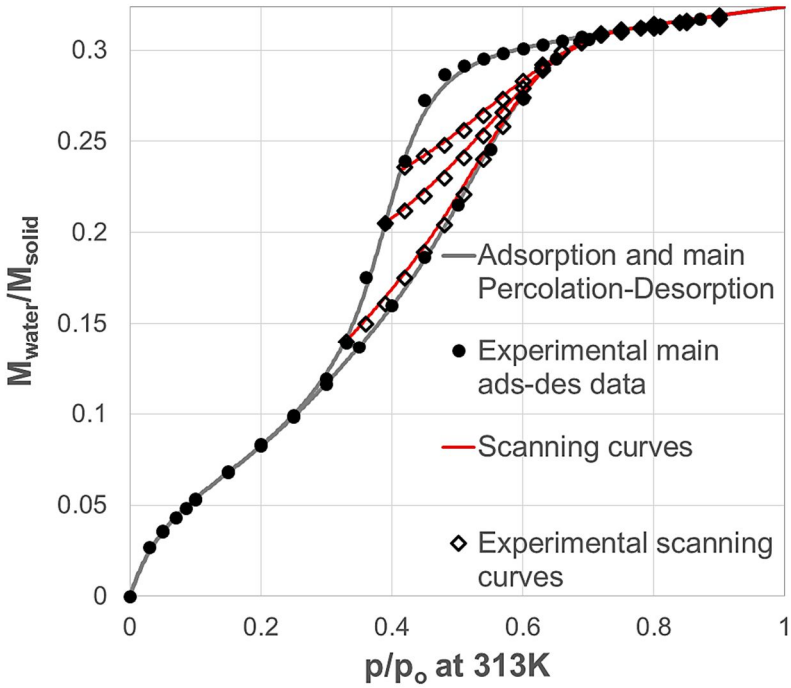

Figure 7.28 – Experimental adsorption-desorption equilibrium isotherm and adsorption scanning curves for water vapor on silica-gel and correlation of the model for percolating pore network.

For the case of water vapor on silica-gel, the multilayer adsorption region can be better represented by using the latest modification of the BET model [46]. This model considers a limited number of permitted adsorbed layers inside the pore and a different heat of adsorption for the last adsorbed layer due to the interaction with the layer adsorbed on the opposite wall. The model is expressed as:

$$V_{ml}(x) = V_m \frac{Cx}{(1-x)} \frac{1+(0.5n_{max}g-n)x^{nmax-1}-(n_{max}g-n_{max}+1)x^{nmax}+0.5n_{max}gx^{nmax+1}}{1+(C-1)x+(0.5Cg-C)x^{nmax}-0.5Cgx^{nmax+1}} \tag{7.51}$$

In this scenario, Eq. (7.37) can be expressed as:

$$m_{ads}(x) = m_{sat} \frac{d\frac{Cx}{(1-x)}\frac{1+(0.5n_{max}g-n)x^{nmax-1}-(n_{max}g-n_{max}+1)x^{nmax}+0.5n_{max}gx^{nmax+1}}{1+(C-1)x+(0.5Cg-C)x^{nmax}-0.5Cgx^{nmax+1}}\int_{r_c(x)}^{r_{max}} f_r(2r-d)dr+\rho_r(x)\int_{r_{min}}^{r_c(x)} f_r r^2 dr}{\int_{r_{min}}^{r_{max}} f_r r^2 dr} \tag{7.52}$$

Where n is the maximum number of adsorbed layers permitted inside the pore and g is an energetic term which can be expressed similarly to C as:

$$g = exp\left(\frac{Q}{RT}\right) \tag{7.53}$$

Where Q is the difference between the heat of adsorption in the last layer and the heat of condensation which, in the BET theory, is considered equal to the heat of the adsorption of a molecule adsorbing on an already adsorbed molecule. According to Eq. (7.51), the predicted multilayer adsorption is shown in fig. 7.29.

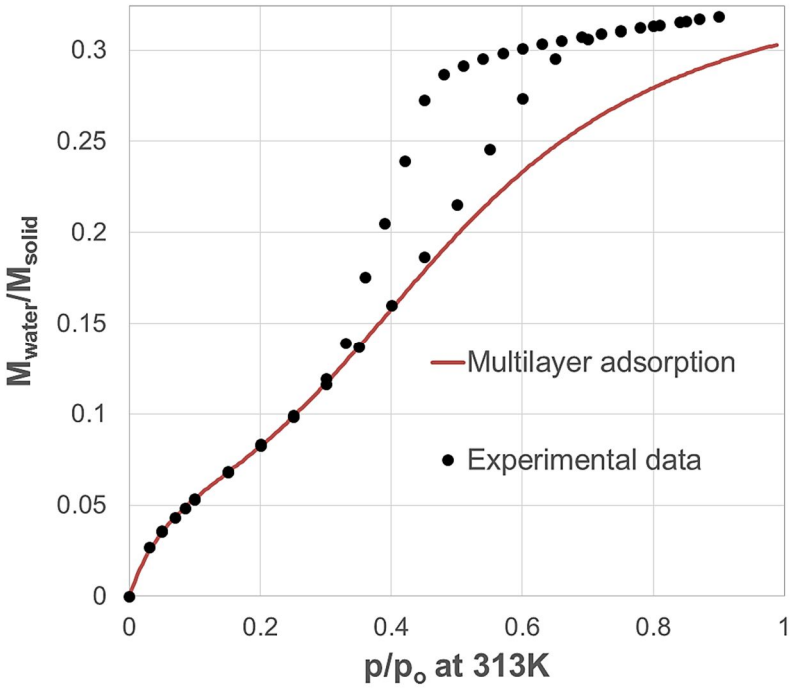

Figure 7.29 – Experimental adsorption-desorption equilibrium isotherm for water *vapor* on silica gel and correlation of the multilayer adsorbed amount.

The parameters of the equilibrium model expressed in Eq. (7.52), used for the regression of the experimental data shown in figs 7.25-7.29, are reported in table 7.4.

Table 7.4 – Parameters used for the regression of the experimental data with the model given by Eq. (7.52).

	313K
d **(nm)**	0.166
n_{max}	4.46
C	14.4
g	23.5
$\theta°$	20
r_{min} **(nm)**	0.7
r_{max} **(nm)**	2.2
σ $pores$	0.191
μ $pores$	0.204
m_{sat} **(g/g)**	0.324
κ **(Pa^{-1})**	$1.95*10^{-9}$
$z-perc.main\ desorption$	3
$z-des.scanning\ curve\ 1$	2.2
$z-des.scanning\ curve\ 2$	1.9
$f_c-perc.main\ desorption$	0.11
$f_c-des.scannig\ curve\ 1$	0
$f_c-des.scanning\ curve2$	0

From table 7.4 it is possible to observe that a different value of coordination number z is required for each desorption curve. This parameter can therefore be considered more as a fitting parameter rather than a realist coordination number for the lattice.

7.8 Conclusions

The experimental data are correlated using two different analytical models. The first model assumes independent and perfectly cylindrical pores. This model can predict the main adsorption and desorption branches in the entire range of concentration at different temperatures. However, the model fails to qualitatively and quantitatively predict the scanning curves inside the hysteresis loop. For a solid made of perfectly cylindrical independent pores, the scanning curves are theoretically supposed to exhibit a crossing behavior. However, the experimental scanning curves showed a crossing behavior at first and a converging trajectory when approaching the opposite branch of the isotherm. This phenomenon can be predicted if one assumes imperfect cylindrical pores. In such a case, each pore can be considered as an ensemble of cavities and constrictions. An appropriate and expedient method to model such imperfection is to assume a normal distribution of cylindrical sub-pores inside each main pore. This would give rise to a different desorption and adsorption mechanism which is able to qualitatively predict the converging behavior of both the desorption and the adsorption scanning curves. Based on these assumptions, the second formulation of the model can be considered as an extension of the first model in which the advanced condensation and pore blocking phenomena were included. The second model can be successfully used for the prediction of both the main adsorption and desorption curves and the scanning curves.

For the prediction of water vapor on silica-gel experimental isotherms, the first formulation of the equilibrium model in Eq. (7.37) can still be used. In such a scenario two distinct pore size distributions are needed for the adsorption and desorption branch of the isotherm. A more rigorous model was developed considering the actual pore structure of the solid. In this view, the equilibrium models were extended to consider the pore blocking effect and percolation desorption mechanism for the desorption branch and desorption scanning curves. The relatively simple analytical expressions of the equilibrium models investigated in this chapter can allow their implementation in adsorption simulation software packages.

8 Equilibrium measurements

8.1 Gravimetric system

8.1.1 SBA-15: Stability of the solid and reproducibility of the equilibrium isotherm

In this paragraph, the possible structural modifications which characterize SBA-15 in contact with high concentrations of water vapor were investigated. Particular attention was given to the stability of the solid after several repeated water vapor adsorption-desorption experiments. To support our considerations, experimental adsorption and desorption isotherms of vapor water on SBA-15 at the three different temperatures of 288 K, 298 K, and 308 K were measured. Full adsorption-desorption cycles up to 90% of humidity were measured. The experimental data also includes scanning desorption and adsorption curves.

Two complete adsorption-desorption isotherms were measured at three different temperatures of 288 K, 298 K, and 308 K. A complete adsorption-desorption isotherm with two scanning desorption curves and two scanning adsorption curves were measured at 298 K. The complete adsorption-desorption cycles were repeated several times on the same sample at 308 K to check for some modification of the solid. The first experimental runs were meant to evaluate the stability of SBA-15 in contact with a high concentration of water vapor and the eventual reproducibility of the adsorption equilibrium isotherm. The relative amount adsorbed was calculated as:

$$M_a = \frac{m_s - m_{dry}}{m_{dry}} \tag{8.1}$$

Where m_s is the mass of the sample on the crucible and m_{dry} is the mass of the dry sample at the beginning of the experiments. Fig. 8.1 shows the first adsorption-desorption run on a fresh sample immediately after the activation. The hydrophobic nature of the silica surface is visible from the shape of the adsorption isotherm at low concentrations. The adsorption branch of the isotherm is characterized by an almost linear region going from zero loading up to the onset of the capillary condensation. This clearly results in a low value for the Henry's law constant. The first adsorption-desorption cycle clearly shows that the desorption curve does not reach the initial dry state. This is the first indication that some water is strongly adsorbed and/or trapped inside the solid during the first experiment on a fresh sample.

Two more experimental runs were performed immediately afterward on the same sample using the same temperature and concentration steps. For each of the following experiments, the sample was regenerated at 393 K for 3 h under a nitrogen purge flow.

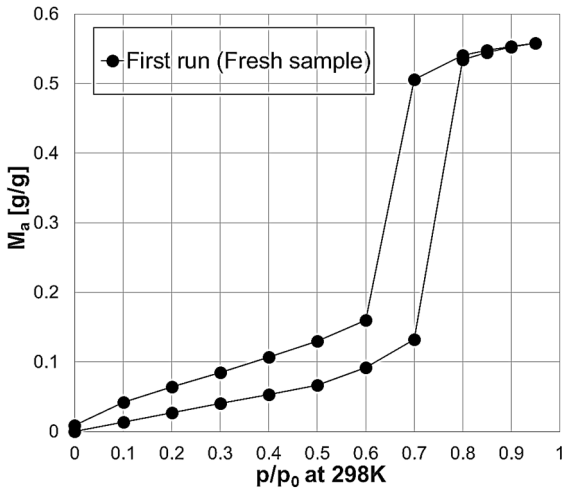

Figure 8.1 – Adsorption-Desorption data on SBA-15 fresh sample at 298 K. The continuous lines are only a guide for the eyes.

Fig. 8.2 shows all the water adsorption-desorption experiments performed on the same sample. The second and the third run are reproducible and confirm that some water is strongly adsorbed and cannot be removed by simply degassing the solid with pure nitrogen or by increasing the temperature up to 393 K. The initial mass of the solid at the beginning of the second and the third run increased compared to the dry mass of the fresh sample used in the first run by approximately 1 %, see fig. 8.1 The dry mass of the fresh sample was used as dry mass for all the following runs to have a consistent comparison between the experiments. In contrast to the first experiment on the fresh sample, the successive experiments show complete reversibility of the isotherm.

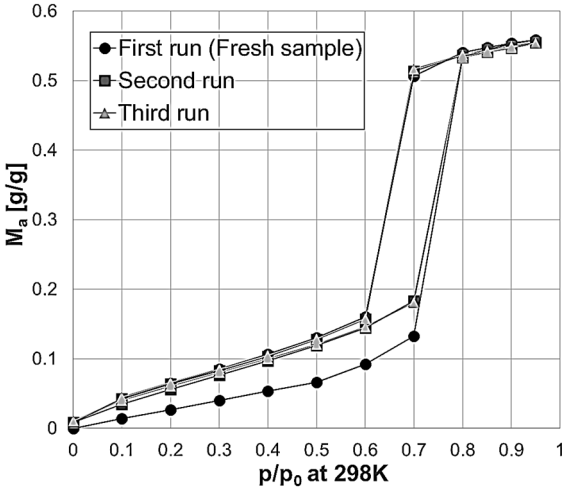

Figure 8.2 – Adsorption-Desorption data on SBA-15 fresh sample and replications on the same sample at 298 K. The continuous lines are only a guide for the eyes.

A possible explanation for these results is that some water is trapped inside the microporous regions of the solid. After the first experimental run, these regions are no longer available for reversible adsorption. To test this hypothesis, Ar isotherms at 87 K were measured as shown in Fig. 8.3. The pore size distribution (PSD) for each sample (fresh and used) was calculated from the equilibrium branch using the NLDFT (Non-Local Density Functional Theory) method (Argon at 87 K zeolites/silica, spherical/cylindrical pore, equilibrium) [85]. The corresponding results are shown in Fig. 8.4.

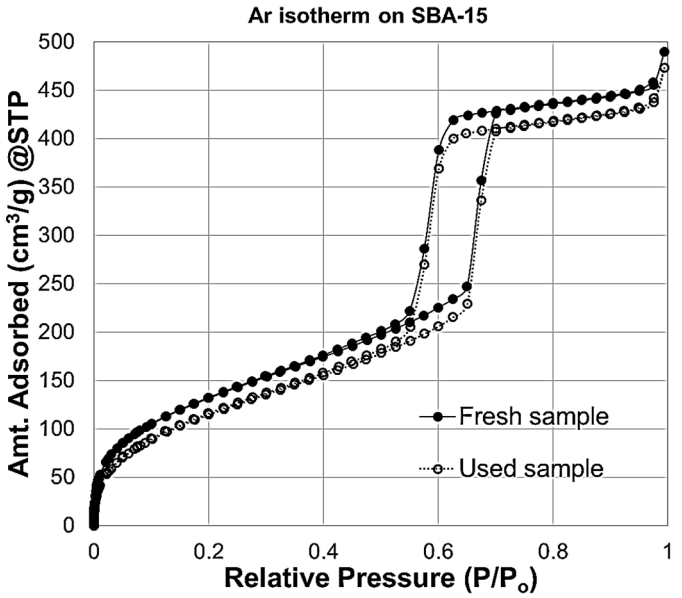

Figure 8.3 – Adsorption-Desorption data for Ar on SBA-15 fresh sample and water-used sample. The continuous lines are only a guide for the eyes.

The mesoporous volumes of the two samples are practically the same, while there is a clear difference in the microporous region as shown more clearly in Fig. 8.5.

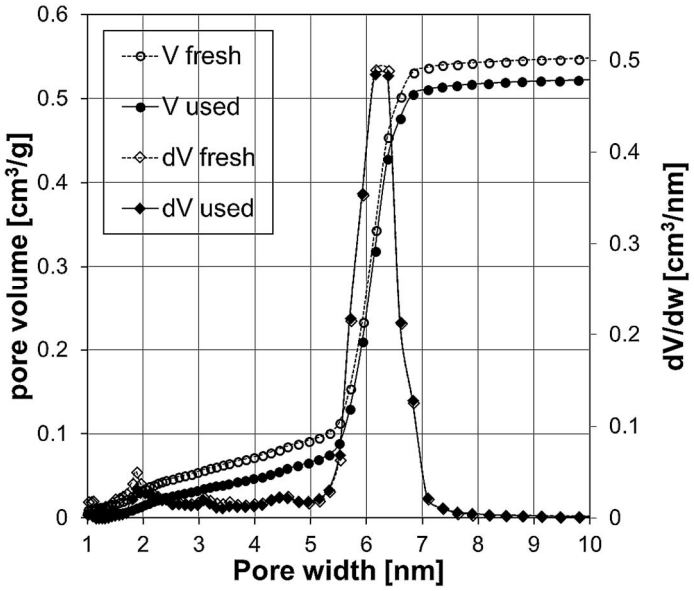

Figure 8.4 - Comparison between the fresh sample and the water-used sample. PSD and pore volume of SBA-15 from argon adsorption-desorption at 87 K.

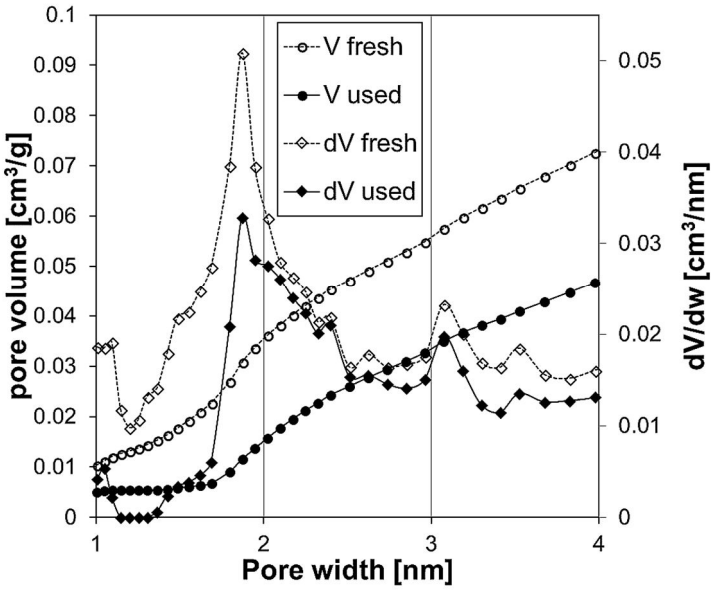

Figure 8.5 - Comparison between the fresh sample and the water-used sample. PSD of the microporous region.

It is interesting to note that in our study the mesopore volume remains unchanged and, therefore, we can exclude that some of the mesopores collapsed. Other studies reported in the literature [19,20,22] observed some loss of mesopore volume resulting from water adsorption. What remains to be determined is whether the entrapment of water is achieved at low partial pressures or if it required that the water molecules need to be in the capillary condensed state. It has been suggested in the literature [19] that the reaction between water and the solid surface occurs during or after the capillary condensation process. This hypothesis can be confirmed by running an adsorption and desorption cycle on a fresh sample but limiting the vapor pressure so that the onset of capillary condensation is avoided. The results for this experiment can be observed in fig. 8.6, together with the first complete adsorption-desorption cycle. The reversibility of the experimental data when the onset of capillary condensation is avoided confirms the fact that in order to understand the water adsorption isotherm on SBA-15 a knowledge of the history of the sample is required.

It is also important to note the fact that reproducible isotherms are obtained, after the first occurrence of the hysteresis loop, indicating that in practical applications one needs to consider only the water that is reversibly adsorbed. To confirm the stability of the material and the reproducibility of the isotherm, a complete adsorption-desorption experiment was performed on a sample two months after the first experiment, as shown in fig. 8.7. This sample was used in five different adsorption-desorption cycles before the repeated experiment. The isotherm is unchanged from zero loading to the full saturation of the pores.

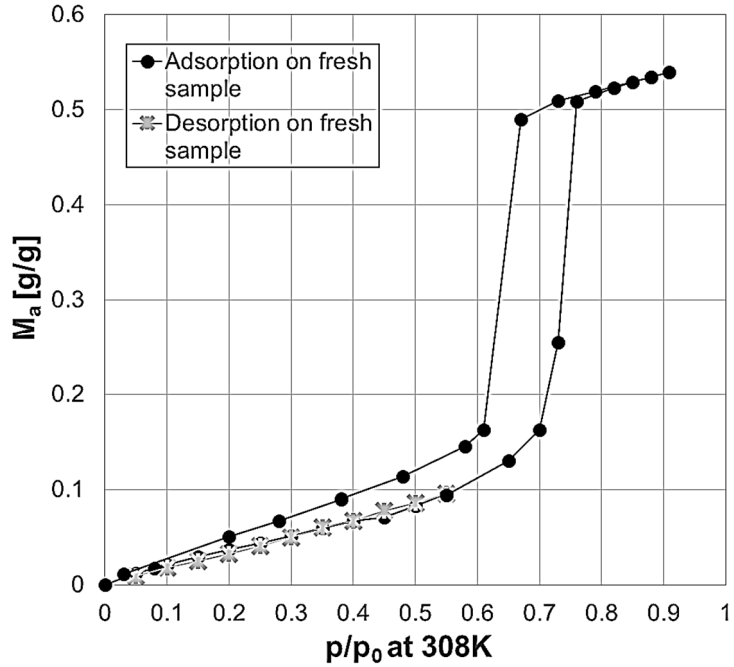

Figure 8.6 – Adsorption-Desorption data on SBA-15 fresh sample at 308 K. The continuous lines are only a guide for the eyes.

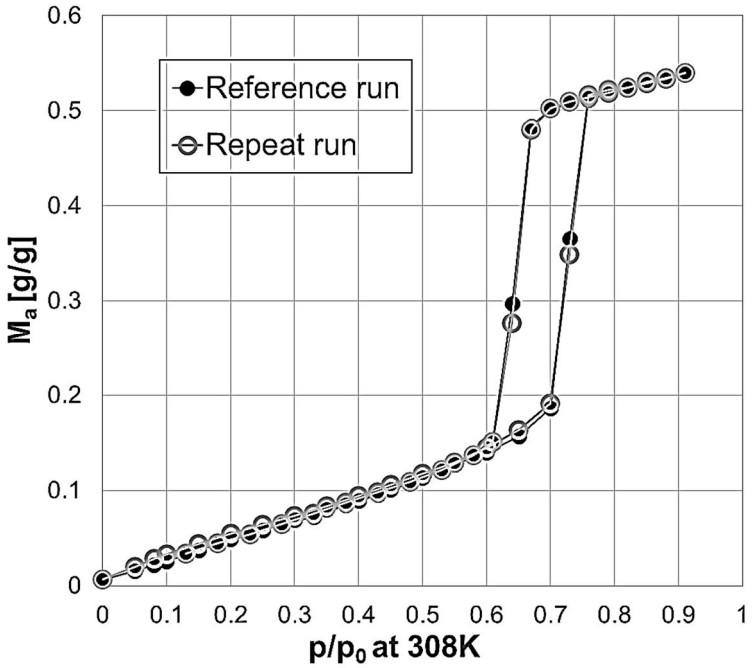

Figure 8.7 – Long-term stability test for water vapor adsorption on SBA-15 at 308 K.

To sum up, the equilibrium adsorption-desorption isotherms for water vapour on SBA-15 are characterized by three main aspects: a moderately high hydrophobicity which results in a small amount adsorbed at low concentrations, almost stepwise capillary condensation and evaporation branches in the hysteresis region, and the irreversible adsorption of some water within the micropores in the first condensation loop.

8.1.2 SBA-15: Adsorption and desorption scanning curves

Once the stability of SBA-15 for repeated water adsorption-desorption cycles was assessed, the attention was focused on the study of the scanning behavior of the hysteresis region. It is important to point out that in the case of almost vertical adsorption and desorption branches a slight change in the gas phase concentration can cause a sudden increase in the amount adsorbed. Therefore, it is not straightforward to choose the starting point for a scanning curve *a priori*. Several runs need to be performed to evaluate the appropriate concentration and equilibration time for the starting points. In addition, the hysteresis region is the irreversible part of the isotherm, and it is important to have a stable concentration of water in the gas phase to avoid an irreversible change in the amount adsorbed.

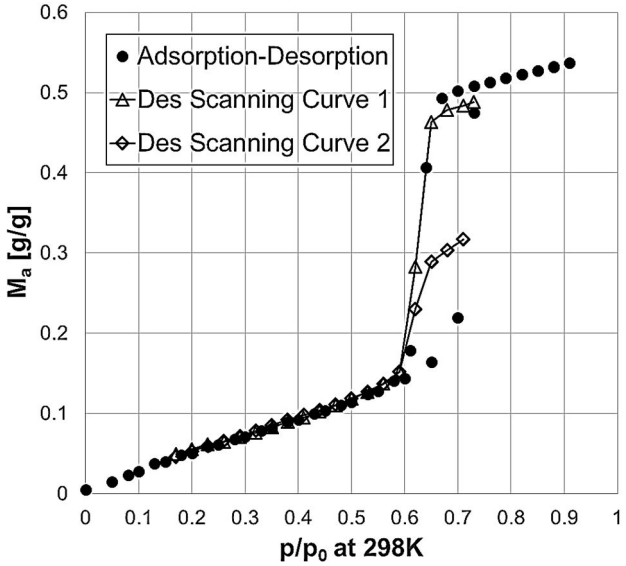

Figure 8.8 – Experimental desorption scanning curves for water vapor on SBA-15 at 298 K. The continuous lines are only a guide for the eyes.

Two adsorption and two desorption scanning curves were measured on the same sample as shown in figs 8.9 and 8.10. The desorption scanning curves seem to be initially in agreement with the theoretical behavior expected for a solid made of perfectly cylindrical independent pores [30], by exhibiting an almost straight crossing behavior from the main adsorption branch up to the main desorption branch. However, the curves start to deviate from a straight-line trajectory when approaching the desorption branch. The adsorption scanning curves show similar and even clearer behavior. Indeed, the curves seem to join the main adsorption branch with a nonlinear and smoother trajectory rather than a crossing straight line. The non-crossing behavior of the scanning curves on SBA-15 has already been observed in the literature [50–52]. The theoretical explanation of such a behavior has been attributed to the possible presence of imperfections and/or constrictions inside the mesopores.

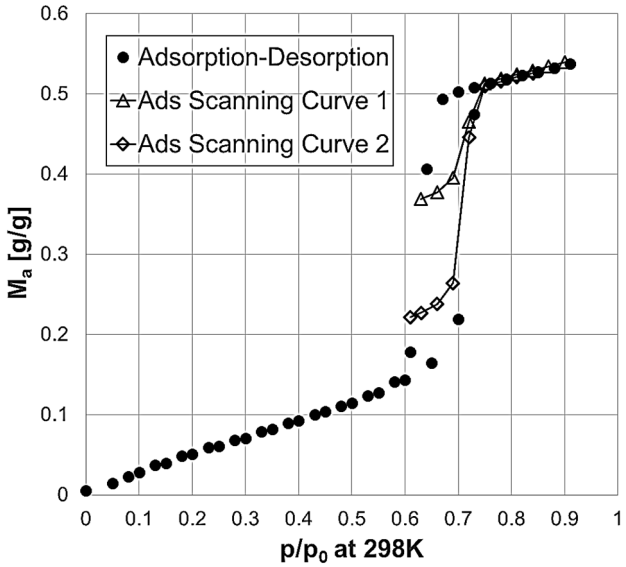

Figure 8.8 – Experimental adsorption scanning curves for water vapor on SBA-15 at 298 K. The continuous lines are only a guide for the eyes.

8.1.3 SBA-15: Conclusions

The structural stability of the silica-based ordered material SBA-15 when exposed to highly concentrated water vapor was investigated. The sample was exposed to several relative humidities up to 90 % at 288 K, 298 K and 308 K. Complete adsorption-desorption cycles were used for the evaluation of the long-term stability of the solid. After the first adsorption-desorption cycle, the equilibrium isotherm is reproducible and the solid appears to be stable to repeated water vapor adsorption-desorption cycles. The structural stability of the solid was confirmed by the measurement of argon adsorption at 87 K. The comparison between the pore size distribution of the fresh sample and the water-used sample showed an unaltered mesoporous volume and a decrease in the microporous volume for the water-used sample.

The first experimental adsorption run with water vapor on a fresh sample resulted in some water trapped inside the microporous structure. The reaction between water and the solid surface occurs during or after the capillary condensation of the water inside the mesopores. This was verified by running a reversible adsorption-desorption experiment up to a concentration value located right before the onset of the capillary condensation in the pores. The equilibrium isotherms are characterized by three main aspects: the relative hydrophobicity of the solid surface which results in a small amount adsorbed at low concentrations; the hysteresis loop due to the capillary condensation phenomenon in the mesopores; the presence of non-crossing scanning adsorption and desorption curves.

8.1.4 Silica-gel: Main adsorption-desorption curves and scanning curves

The silica-gel used in this work is a narrow pored beaded form of amorphous silica impregnated with an inorganic (iron) indicator compound. The beads gradually change color from orange in the dry (activated) condition to pale yellow (almost colorless) when saturated with water. The chemical and physical characteristics of the solid are shown in fig. 8.10 as reported by the manufacturer.

Typical Properties	Moisture content at 145°C	3% maximum
	Equilibrium capacity for water vapour at 25°C and given relative humidity (r.h.)	
	20% r.h.	> 10% w/w (weight for weight)
	35% r.h.	> 15% w/w
	50% r.h.	> 23% w/w
	80% r.h.	> 33% w/w
	Iron content	0.4% w/w
	BET surface area	600 - 800 m^2/g
	Pore volume	0.35 – 0.45 ml/g
	Average pore diameter	20 – 30 A
	pH (10% aqueous solution)	1.8 – 2.2
	Bulk density	700 - 800 g/l
Colour change	Orange	10% w/w adsorption
	Pale Orange	15% w/w adsorption
	Pale Yellow	20% w/w adsorption
Chemical Composition	Silica SiO_2	approx. 98% w/w
	Humidity Indicator	approx. 0.4% w/w
Bead Size	Less than 2 mm	5% maximum
	Greater then 5 mm	5% maximum
Toxicity		Non-toxic

Figure 8.10 – Physical and structural *characterization* of the silica gel sample used in this study. The figure was provided by the manufacturer.

Several adsorption-desorption isotherms of water vapor on silica-gel were measured and used as a reference for the ZLC system. The long-term stability of this solid to repeated water vapor adsorption-desorption cycles is well known in the literature. This has also been confirmed in this study by the perfect reproducibility of the adsorption-desorption isotherms measured several times on the same sample and at different temperatures.

For the measurement of the equilibrium isotherms, 3 beads with a total dry mass of 48mg were used. In fig. 8.11, the experimental water vapor adsorption-desorption isotherms are reported at 318K on a fresh sample and on the same used sample. Similarly, to SBA-15, the first run shows a small hysteresis loop at low concentration. This can also be attributed to some water

which strongly reacts with the solid surface. In fig. 8.12 the experimental equilibrium isotherms of water vapor on silica-gel measured at different temperatures are reported. The small difference between the isotherms, measured at different temperatures and plotted on the same scale, indicates that the isosteric heat of adsorption is quite close to the heat of condensation of water as it can simply be demonstrated using the Clausius-Clapeyron equation.

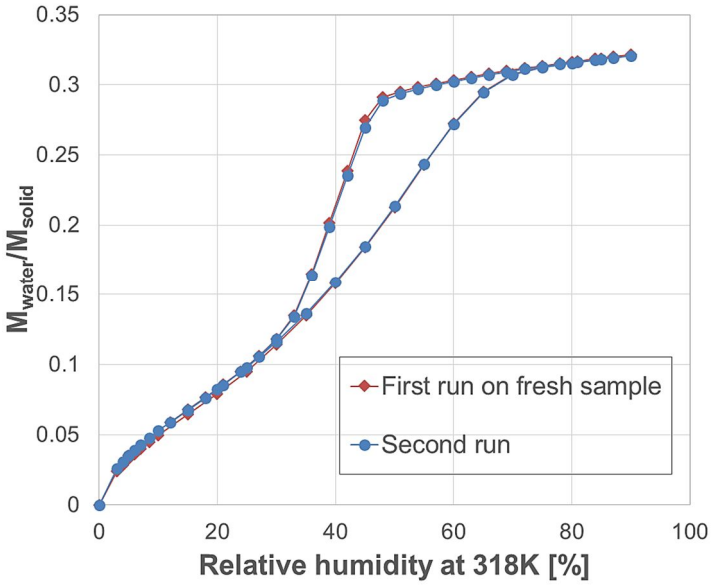

Figure 8.11 – Experimental adsorption-desorption equilibrium isotherm for water vapor on silica gel at 318K. Sample mass 48 mg. The continuous lines are only a guide for the eyes.

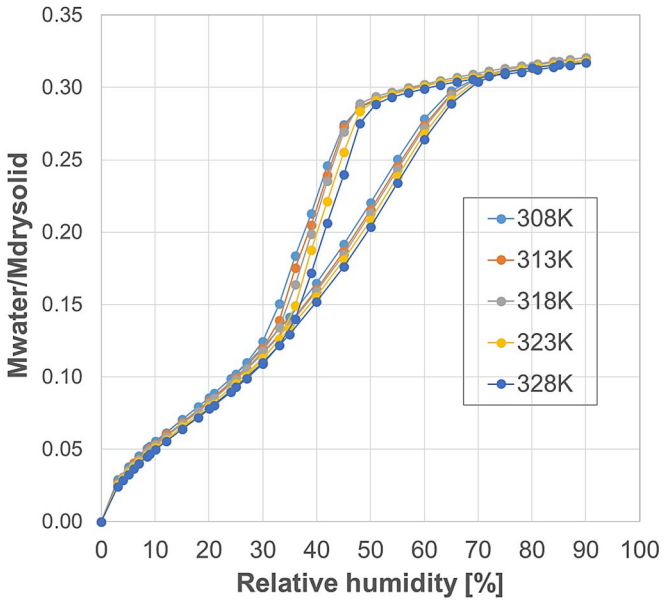

Figure 8.12 – Experimental adsorption-desorption equilibrium isotherms for water *vapor* on silica gel at different temperatures. The continuous lines are only a guide for the eyes.

In fig. 8.13 the equilibrium adsorption-desorption isotherm measured at 313K together with the adsorption and desorption scanning curves are reported. As expected, the scanning curves show a converging behavior. This means that the curves depart from one of the isotherm

branches and join the opposite branch either at the lower or at the higher closing point of the hysteresis.

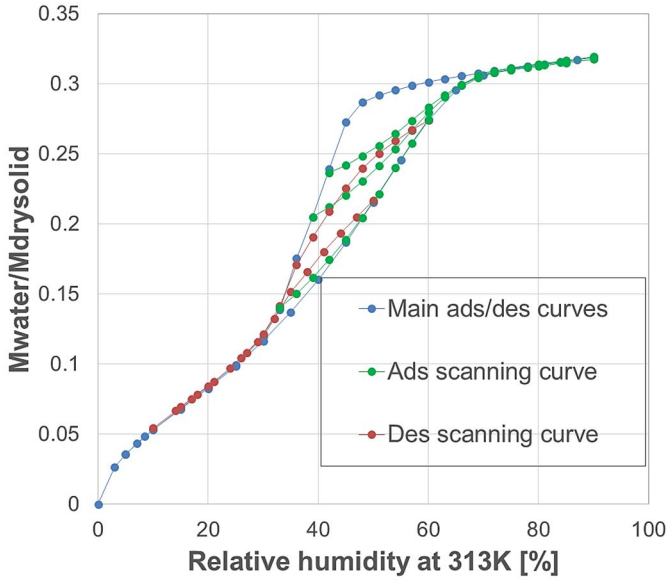

Figure 8.13 – Experimental adsorption-desorption equilibrium isotherms and adsorption-desorption scanning curves for water vapor on silica gel at 313K. The continuous lines are only a guide for the eyes.

8.2 ZLC system

8.2.1 Introduction

In this work and for the first time in literature the Zero Length Column (ZLC) technique was used to measure the adsorption-desorption isotherm and scanning curve of a condensable vapor on mesoporous adsorbents up to a gas phase relative saturation of 90% at 298K. The technique showed two extraordinary and innovative advantages when compared to a traditional gravimetric system: a) The possibility to obtain continuous adsorption and desorption branches for complexly shaped isotherms; b) The small amount of time needed to measure a complete adsorption-desorption cycle. Water vapor and two silica-based material, SBA-15 and silica-gel, were respectively used as adsorptive and adsorbent materials. The adsorption and desorption branches of the isotherm were calculated with a robust and reasonably simple integration of the mass balance in the system. The adsorption-desorption isotherms obtained with the ZLC system were compared and validated against the equilibrium water vapor adsorption-desorption isotherms measured on the same solids on an independent commercial gravimetric system designed for water vapor adsorption. A systematic analysis of the dynamic response of the experimental system was carried out to evaluate the influence of the sample

mass on the calculated isotherm. A corrective deconvolution procedure is suggested and applied when using low sample masses or kinetic control conditions.

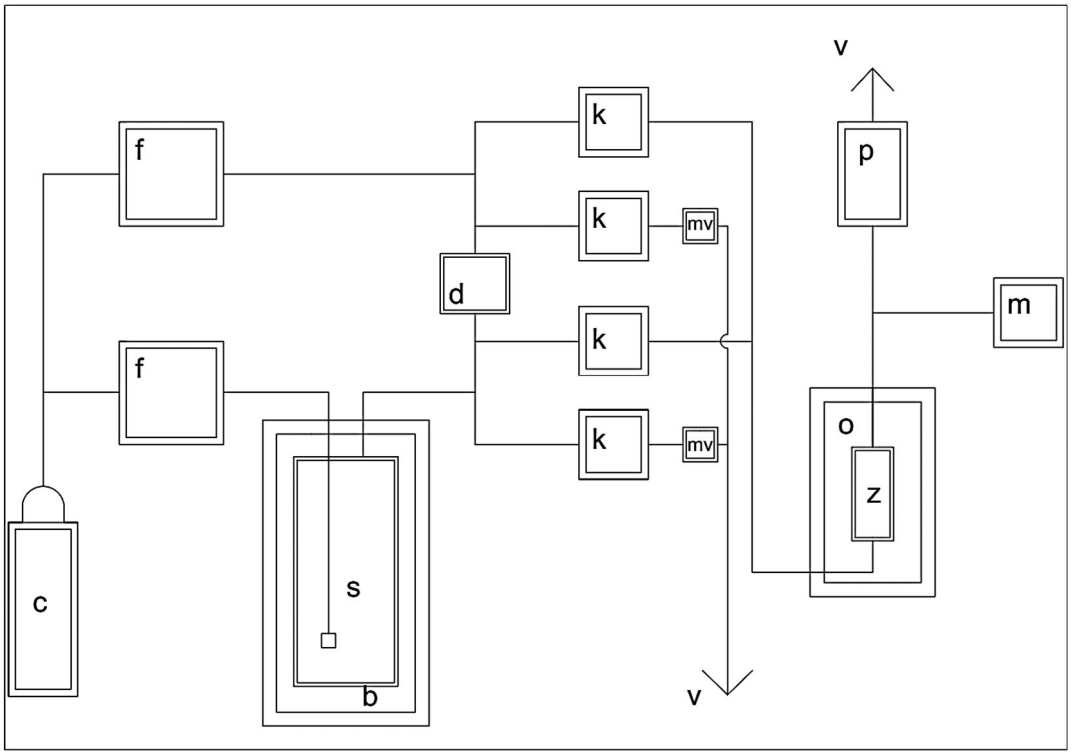

Figure 8.14 – Schematic flowsheet and components of the experimental ZLC system. c gas cylinder. f mass flow controllers. b water bath. s bubbler. k solenoid switching valve. v vent. o ZLC oven. z ZLC. p humidity probe. m mass spectrometer.

The experimental apparatus used in this work is a home-made ZLC system. The simplified flowsheet of the system is presented in fig. 8.14. For the humidification of the feed line, a bubbler was used.

8.2.2 SBA-15: Main adsorption and desorption curves

The initial experiments were aimed to find out the optimal values of the experimental parameters for the assessment of the control regime of the system. Several experiments at the same temperature and same initial concentration were performed at different flowrate to find out the minimum equilibrium flowrate. As discussed in chapter 5, a plot of the experimental C vs Ft represents a simple and strong graphical check for the assessment of the control regime of the system. This represents an immediate and straightforward check. An alternative and more accurate graphical check is given by the integration of the experimental signal according to Eq. (8.2). In such a case the equilibrium isotherms or kinetic isotherms (see fig. 10.3), measured at the different flowrates, are calculated and compared on a $\bar{q}$ vs c plot. With this alternative graphical check, the experimental validation of equilibrium control is given by the

overlapping of the different isotherms. The advantage of this new graphical check is due to the simultaneous verification of the control regime and of the consistency of the mass balance. This results particularly handy in case of non-overlapping curves, i.e. kinetic control conditions. Indeed, the initial amount adsorbed is given by the total area underneath the C vs Ft curve and this value must be independent on the flowrate and on the control regime.

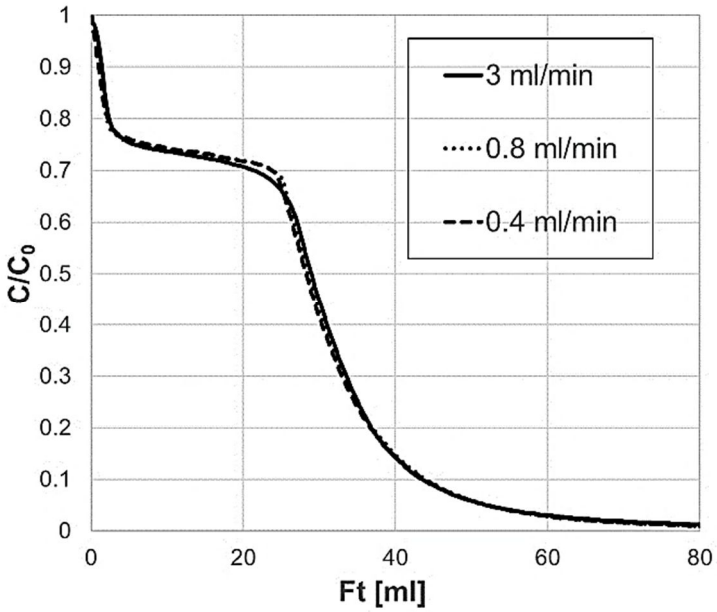

Figure 8.15 – Experimental Ft-plot for the evaluation of the control regime on SBA-15. Sample mass 3.7 mg.

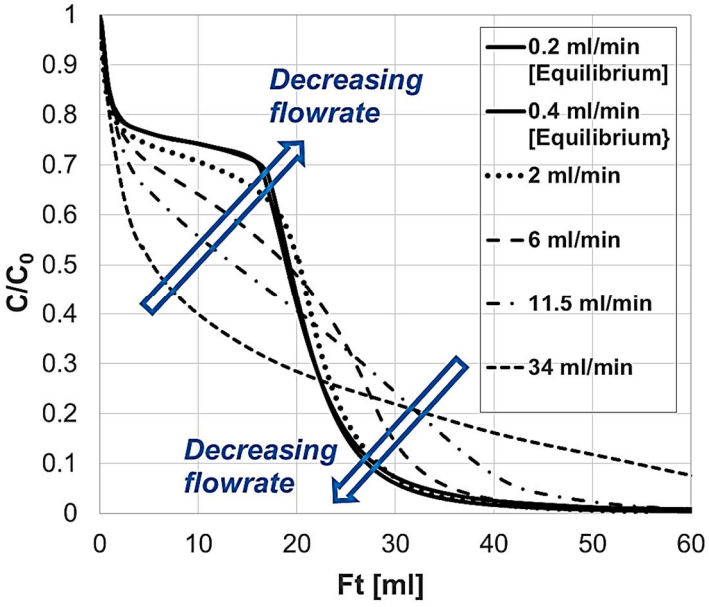

Figure 8.16 – Experimental Ft-plot for the evaluation of the control regime on SBA-15. Sample mass 1.2 mg.

The equilibrium control conditions can clearly be observed in fig. 8.15 where three desorption curves at three different flowrates are plotted on an Ft-plot. The curves overlap at the two lowest flowrates demonstrating the equilibrium control condition. The curve at 3 ml/min shows

some deviation from the other curves and therefore it can be considered as the onset of a transition state between equilibrium and kinetic control. It is also interesting to notice how extremely low flowrates are needed to reach the equilibrium control condition. This aspect indicates a quite slow transport mechanism of water inside the solid. In comparison, in fig. 8.16 it is possible to observe a more evident transition when using higher flowrates. The two figures refer to different sample masses as it is possible to observe from the total area underneath the curves. In fig. 8.16, a smaller mass of solid was used to increase the L parameter. This results more convenient for kinetics studies as the system approaches kinetic control conditions at lower flowrates. Whereas, for equilibrium studies, a larger amount of solid is preferred. A larger mass of sample could result rather convenient in the case of very slow transport kinetics.

8.2.3 SBA-15: Calculation of the isotherm branches

As discussed in the theory section in chapter 6, the shape of the isotherm can already be spotted from the experimental concentration curves. Eq. (8.1), expressed in section 6.2.4, can be rearranged for the integration respect to time and for the calculation of the average amount adsorbed at a given gas phase concentration. Considering the desorption process in which a pure inert gas is used, the integration of the mass balance can be expressed as:

$$\bar{q}_{des}(t) = \frac{c_0 \int_0^{\infty} F_{out}(t) C_{norm}(t) dt - c_0 \int_0^{t} F_{out}(t) C_{norm}(t) dt - c_0 V_f C_{norm}(t)}{m_{solid}} \tag{8.2}$$

Where $C_{norm}(t)$ is the normalized experimental signal acquired by the MS at the outlet of the column. $F_{out}(t)$ is the flowrate at the outlet of the column. This flowrate is not considered constant and this is discussed later. c_0 is the absolute initial concentration of water measured by the humidity probe. V_f is the volume of the gas phase inside the column and it is determined with a blank experiment. m_{solid} is the dry mass of the solid packed in the column. The integral can be split in two parts. This allows to avoid the systematic error associated with the integration of the noisy part of the signal close to the baseline. At low concentrations, any isotherm will eventually be linear and the experimental signal can be fitted with an exponential decay [86]. The integration of the mass balance can therefore be rearranged as follows:

$$\bar{q}_{des}(t) = \frac{\begin{array}{c} c_0 \int_0^{timeEXP} F_{out}(t) C_{norm}(t) dt - c_0 \int_0^{t} F_{out}(t) C_{norm}(t) dt - V_f C_{norm}(t) \\ + c_0 \int_{timeEXP}^{\infty} F_{out}(t) C_{expout}(t) dt \end{array}}{m_{solid}} \tag{8.3}$$

Where $timeEXP$ is the time at which the exponential integration begins. $C_{expout}(t)$ is the exponential function used to regress the low concentration data. For the adsorption branch which is calculated from the adsorption curve, the mass balance remains the same as formulated in Eq. (8.1), expressed in section 6.2.4, but the expression for the calculation of the amount adsorbed at each concentration in the gas phase is slightly different. The integration of the mass balance for an adsorption process can be expressed as:

$$\bar{q}_{ads}(t) = \frac{F_{in}(t)c_0 - \int_0^t F_{out}(t)C_{norm}(t)dt - V_f C_{norm}(t)}{m_{solid}} \tag{8.4}$$

For the calculation of the integrals, it must be considered that the flowrate at the outlet of the column is generally not constant and it can be assumed constant only under diluted conditions. In the literature, many different approaches have been used for the approximation of the outlet flowrate. The simplest approximation for the outlet flowrate assumes that the inert mass flowrate entering the column is equal to the inert mass flowrate leaving the column. Following this approach, the outlet mass flowrate can be expressed as:

$$F_{out}(t) = \frac{F_{in}(1-y_{in})}{1-y(t)} = \frac{F_{in}(1-y_{in})}{1-C_{norm}(t)y_0} \tag{8.5}$$

Where y_0 is the initial molar fraction of water inside the column and y_{in} is the molar fraction of water in the inlet flowrate. Eq. (8.5) was proved to be a valid approximation of the outlet flowrate up to a water molar fraction of 0.3. The relationship fails to predict the actual flowrate for higher molar fractions [37]. Indeed, Eq. (8.5) is only an approximation of the correct outlet flowrate and it is derived from the mass balance on the carrier gas in which the accumulation term in the column is neglected. In the present study, the maximum molar fraction of water never exceeded a value of 5% and, therefore, Eq. (8.5) was used for the calculation of the experimental adsorption-desorption isotherms. A more extensive analysis on the possible flowrate approximations to adopt for the calculation of the isotherms is reported in section 6.2.5. In the same section, a graphical comparison among the adsorption-desorption isotherms calculated using the different flowrate approximations is reported.

The integration of the normalized experimental concentration curves according to Eq. (8.3) and Eq. (8.4) yields the adsorption-desorption isotherms. The integral is calculated at each point of the experimental signal. Considering the high frequency of data sampling of the detector, the integrated curves can practically be considered as continuous adsorption-desorption isotherms. It is interesting to notice how the experimental signal shown in fig. 8.17 perfectly resembles the simulated data shown in Section 6.2.4.

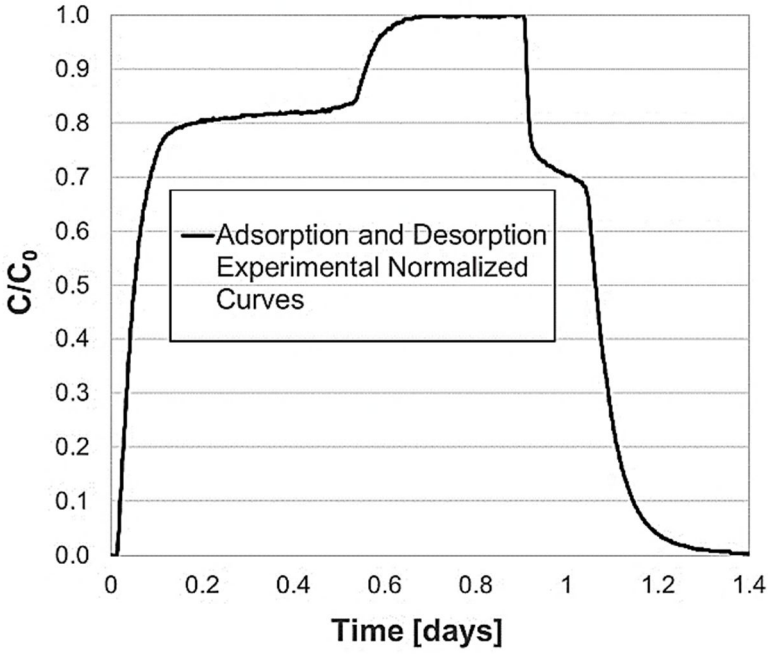

Figure 8.17 – Experimental ZLC adsorption-desorption normalized concentration curves for water vapor on SBA-15 at 298K. Sample mass 1.2 mg.

In fig. 8.18 the integrated adsorption and desorption curves are shown and validated against the gravimetric system used as a reference. In both systems, the isotherms were measured on samples which had already been exposed to several water vapor adsorption-desorption cycles as discussed in section 8.1.1. This indicates that only the reversible amount adsorbed is considered in the isotherm. The excellent agreement of the calculated adsorption isotherms between the two independent techniques is quite evident in fig 8.18.

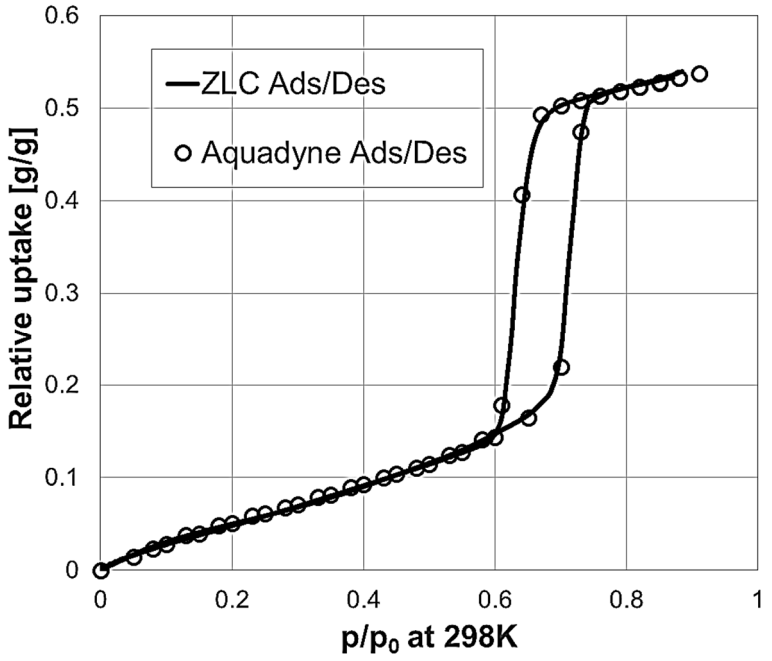

Figure 8.18 – Calculated adsorption-desorption isotherm for water vapor on SBA-15. The experimental data were obtained from the ZLC and the gravimetric system at 298K.

8.2.4 SBA-15: Advantages of the ZLC

What is probably not immediately clear from fig. 8.17 and fig. 8.18 are the exceptional advantages in using the ZLC method. It is relevant to stress the possibility to have a continuous equilibrium isotherm in all the range of concentration. This aspect is particularly useful when the isotherm is characterized by almost vertical branches. In this case, the traditional discontinuous gravimetric or volumetric techniques would require a high number of single point measurements to show the accurate shape of the isotherm. Moreover, the equilibration time or the amount of gas dosed for each single concentration step cannot be accurately decided a priori and some trial run is needed to adjust the experimental parameters. In comparison, the ZLC system can, in theory, provide the equilibrium isotherm from the first experimental run if the flowrate is sufficiently low to ensure the equilibrium control conditions.

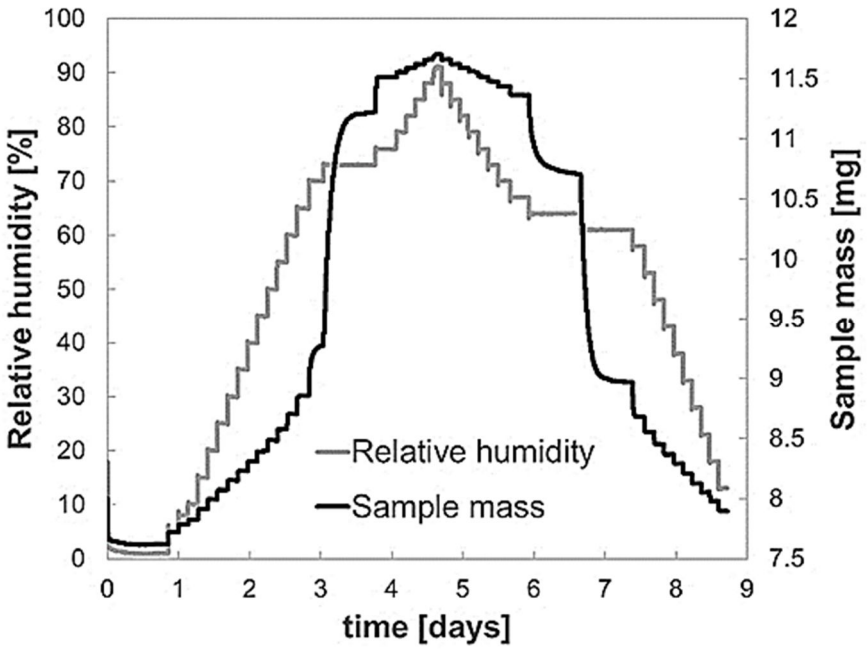

Figure 8.19 – Experimental uptake curves and relative humidity for water vapor on SBA-15 at 298K. Sample dry mass 7.6 mg.

The ZLC is a continuous chromatographic technique and it results intrinsically faster than the repeated single point techniques. This can be confirmed from fig. 8.19 where the experimental uptake curves of the gravimetric system are reported together with the stepwise changes in the gas phase concentration. The ZLC system was able to measure the complete adsorption-desorption isotherm in less than 36 hours while the gravimetric system needed almost nine days. It must be clarified that 1.2 mg of solid was packed in the ZLC while 7 mg of solid was used in the gravimetric system. The experiment duration is linearly affected by the mass of sample loaded in the ZLC. The gravimetric system is not supposed to be affected by the mass

of the sample if external transport limitations, heat effects or bed transport effects are excluded. The high time consumption of the gravimetric technique is mostly due to its discontinuous way of operating.

8.2.5 SBA-15: Adsorption and desorption scanning curves

The advantages of the ZLC extend to the measurement of the scanning curves, i.e. the curves which scan the hysteresis loop from the adsorption branch to the desorption branch and *vice versa*. These curves are divided into adsorption and desorption scanning curves according to the starting point and direction along the equilibrium isotherm. To obtain the desorption scanning curves on the ZLC system, two methods can be used. The solid can firstly be saturated with a concentration of water belonging to any point of the almost vertical adsorption branch; Then the feed is switched to pure inert under equilibrium control. This method is comparable to the operating way of a discontinuous technique. However, this method is not recommended since it needs an extremely stable value of gas phase concentration in the feed stream especially for isotherms with stepwise capillary condensation branch. With the second method, the advantages of the ZLC is fully exploited. The adsorption is performed under equilibrium control up to any point on the almost horizontal part of the concentration signal and then the feed is switched to pure inert under equilibrium control. The experimental concentration signal corresponding to one of the measured desorption scanning using the recommended method is shown in fig. 8.20. The calculated desorption scanning curves are shown in fig. 8.21.

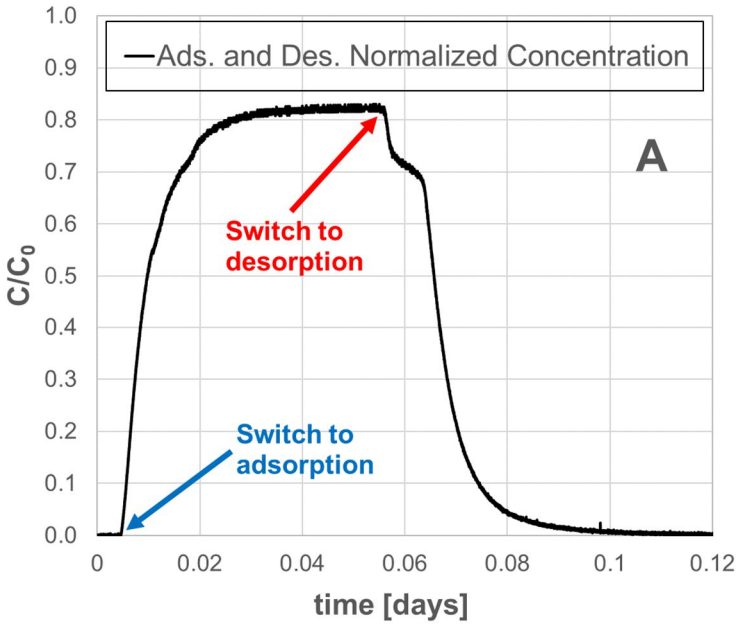

Figure 8.20 – Experimental ZLC normalized concentration curve obtained from the measurement of a desorption scanning curve for water vapor on SBA-15 at 298K.

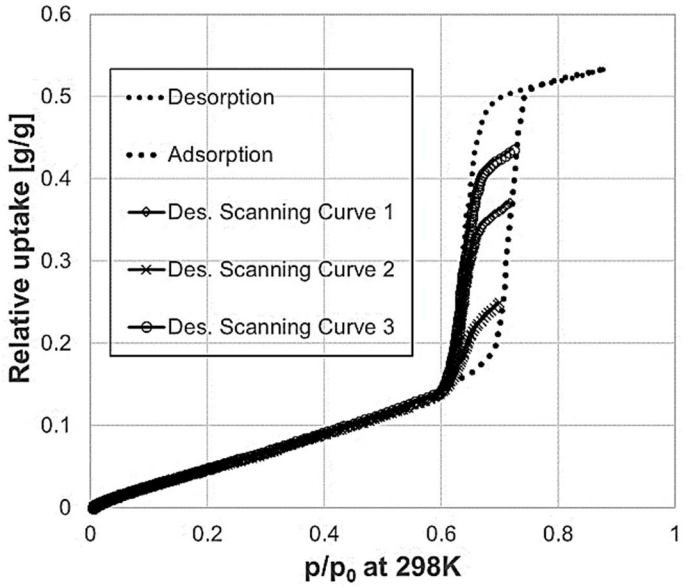

Figure 8.21 – Calculated desorption scanning curves for water vapor on SBA-15 at 298K. The scanning curve was calculated using the signal in fig. 8.20.

The adsorption scanning curves can be obtained by saturating the sample with a gas concentration beyond the upper closure point of the hysteresis loop. Then the flow is switched to pure inert and the desorption is performed under equilibrium control up to any point on the almost horizontal part of the concentration signal which corresponds to the almost vertical part of the desorption branch. The flow is again switched to the humid feed gas under equilibrium control conditions and the adsorption scanning curve is obtained. The experimental adsorption concentration signal corresponding to one of the measured adsorption scanning curves is shown in fig. 8.22. The calculated adsorption scanning curve is shown in fig. 8.23.

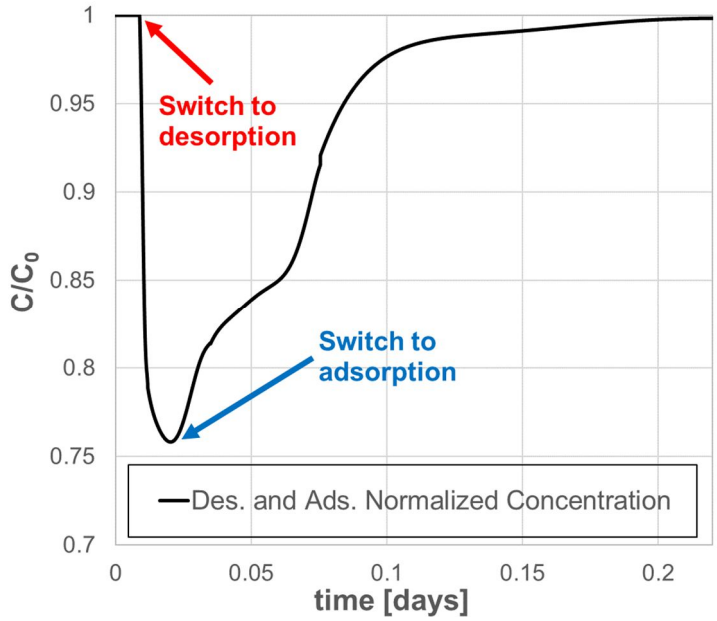

Figure 8.22 – Experimental ZLC normalized concentration curve obtained from the measurement of an adsorption scanning curve for water vapor on SBA-15 at 298K.

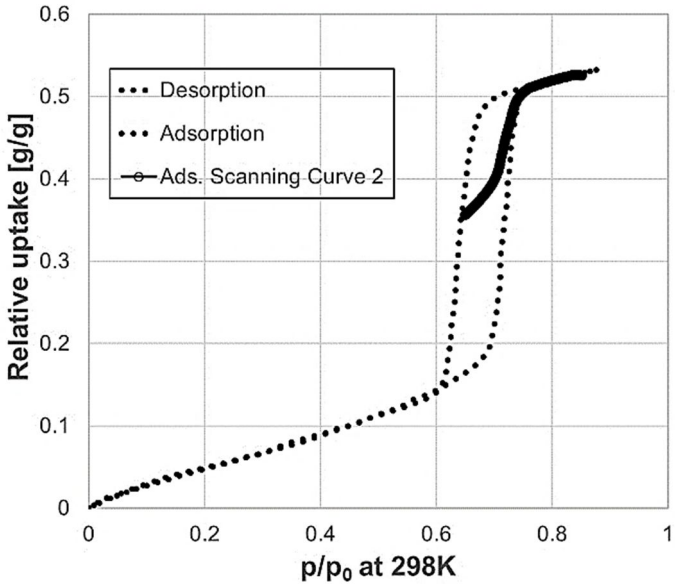

Figure 8.23 – Calculated adsorption scanning curve for water vapor on SBA-15 at 298K. The scanning curve was calculated using the signal in fig. 8.22.

The scanning curves have recently gained a lot of interest as a powerful instrument for the understanding of the inner structure of the solid [44]. The scanning curves are usually classified based on their trajectory. The curves are defined respectively as converging if they converge to the upper or lower closure point of the hysteresis loop, crossing if they join the main adsorption or desorption branch before the closure points, returning if they return to the branch from which they departed [48]. The trajectory of this curve is strictly correlated to the internal structure of the solid [44]. Therefore, the possibility to obtain continuous scanning curves might represent a significant advantage for the structural characterization of porous solids. The shape of the scanning curves measured with the ZLC system agrees with the scanning curves measured on the gravimetric system as shown in figs 8.8-8.9.

8.2.6 SBA-15: Deconvolution of the experimental signal

The possibility to use a tiny amount of solid is not only convenient for the limitation of heat effects and pressure drops, but it also permits to reduce the duration of the experiments. To further decrease the duration time of the experiments, one might think to reduce the amount of solid packed inside the column. However, it is necessary to consider two aspects: Firstly, the absolute integral of the experimental signal will be smaller and the relative error in the calculation of the integral might be higher; Secondly, the effect of the geometry of the system and the dynamic response of the system might become more relevant.

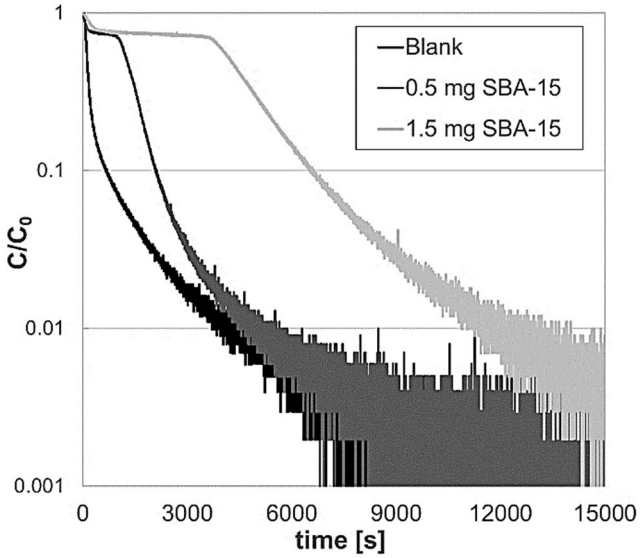

Figure 8.24 – Experimental ZLC normalized desorption curves for different masses of sample and for the blank experiment (empty column).

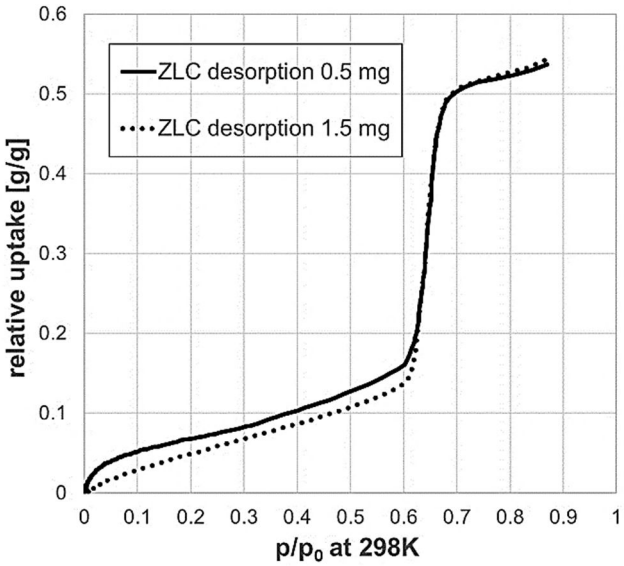

Figure 8.25 – Calculated desorption isotherms from experiments performed using different masses of sample (fig. 8.24).

The calculated desorption isotherm, obtained with only 0.5 mg of sample packed inside the column, is reported in fig. 8.25. Compared to the isotherm obtained with 1.5 mg of sample, it is possible to notice a higher amount adsorbed from low pressure up to a value of $p/p_0 = 0.6$. It is also relevant to notice the unexpected curvature at very low concentrations, which might give the impression of a much higher Henry law constant when compared to the experiments conducted with 1.5 mg of sample. The comparison among the experimental concentration signals using different sample masses is shown in fig. 8.24. The 0.5 mg signal is strongly influenced by the blank response of the system. The overlap of the two signals before joining the baseline is theoretically impossible according to the mass balance in the system. This

scenario can be possible only if some water is retained in the system and if the residence time is comparable to the residence time of water in the solid adsorbent. In such a case the correct shape of the isotherm can still be calculated if a complete analysis of the blank response of the system is performed.

The response of the system depends on the geometric characteristics of the fittings and components which are placed in between the two switching valves and the detector. To correctly interpret the response of the blank system, it is necessary to consider the dynamic response of each of the components of the system.

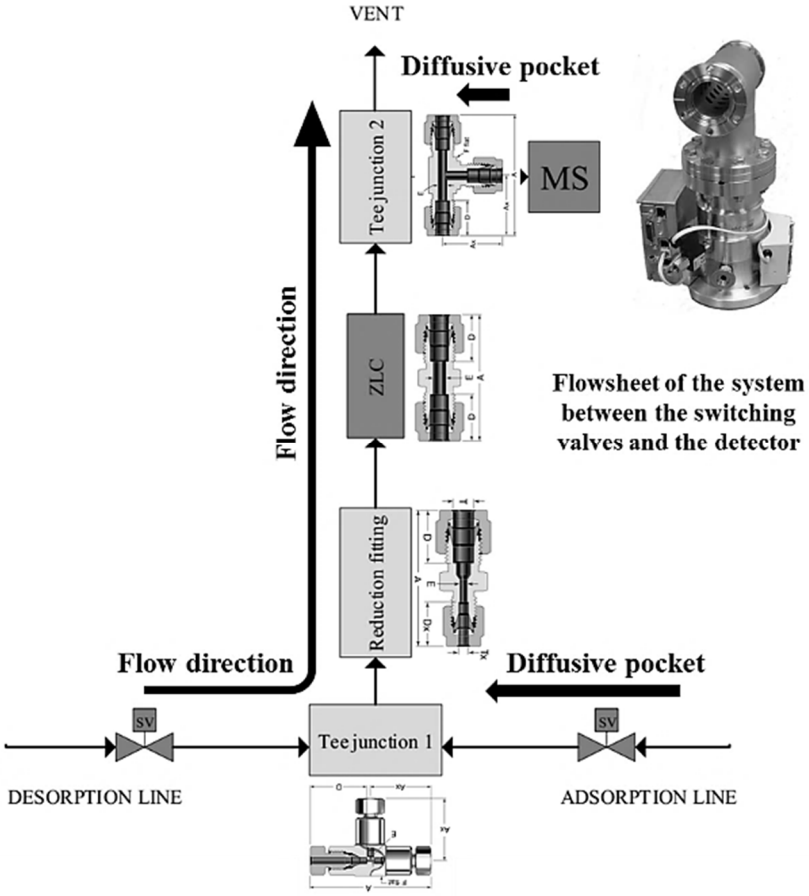

Figure 8.26 – Schematic flowsheet of the experimental system after the two switching valves (see fig. 6.3).

In fig. 8.26 it is reported the flowsheet of the experimental system with all the components and fittings involved in the analysis. The response of the system is examined under desorption conditions. This implies a stepwise change of concentration to pure inert at the inlet of the system at time zero when simultaneously the adsorption valve closes, and the desorption valve opens. The inlet of the system corresponds to the outlet of the desorption valve according to the flow direction arrow in fig. 8.26. All the straight unions were considered as pure mixing volumes while the T-junctions were considered as pure mixing volumes with a side diffusive pocket for the part in stagnant flow. Considering the internal geometry of the mass

spectrometer, the detector was modeled as a mixing volume plus a diffusive side pocket as already done in the literature [41]. The parameters of the models are given by the mixing volumes and diffusion lengths of the components. The values of the geometrical parameters are either given on the catalog of the fittings manufacturer or they are calculated from the geometrical characteristic of the system. The parameters of the detector cannot be calculated in advance and they can be used for the regression of the blank response. The tube in between two consecutive components was considered as a pure time-lag and this does not have any influence on the shape of the response curve. In fig. 8.27 it is shown the predicted response of all the components and the experimental response at the detector.

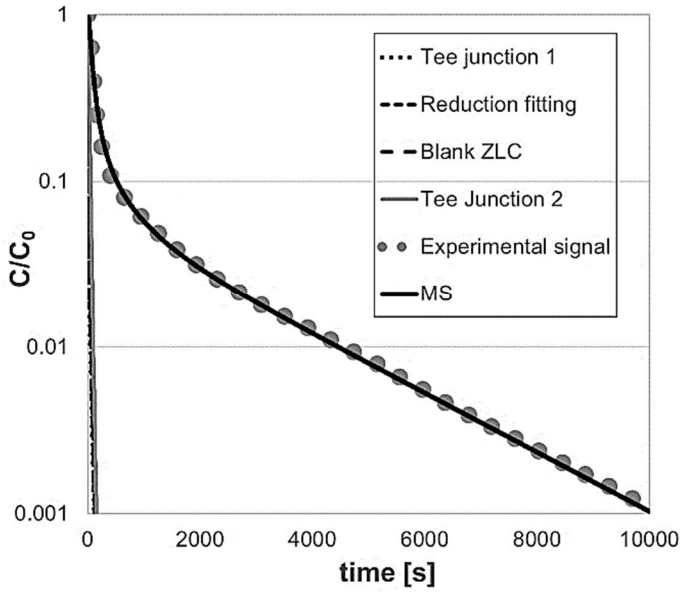

Figure 8.27 – Simulated blank response of all the components represented in fig. 8.26 and experimental blank response measured by the mass spectrometer.

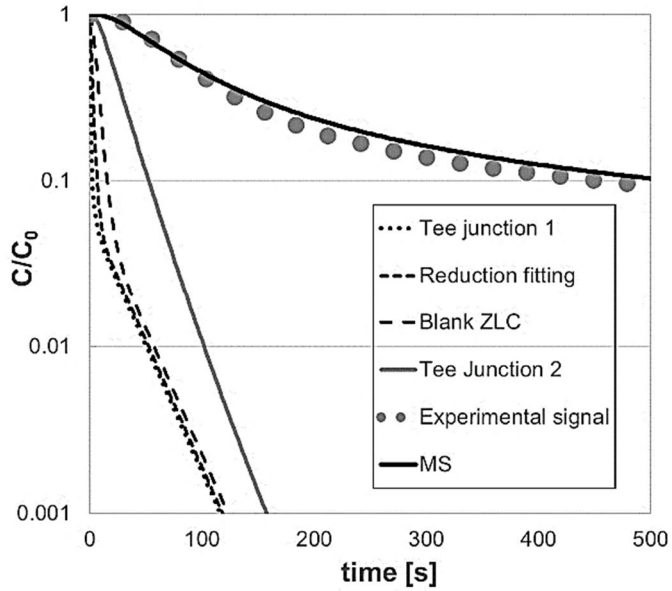

Figure 8.27 – Magnification of fig. 8.27 at lower times.

It is clear from figs 8.27-8.28 that the blank response is fundamentally due to the dynamic response of the detector. The response of all the other components is essentially stepwise. The concentration at the inlet of the detector (T-junction 2) can be considered as the concentration at the outlet of the ZLC. The concentration measured by the detector can be expressed using the convolution integral as:

$$C_{detector}(t) = \int_0^t G_{detector}(t-u)\, C_{in}(u)du \tag{8.6}$$

Where $G_{detector}$ is the transfer function of the detector in the time domain and C_{in} is the concentration change at the inlet of the detector, i.e. the forcing function. The convolution integral can be approximated numerically and the concentration at the inlet can be calculated at each time interval as described in section 6.2.6. The parameters of the detector, calculated using the blank response, are to be adopted to perform the deconvolution of the detector signal to obtain the concentration at the inlet. The de-convoluted concentration can therefore be used to perform the integration of the mass balance and the calculation of the equilibrium isotherm according to Eq. (8.3).

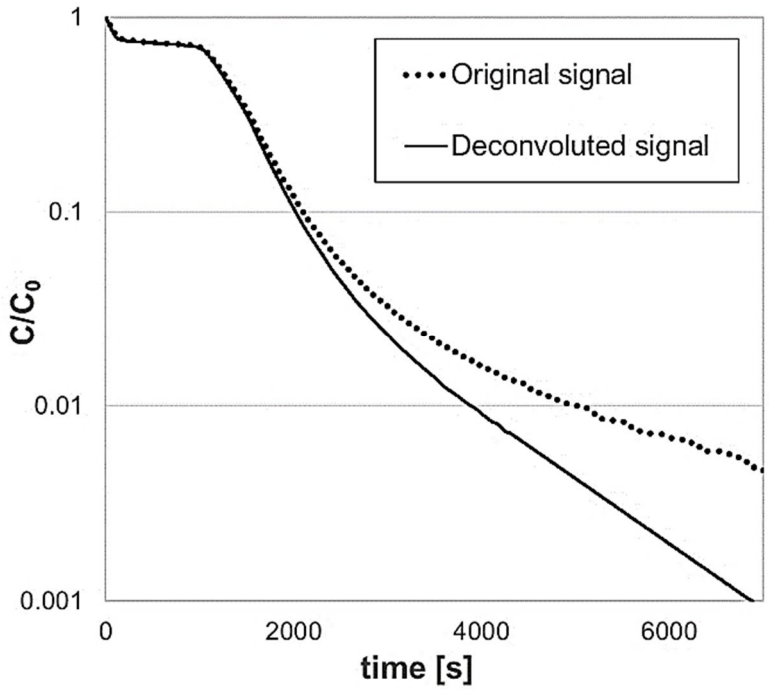

Figure 8.29 – Original and de-convoluted normalized concentration signal.

The deconvoluted signal and the computed isotherm are respectively shown in fig. 8.29 and fig. 8.30. The mathematical modeling, the analysis of the blank response and the deconvolution of the experimental signal were carried out in the Laplace domain and the full mathematical derivation is reported in section 6.2.6.

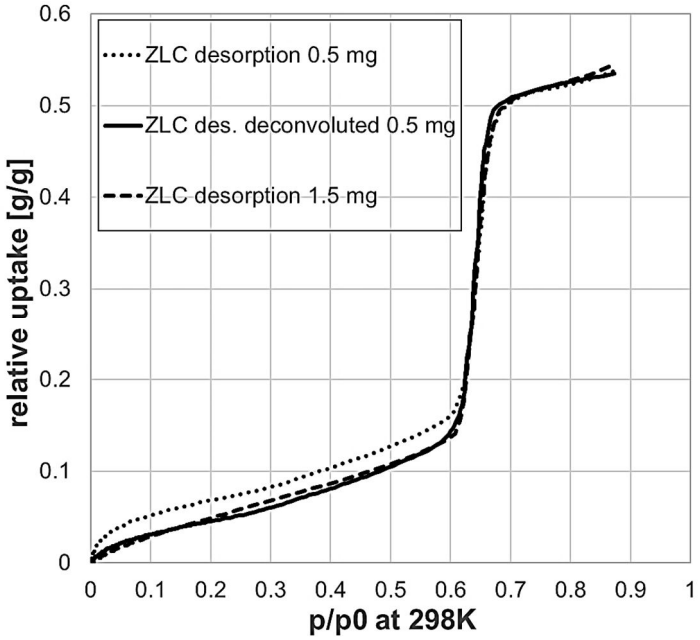

Figure 8.30 – Calculated isotherms for water vapor on SBA-14 using the original and the de-convoluted concentration signal.

The deconvolution approach is a useful correction method to adopt when the residence time of the adsorptive in the ZLC is comparable to the residence time in the detector. The difference between the original and the deconvoluted signal is more evident at low concentrations where a significant different slope of the long-time asymptote can be observed. The correction can be applied to equilibrium experiments for the correct evaluation of the equilibrium isotherm or to kinetic experiments for the correct evaluation of the diffusive time constant. The correction can be avoided if a higher amount of sample is used. A higher mass of sample is useful for equilibrium measurement as the L parameter decreases and the system approach equilibrium conditions at higher flowrates. However, at the same time, a higher mass is likely to increases the experiment duration. The kinetic control condition is better approached by using a lower mass and probably the signal correction is more needed if the correct long-time asymptote is to be determined. The dimensions and the parameters used for the dynamic analysis of the blank response and deconvolution of the detector signal are reported in table 8.1. A detailed description of the parameters is given in section 6.2.6.

Table 8.1 – Experimental and regressing parameters used for the blank response analysis and signal deconvolution.

F	V_{mix}	V_{diff}	X	a	$L_{fitting}$	$\gamma_{fitting}$	$\alpha_{fitting}$
$\left(\frac{ml}{min}\right)$	(ml)	(ml)	(cm)	(s^{-1})	(s^{-1})		

Tee-junction 1	0.4	$1.5 * 10^{-4}$	0.013	5	-	0.502	0.011	0.015
Reducing fitting	0.4	0.012	-	-	0.527	-	-	-
Blank ZLC	0.4	0.029	-	-	0.225	-	-	-
Tee-junction 2	0.4	0.079	0.035	0.85	-	0.184	2.27	0.511
Detector (MS)	-	-	-	-	-	0.0046	0.25	$4.4 * 10^{-5}$

8.2.7 Silica-gel: Main adsorption and desorption curves

In analogy with the experimental procedure used for SBA-15, the first experiments were focused on the evaluation of the control regime of the system and calculation of the adsorption-desorption equilibrium isotherm. The ZLC column was packed with 2.6 mg of silica gel beads with an average size of 0.165mm. In fig. 8.31 the normalized experimental signal for an equilibrium adsorption-desorption cycle is reported. From a comparison with the SBA-15 signal shown in fig. 8.17, it is possible to spot in advance the differences in the shape between the two signals which reflects in a different shape of the equilibrium isotherms. The most visible difference is the absence of the two almost horizontal parts which were observed beforehand for the SBA-15 isotherm. This represents an indication of the fact that the condensation and the evaporation branches of silica-gel are smoother than the ones observed on SBA-15.

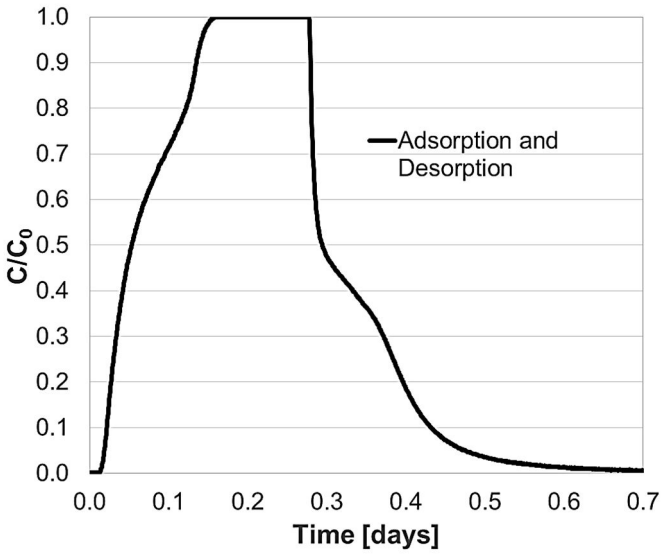

Figure 8.31 – Experimental ZLC adsorption-desorption normalized concentration curves for water vapor on silica gel at 298K. Sample mass 2.6 mg.

In fig. 8.32, the Ft plot for the silica-gel desorption experiments conducted at different flowrates is reported. It can immediately be spotted that the water desorption kinetics on silica-gel is faster than the desorption kinetics on SBA-15 as the equilibrium control conditions are approached at higher desorption flowrates for silica-gel. This concept is better explained and investigated in chapter 8, where the adsorption and desorption kinetics of water vapour on SBA-15 and the desorption kinetics of water vapour on silica gel is studied.

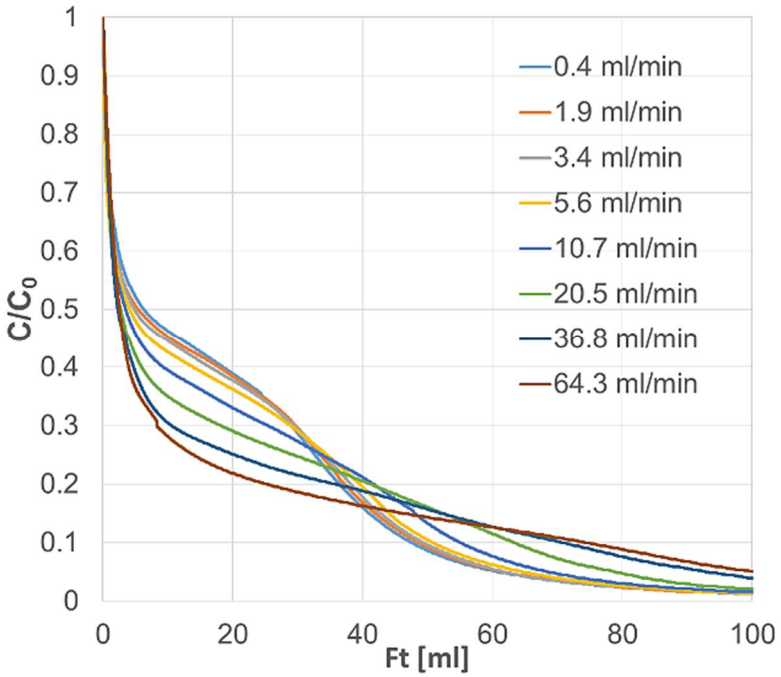

Figure 8.32 – Experimental Ft-plot for the evaluation of the control regime on silica gel. Sample mass 2.6 mg.

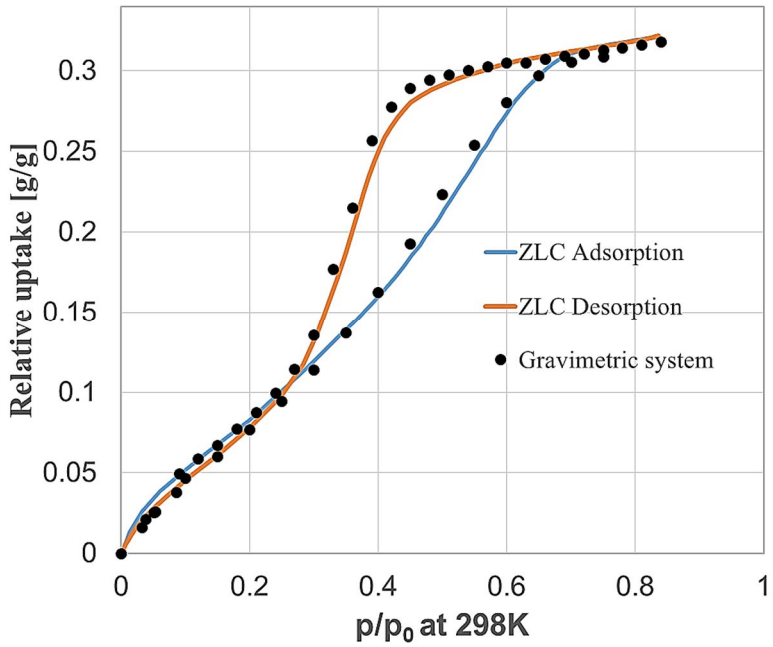

Figure 8.33 – Calculated adsorption-desorption isotherm for water vapor on silica gel. The experimental data were obtained from the ZLC and the gravimetric system at 298K.

For an experiment conducted under equilibrium control conditions, the integration of the experimental adsorption-desorption signal according to Eq. (8.4) for the adsorption and Eq. (8.3) for the desorption, provides the adsorption-desorption isotherm shown in fig. 8.33. In the same figure, the experimental data obtained on the gravimetric system is reported and used as a reference for the ZLC isotherms. As well as for the SBA-15 isotherm, it was possible to measure a continuous adsorption-desorption isotherm in one-tenth of the time taken by the traditional gravimetric system (Figure 8.34).

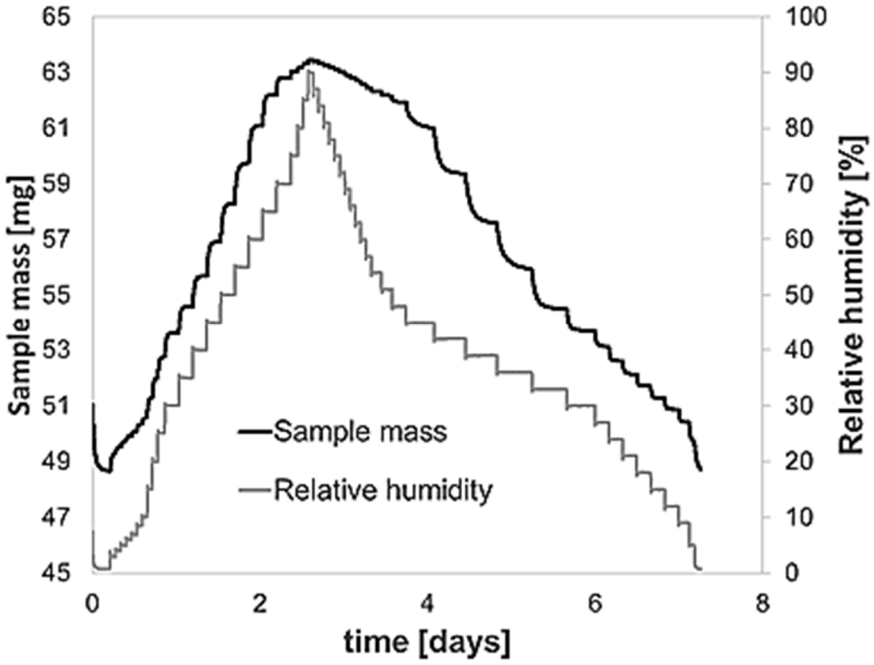

Figure 8.34 – Experimental uptake curves and relative humidity for water vapor on silica gel at 298K. Sample dry mass 48 mg.

8.3 Conclusions

In the present work and for the first time in the literature, the ZLC technique was successfully used for the measurement and calculation of type IV/V adsorption isotherms. The technique can accurately catch the complex shape of the water vapor adsorption isotherm on SBA-15 and silica-gel. The adsorption-desorption isotherms calculated from the integration of the experimental adsorption-desorption curves were validated against the equilibrium isotherm measured in a different and independent commercial gravimetric system, which is designed for water adsorption measurements.

The traditional graphical check for the assessment of the equilibrium control conditions of a ZLC system was applied. The excellent match between the ZLC experimental data and the gravimetric data confirms the enormous advantages of the ZLC system. The ZLC is

intrinsically faster up to an order of magnitude in time and it can provide a practically continuous adsorption-desorption isotherm. This aspect results much advantageous for isotherms characterized by almost vertical branches. It is also possible to measure accurate and continuous adsorption and desorption scanning curves.

The amount of solid loaded inside the column can affect the quality and the reliability of the experimental signal. A sample mass of 1.5 mg of SBA-15 was proved to be enough for reproducible and reliable measurements. A sample mass of 0.5 mg was tested with the aim to further reduce the experiment duration. However, the shape of the calculated isotherm showed some dissimilarity when compared to the correct shape obtained from the 1.5 mg sample and from the gravimetric isotherm. The misleading shape is due to an overlap between the water desorption signal and the blank response signal of the system. This is theoretically questionable unless some water is retained in some part of the experimental system. A systematic analysis of the dynamic response of the blank system revealed that some water is retained for a relatively long time in the detector. This can lead to a misleading shape of the concentration signal if the residence time of water in the detector is comparable to the residence time of water in the ZLC. A correction procedure based on a numerical deconvolution method is proposed and applied for the correct evaluation of the experimental concentration signal. The correction can be used for the correct calculation of the adsorption isotherm or for the evaluation of the correct diffusive time constant in kinetic experiments.

9 Kinetic models

9.1 Introduction

Water vapor adsorption in microporous and mesoporous solids has been studied extensively in the literature due to the many industrial applications in which water vapor adsorption is requested. The industrial applications related to water vapor adsorption are numerous and these include gas drying [4], food and drugs preservation, construction materials conservation, adsorption refrigeration cycles [5] and more recently characterization of porous materials [6,7]. For all of these industrial and commercial applications, the knowledge of the equilibrium and kinetic properties related to water vapor adsorption is critical for the correct modeling of the process. In particular, the understanding of the mass transport kinetics is essential for the modeling and the optimization of dynamic processes involving repeated adsorption-desorption cycles. The modeling of the mass transport kinetics of condensable water vapor in porous solid has been studied extensively on both hydrophilic and hydrophobic solid adsorbents [87]. Hydrodynamic models, percolations models, diffusion models, linear driving force models and empirical expressions have been adopted to describe the uptake kinetics of water and to best-predict the experimental data.

Ribeiro et al. [88] studied the water vapor adsorption kinetics on several solids using breakthrough experiments. The mass transport was modeled using an equivalent linear driving force model and the mass transfer coefficient was correlated to the amount adsorbed using the inverse of the equilibrium isotherm. Glover et al. [89] used a concentration-swing frequency response method to measure water adsorption kinetics at different concentrations on several solids. They found out that the mass transfer coefficient strongly depends on the concentration adsorbed and it exhibits a relevant minimum for concentration values located in the hysteresis region of the equilibrium isotherm. The Darken correction factor was claimed to well predict the experimental diffusion coefficient at the different concentrations only for some of the solids tested. However, the authors admitted the necessity of knowing the slope of the scanning curves for the correct evaluation of the Darken correction factor in the hysteresis region when a concentration-swing frequency response method is used. Jaguste et al. [90] developed a diffusive-hydrodynamic model to describe the combined surface diffusion and viscous flow of coexisting multilayer adsorbed and capillary condensed cyclohexane in activated alumina pellets. Although the total pressure is constant along the capillary, the driving force for the

mass transport was considered to be given by the hydrostatic stress pressure in the adsorbate phase. The apparent diffusion coefficient was theoretically correlated to the amount adsorbed using a correlation which is mathematically similar to the Darken correction factor. Rhim et al. [91] considered the transport of a condensed liquid phase inside a capillary where the ends of the capillary are exposed to different pressures. Tamon et al. [92] modeled the mass transport of both multilayers adsorbed phase and capillary condensed phase respectively as a combination of hopping flow and viscous flow. They derived an expression quite similar to the Darken correction factor for the prediction of the apparent surface diffusion coefficient at different adsorbed phase concentrations. Other authors have used hydrodynamic approaches with similar results [93]. Lin et al. [94] modeled the mass transport of water adsorbed inside an activated carbon considering two diffusive mechanisms in parallel. The diffusive flow of the gas phase and the diffusive flow of the adsorbed phase. Local equilibrium was assumed between the two phases along the pore. The combined diffusion equation has an effective diffusion coefficient which depends on the inverse of the derivative of the equilibrium isotherm. Šoóš et al. [95,96] developed a lattice percolation model for the evaluation of the adsorption kinetics of nitrogen on Vycor glass and water on silica-gel. Hefti et al. [63] used an empirical equivalent linear driving force model to predict the dynamics of water vapor adsorption in a column packed with activated carbons. However, more than ten empirical parameters were needed for a good prediction of the experimental breakthrough curves.

Although several different approaches and models have been adopted to understand the mass transport kinetics of a condensable vapor adsorbing in porous solids, all these studies have shown a common characteristic. Due to the large adsorbed phase concentration change when adsorbing a condensable vapor, the mass transfer coefficient is strongly dependent on the amount adsorbed. In many experimental studies [63], the mass transfer coefficient has shown a clear minimum located in the hysteresis region of the equilibrium isotherm. This phenomenon has been theoretically predicted considering different approaches. However, the Darken correction factor is the only thermodynamic consistent method to express the dependence of the transport diffusivity on the equilibrium amount adsorbed. The Darken factor requires a smooth and accurate equilibrium isotherm for the correct evaluation of the slope and the secant, and it can predict a strong decrease of the transport diffusivity in the capillary condensation region.

In all of the works reported in the literature about the adsorption kinetics of water vapor in porous solids, a clear indication of the real transport mechanism for condensing-evaporating water vapor in a wide range of concentrations is still missing. The reasons are mainly due to a

lack of uniformity in the experiments and to the different solid adsorbents used in the different studies. Other factors might be related to the structure and surface chemistry of the solids. The presence of pore networks or strong chemical surface groups can lead to different transport mechanisms and give a strong contribution to the mass transfer kinetics. It is also to be mentioned that heat effects could be relevant in case of large concentration steps and significant amounts adsorbed. Other side effects as axial dispersion and pressure drops are likely to occur when packed columns are used for the study of the adsorption-desorption kinetics. The side effects can eventually be modeled and predicted but their presence might affect and impede the correct evaluation of the mass transfer kinetics.

In this view, the present work represents an attempt to fully understand the kinetics and the transport mechanism of condensable water vapor in regular independent straight pores in the entire range of adsorbed concentration from empty pores up to full saturation. This permitted to avoid eventual pore network contributions. In addition, SBA-15 is rather hydrophobic and the influence of strong surface groups can be excluded. As regards the experimental methodology, the use of the ZLC technique permitted to minimize all the possible side effects and to identify the most probable mass transfer mechanism.

9.2 Equivalent linear driving force model

As discussed in section 6.2.4, the overall mass balance on the adsorptive and on the adsorbed phase inside a ZLC reduces to a quite simple form which can be expressed as:

$$V_s \frac{d\bar{q}}{dt} + V_f \frac{dc}{dt} = F_{in} c_{in} - F_{out} c \tag{9.1}$$

The mass balance in Eq. (9.1) can be easily manipulated for the calculation of the mass transfer coefficient corresponding to an equivalent linear driving force model. This semi-experimental procedure can be adopted to assess if the adsorption kinetics can be well described by a linear driving force model or if a more complex kinetic model is requested. The linear driving force model can be expressed as:

$$V_s \frac{d\overline{q_{tot}}}{dt} = k_{ldf} A_s \left(q_{eq} - \overline{q_{tot}}\right) \tag{9.2}$$

Where k_{ldf} is the mass transfer coefficient, A_s is the external surface of the solid and q_{eq} is the adsorbed phase concentration at equilibrium with the gas phase concentration in the column. Eq. (9.2) can be inserted in Eq. (9.1) and the k_{ldf} can be calculated as a function of

$\overline{q_{tot}}$. using the experimental data obtained at each flowrate. For a desorption experiment, the equivalent linear driving force coefficient can be expressed as:

$$A_s k_{ldf}(\overline{q_{tot}}) = k'_{ldf}(\overline{q_{tot}}) = \frac{V_F \frac{dc_{zlc}}{dt} + F_{out} c_{zlc}}{\overline{q_{tot}} - q_{eq}} \tag{9.3}$$

In dimensionless form, eq. 9.3 can be expressed as:

$$K_{ldf}(\overline{q_{tot}}) = \frac{\gamma \frac{dC_{zlc}}{dt} + L C_{zlc}}{\overline{Q_{tot}} - Q_{eq}} \tag{9.3a}$$

Where the dimensionless parameter and variables were defined previously in Chapter 6. If the resistance to the mass transfer in the gas phase is negligible, $K_{ldf}(\overline{q_{tot}})$ should theoretically depend only on the average amount adsorbed and it should be independent on the desorption flowrate at which the experiment is performed. Therefore, If the $K_{ldf}(\overline{q_{tot}})$ shows a similar trend at the different flowrates then the linear driving force model can be considered a good approximation of the transport mechanism, otherwise different transport mechanism must be investigated.

The contribution of the external mass transfer resistance, i.e. the resistance in the gas phase, can be assessed considering an extremely conservative scenario. The solid can be assumed as made of as single crystal with the lowest specific surface and only a diffusion mechanism is present in the gas phase. The latter hypothesis implies assuming a Sherwood number equal to 2. The outer mass transfer coefficient can, therefore, be expressed as:

$$K_{out} = \frac{Sh\ D_m}{2\ R_p} \frac{A_s}{V_s} \tag{9.3b}$$

Where Sh is the Sherwood number; D_m is the molecular diffusivity; R_p is the particle/solid radius.

9.3 Combined diffusion model: Diffusion in a bed of mesoporous crystals

For the formulation of the diffusion model, Eq. (9.1) can be expressed in dimensionless form as:

$$\frac{d\overline{Q_{tot}}}{d\tau} + \gamma \frac{dC_{zlc}}{d\tau} = L(C_{in} - C_{zlc}) \tag{9.4}$$

The dimensionless parameters are defined as:

$$L = \frac{Fc_0}{\alpha V_s q_{0_{tot}}} \tag{9.5}$$

$$\gamma = \frac{V_f c_0}{V_s q_{0_{tot}}} \tag{9.6}$$

$$\tau = t\alpha \tag{9.7}$$

Where c_0 is the initial or the final concentration in the gas phase, $q_{0_{tot}}$ is the initial or the final concentration of adsorptive and adsorbate in the solid and α is the inverse of the diffusive time constant in the mesopores which can be defined as:

$$\alpha = \frac{D_0}{R^2} \tag{9.8}$$

Where D_0 is the corrected diffusivity of water in the mesopores and R is the characteristic diffusive length of the crystals. The mass balance in Eq. (9.4) is always valid either under kinetic or equilibrium control conditions and it is based on the main physical assumptions of the ZLC technique. The mass balance in the solid adsorbent depends on the mass transfer mechanism adopted and on the geometry of the solid. For a bed of mesoporous crystals, which represents the packing conditions of the solid inside the column, there are three different transport mechanisms. The gas phase molecular diffusion in the macroporous bed, the surface diffusion of the adsorbed phase inside the mesopores and the Knudsen diffusion of the gas phase inside the mesopores in parallel with the surface diffusion. The diffusion in the macroporous bed is in series with the other two diffusive mechanisms. The concentration of water in the gas phase is negligible compared to the concentration of water adsorbed. Therefore, the only relevant transport mechanism inside the mesopores is represented by the surface diffusion.

The set of differential equations describing the diffusion in a bed of mesoporous crystals is given by the mass balance in the macropores and the mass balance in the mesopores [97]. The diffusion equation in the macropores can be expressed as:

$$(1-\varepsilon)\frac{\partial \bar{q}}{\partial t} + \varepsilon\frac{\partial c}{\partial t} = \varepsilon\frac{D_m}{\tau}\left(\frac{\partial^2 c}{\partial x^2} + \frac{geobed}{x}\frac{\partial c}{\partial x}\right) \tag{9.9}$$

Where ε is the bed voidage, D_m is the molecular diffusivity, τ is the bed tortuosity, c is the gas phase concentration, $\bar{q}$ is the average concentration of adsorbate in the mesopores, $geobed$ is the geometric coefficient of the bed and x is the bed spatial coordinate. $geobed$ is 0 for slab

geometry, 1 for cylindrical geometry and 2 for spherical geometry. The dimensionless form of Eq. (9.9) can be expressed as:

$$\frac{\partial C}{\partial \tau} = -\frac{1}{\delta}\frac{\partial \bar{Q}}{\partial \tau} + \frac{\beta}{\alpha}\left(\frac{\partial^2 C}{\partial {\xi_b}^2} + \frac{geobed}{\xi_b}\frac{\partial C}{\partial \xi_b}\right) \tag{9.10}$$

Where $\xi_b = \frac{x}{L_{bed}}$ is the dimensionless bed spatial coordinate and L_{bed} is the characteristic diffusive length of the bed. The dimensionless parameter δ is given by:

$$\delta = \frac{\varepsilon c_0}{(1-\varepsilon)q_0} \tag{9.11}$$

Where q_0 is the initial or the final concentration of adsorbate in the solid. The inverse of the bed diffusive time constant is expressed as:

$$\beta = \frac{D_m}{{L_{bed}}^2} \tag{9.12}$$

The diffusion equation in the mesopores [94] can be expressed as:

$$(1-\varepsilon_{meso})\frac{\partial q}{\partial t} + \varepsilon_{meso}\frac{\partial c_{meso}}{\partial t} = \varepsilon_{meso} D_k\left(\frac{\partial^2 c}{\partial r^2} + \frac{geomeso}{r}\frac{\partial c}{\partial r}\right) + (1-\varepsilon_{meso})\left(D_s\frac{\partial^2 q}{\partial r^2} + D_s\frac{geomeso}{r}\frac{\partial q}{\partial r} + \frac{\partial D_s}{\partial r}\frac{\partial q}{\partial r}\right) \tag{9.13}$$

Where ε_{meso} is the mesopore voidage; c_{meso} is the concentration in the gas phase inside the mesopore; D_k is the Knudsen diffusivity; D_s is the surface diffusivity; r is the mesopore spatial coordinate and $geomeso$ is the geometric coefficient of the crystal and it is defined in the same way as $geobed$. The transport surface diffusivity D_s is correlated to the local amount adsorbed using the Darken correction factor as:

$$D_s = D_0 D_f = D_0\frac{q_{eq}}{c_{meso}}\frac{dc_{meso}}{dq_{eq}} \tag{9.14}$$

Where D_0 is the corrected diffusivity, D_f is the Darken correction factor and q_{eq} is the adsorbed phase concentration at equilibrium with the gas phase concentration c_{meso}. The dimensionless form of Eq. (9.13) can be expressed as:

$$\frac{\partial \mathrm{Q}}{\partial \tau} + \frac{\mathrm{c_0}\varepsilon_{\mathrm{meso}}}{\mathrm{q_0}(1-\varepsilon_{\mathrm{meso}})}\frac{\partial \mathrm{C}}{\partial \tau} = \frac{\mathrm{c_0}\varepsilon_{\mathrm{meso}}}{\mathrm{q_0}(1-\varepsilon_{\mathrm{meso}})}\frac{\mathrm{D_k}}{\mathrm{D_0}}\left(\frac{\partial^2 \mathrm{C}}{\partial {\xi_\mathrm{m}}^2} + \frac{\mathrm{geomeso}}{\xi_\mathrm{m}}\frac{\partial \mathrm{C}}{\partial \xi_\mathrm{m}}\right) + \left(\mathrm{D_f}\frac{\partial^2 \mathrm{Q}}{\partial {\xi_\mathrm{m}}^2} + \mathrm{D_f}\frac{\mathrm{geomeso}}{\xi_\mathrm{m}}\frac{\partial \mathrm{Q}}{\partial \xi_\mathrm{m}} + \frac{\partial \mathrm{D_f}}{\partial \xi_\mathrm{m}}\frac{\partial \mathrm{Q}}{\partial \xi_\mathrm{m}}\right) \tag{9.15}$$

Where $\xi_m = \frac{r}{L_{meso}}$ is the dimensionless mesopores spatial coordinate and L_{meso} is the characteristic diffusive length of the mesopores. Considering that the concentration c_0 of water in the gas phase is negligible compared to the concentration q_0 of water in the adsorbed phase, Eq. (9.15) can be simplified and expressed as:

$$\frac{\partial Q}{\partial \tau} = D_f \frac{\partial^2 Q}{\partial {\xi_m}^2} + D_f \frac{geomeso}{\xi_m} \frac{\partial Q}{\partial \xi_m} + \frac{\partial D_f}{\partial \xi_m} \frac{\partial Q}{\partial \xi_m} \tag{9.16}$$

9.4 Equilibrium isotherm and Darken correction factor calculation

The equilibrium isotherm can be measured by running a complete adsorption-desorption cycle at low flowrates. The system reaches equilibrium control conditions and the integration of Eq. (9.1) provides the average amount adsorbed at equilibrium with the concentration in the gas phase expressed beforehand as c_{zlc}. More details about the measurement and the calculation of the equilibrium isotherm can be found in section 8.2.3. The calculated equilibrium isotherm is shown in fig. 9.1. The equilibrium isotherm is needed for the formulation and solution of the kinetics model [98,99]. The isotherm is used as boundary condition for the mass balance in the mesopores and it is necessary for the calculation of the darken correction factor. In fig. 9.2, the Darken correction factor calculated using the adsorption and the desorption branches of the isotherm is reported together with the normalized adsorption-desorption isotherm. It is possible to observe how the Darken factor predicts a significant drop of the transport diffusivity in the region of capillary condensation and evaporation. The highest value of transport diffusivity is predicted at the concentration of saturation of the solid.

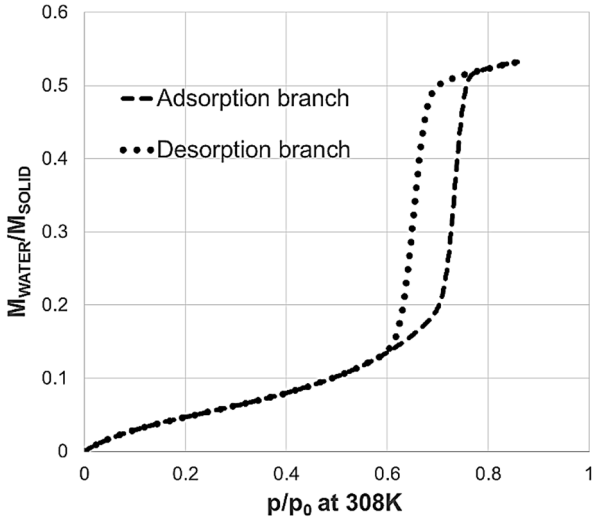

Figure 9.1 – Adsorption-desorption equilibrium isotherm measured on the ZLC at 308K. Sample mass 1.2 mg

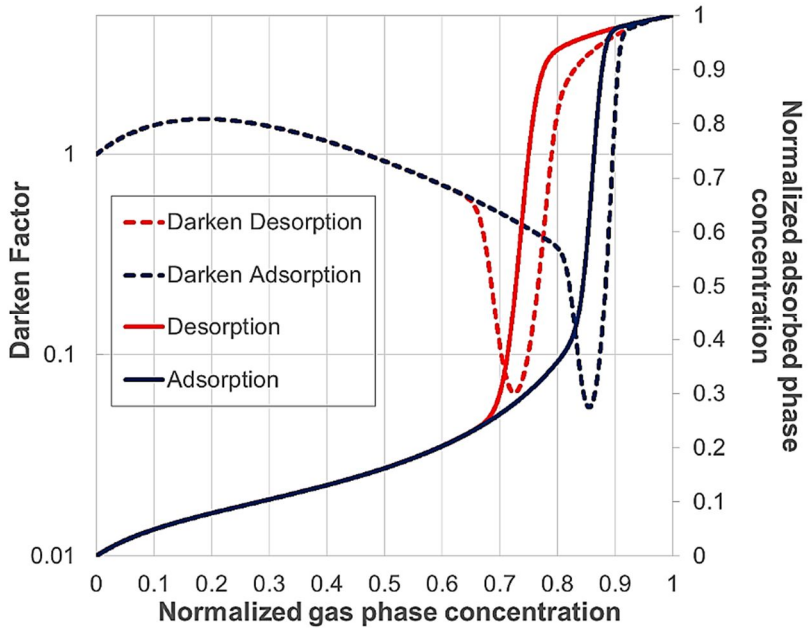

Figure 9.2 – Calculated Darken correction factor for the adsorption-desorption isotherm shown in fig. 9.1.

9.5 Bed/Macropores diffusion model

The bed/macropores diffusion control model represents an extreme case of the combined diffusion model in which the concentration along each mesopore is constant and at equilibrium with the local concentration along the bed. In this case, Eq. (9.9) can be rearranged considering that the average amount adsorbed in each mesopore is at equilibrium with the local gas phase concentration in the bed. Therefore, the mass balance in the bed can be expressed as:

$$\frac{\partial c}{\partial t} = \frac{\varepsilon \frac{Dm}{\tau}}{\varepsilon + (1-\varepsilon)\frac{\partial q_{eq}}{\partial c}} \left(\frac{\partial^2 c}{\partial x^2} + \frac{geobed}{x} \frac{\partial c}{\partial x} \right) \tag{9.17}$$

Eq. (9.17) can be expressed in dimensionless form as:

$$\frac{\partial C}{\partial \tau} = \frac{1}{1 + \frac{1}{\delta}\frac{\partial Q_{eq}}{\partial C}} \left(\frac{\partial^2 C}{\partial {\xi_b}^2} + \frac{geobed}{\xi_b} \frac{\partial C}{\partial \xi_b} \right) \tag{9.18}$$

The inverse of the bed/macropores diffusive time constant was expressed in Eq. (9.18a) as:

$$\beta = \frac{D_m}{{L_{bed}}^2} \tag{9.18a}$$

Eq. (9.18) can give results quite similar to the results predicted by the combined diffusion model as the derivative of the isotherm gives a contribution to the effective diffusivity which is similar to the darken correction factor. The comparison between the Darken correction factor

and the inverse of the derivative of the isotherm is reported in fig. 9.3. Both functions are calculated for the desorption branch of the isotherm.

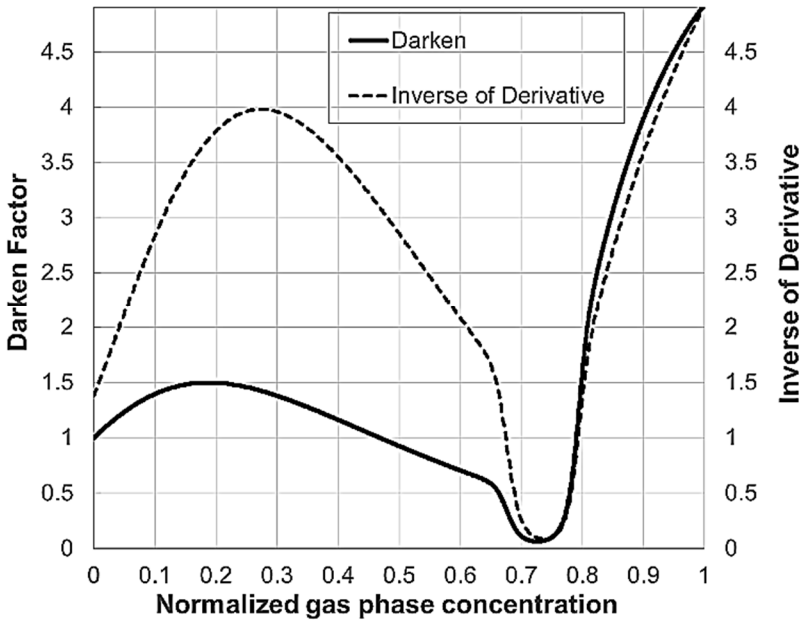

Figure 9.3 – Calculated Darken correction factor and inverse of the derivative of the isotherm for the desorption branch of the isotherm shown in fig. 9.1.

9.6 Mesopores diffusion model

For the case in which the diffusion in the bed is fast enough and the diffusion in the mesopores is controlling the overall mass transfer, the solution of the mass balance in the mesopores gives the transient uptake in the solid. Therefore, the mesopores diffusion model represents an extreme case of the combined diffusion model. In this scenario, the mass transport inside the solid can be described by the diffusion equation in the mesopores expressed before in Eq. (9.19) as:

$$\frac{\partial Q}{\partial \tau} = D_f \frac{\partial^2 Q}{\partial {\xi_m}^2} + D_f \frac{geomeso}{\xi_m} \frac{\partial Q}{\partial \xi_m} + \frac{\partial D_f}{\partial \xi_m} \frac{\partial Q}{\partial \xi_m} \tag{9.19}$$

9.7 Heat effects

For the formulation of the energy balance, the most conservative scenario was considered in order to maximize the heat effects [100]. The solid was considered as composed of a single crystal with an evident much lower surface area than the actual one. The heat of adsorption was assumed constant and it was approximated to 1.2 times the heat of vaporization of water [101]. The heat capacity of silica was considered for the calculation of the energy accumulation in the

solid while the heat capacity of water was neglected. The Nusselt number was assumed to be equal to 2 for the evaluation of the external heat transfer coefficient. This represents an extremely conservative assumption considering that a gas flow is constantly passing through the column. The thermal conductivity of the gas phase was approximated with the thermal conductivity of the carrier gas. The energy balance in the solid adsorbent can be approximated by an enthalpy balance which can be expressed as:

$$\frac{d\bar{T}}{dt} = -\frac{\Delta H_{ads} V_s}{M_s Cp}\frac{d\overline{q_{tot}}}{dt} - \frac{hA_s}{M_s Cp}\left(\bar{T} - T_g\right) \tag{9.20}$$

Where $\bar{T}$ is the average temperature of the solid, T_g is the temperature of the gas phase, ΔH_{ads} is the heat of adsorption, M_s is the mass of the solid, Cp is heat capacity of the solid, A_s is the external surface of the solid and h is the external heat transfer coefficient. The dimensionless form of Eq. (9.20) can be expressed as:

$$\frac{d\theta_s}{d\tau} = -\lambda\frac{d\overline{Q_{tot}}}{d\tau} - \frac{\sigma}{\alpha}(\theta_s - 1) \tag{9.21}$$

Where θ_s is the dimensionless temperature of the solid; The dimensionless parameters are expressed as:

$$\lambda = \frac{\Delta H_{ads} V_s q_0}{M_s Cp T_g} \tag{9.22}$$

$$\sigma = \frac{hA_s}{M_s Cp} \tag{9.23}$$

9.8 Solution methods for the mass balances

The set of dimensionless partial differential equations was solved as a system of ordinary differential equations after discretizing the space derivatives. For the calculation of the outlet flowrate expressed in Eq. (9.1) the flowrate correction described in [11], and expressed by Eq. (9.32) in section 6.2.5, was adopted. The methods of finite differences and orthogonal collocation on finite elements were applied to discretize the space derivatives. For the simulation with the highest flowrate, which is characterized by the steepest change in both bed concentration and solid concentration profiles, 150 discretization points were used to discretize the spatial coordinate in the crystal and 50 discretization points were used to discretize the spatial coordinate in the bed. For the lowest flowrate, corresponding to equilibrium control conditions, respectively 25 and 15 discretization points were used. Mathcad, MATLAB and gPROMS were used for the solution of the differential equations.

The initial conditions for Eq. (9.1) are given by:

At $t = 0$; $C_{zlc} = 1$ for desorption and $C_{zlc} = 0$ for adsorption. (9.24)

At $t = 0$; $\overline{Q_{tot}} = 1$ for desorption and $\overline{Q_{tot}} = 0$ for adsorption. (9.25)

The initial and boundary conditions for Eq. (9.10) are given by:

At t= 0 ; $C = 1$ for desorption and $C = 0$ for adsorption. (9.26)

For $\xi_b = 0$; $\frac{\partial C}{\partial \xi_b} = 0$ or the symmetry conditions can be applied. (9.27)

For $\xi_b = 1$; $C = C_{zlc}$ (9.28)

The boundary condition in Eq. (9.27) can be replaced by the symmetry condition which can be expressed as:

For $\xi_b = 0$; $\frac{\partial C}{\partial \xi_b} = -\frac{1}{\delta}\left(\frac{\partial \bar{Q}}{\partial \tau}\right)_{\xi_b=0} + \frac{\beta}{\alpha}\left(\frac{\partial^2 C}{\partial {\xi_b}^2}\right)_{\xi_b=0}$ (9.29)

The initial and boundary conditions of Eq. (9.16) are given by:

At $t = 0$; $Q = 1$ for desorption and $Q = 0$ for adsorption. (9.30)

For $\xi_m = 0$; $\frac{\partial Q}{\partial \xi_m} = 0$ or the symmetry condition can be applied. (9.31)

For $\xi_m = 1$; $Q = Q_{eq}(C)$ (9.32)

The boundary condition in Eq. (9.31) can be replaced by the symmetry condition which can be expressed as:

For $\xi_m = 0$; $\frac{\partial Q}{\partial \xi_m} = \left(D_f \frac{\partial^2 Q}{\partial {\xi_m}^2}\right)_{\xi_m=0}$

The initial conditions of Eq. (9.19) are given by:

At $t = 0$; $\theta = 1$ for desorption and adsorption. (9.33)

The total average amount of adsorptive and adsorbate inside the solid can be expressed as:

$$\overline{Q_{tot}} = \frac{\delta}{\delta+1}(geobed + 1)\int_0^1 C\,{\xi_b}^{geobed} d\xi_b + \frac{1}{\delta+1}(geobed + 1)\int_0^1 \bar{Q}\,{\xi_b}^{geobed} d\xi_b \quad (9.34)$$

The average amount adsorbed in the mesopore can be expressed as:

$$\bar{Q} = (geomeso + 1)\int_0^1 Q\,{\xi_m}^{geomeso} d\xi_m \quad (9.35)$$

The time derivatives of the average concentration can be expressed either deriving Eqs 34-35 or through the flux at the surfaces of the bed and of the crystals [34] as:

$$\frac{d\overline{Q_{tot}}}{d\tau} = \frac{\delta}{\delta+1}(geobed+1)\frac{\beta}{\alpha}\left(\frac{\partial C}{\partial \xi_b}\right)_{\xi_b=1} + \frac{1}{\delta+1}(geobed+1)\left(\mathrm{D_f}\frac{\partial \bar{Q}}{\partial \xi_b}\right)_{\xi_b=1} \tag{9.36}$$

$$\frac{\partial \bar{Q}}{\partial \tau} = (geomeso+1)\left(\mathrm{D_f}\frac{\partial Q}{\partial \xi_m}\right)_{\xi_m=1} \tag{9.37}$$

Both methods for the calculation of the derivatives of the average amount of adsorptive in the bed and of the average amount of adsorbate in the solid gave the same results. However, for the accurate calculation of the diffusive fluxes at the surfaces, more elements or discretization points are needed, and longer calculations time are requested.

9.9 Conclusions

A semi-experimental procedure for the evaluation of the equivalent linear driving force model was defined in order to be applied specifically to the ZLC experiments. The procedure is intended to calculate the variation of the equivalent linear driving force mass transfer coefficient with the average amount adsorbed.

A mass transfer mechanism which considers the diffusion in a bed of crystal in series with the diffusion inside the mesopores and the two extreme subcases of bed diffusion controlling and mesopore diffusion controlling were formulated and derived. The mass balances were derived in dimensionless form to highlight the dimensionless parameters and diffusive time constants. The formulation of such models is justified by the experimental procedure in which the solids were packed inside the column. SBA-15 is a fine powder and the crystals can agglomerate into bigger clusters when filling up the column. Silica-gel is instead composed of irregular pellets with average dimensions of 0.165mm and agglomeration effect can be excluded in such a case. The Darken correction factor was used in the mesopore diffusion model to locally correlate the transport diffusivity coefficient to the amount adsorbed. Interestingly, the calculation of the Darken correction factor for a type IV isotherm shows a minimum for concentrations located in the hysteresis region of the equilibrium isotherm.

10 ZLC kinetic measurements

10.1 Introduction

The desorption kinetics of water vapor in SBA-15 powder and silica-gel pellets was investigated at 308.15 K by using the ZLC technique. A comparison among different kinetic models was carried out to better understand the mass transport mechanism of water vapor in the two solid adsorbents. The equivalent linear-driving-force mass transfer coefficient was experimentally found to strongly depend on the concentration of water adsorbed and on the desorption flowrates for both solid adsorbents. The mass transport of water vapor in SBA-15 powder and silica-gel was demonstrated to be controlled by a macroporous diffusive process in the entire range of adsorbed concentration, from dry solid up to full saturation of the pores. Considering the particular structural and chemical characteristics of SBA-15 and silica-gel, the study was initially meant to investigate the mass transport mechanism of an adsorbing-condensing vapor inside a well-defined mesoporous channel and inside a mesoporous pore-network. However, the inevitable agglomeration of the SBA-15 crystals generated a strong resistance for the water vapor transport in the bed of SBA-15 particles. A similar scenario was observed for silica-gel, in which the mass transfer mechanism was controlled by a macroporous diffusion process. The ZLC technique allowed to clearly identify the controlling mass transfer mechanism by using two different carrier gases and by minimizing secondary effects. Heat effects were proved to be negligible by performing a simple and extremely conservative energy balance on the solid using the experimental average amount adsorbed.

10.2 SBA-15

The first experiments were performed to assess the kinetic control conditions of the system. In fig. 10.1 and fig. 10.2 it is possible to observe respectively the Ft plots of several desorption and adsorption experiments conducted at different flowrates. The Ft plots clearly show the kinetic control conditions of the system for both the adsorption and the desorption experiments. It is interesting to notice how the curves tend to diverge starting from the almost horizontal parts which correspond to the capillary condensation and evaporation regions of the equilibrium isotherm. This represents a useful and straightforward method in case of large concentration change because it permits to simply visualize at which concentration the mass transport is slower. It can be experimentally observed that the slowest mass transport occurs in

the region of the isotherm characterized by the capillary condensation and evaporation phenomena.

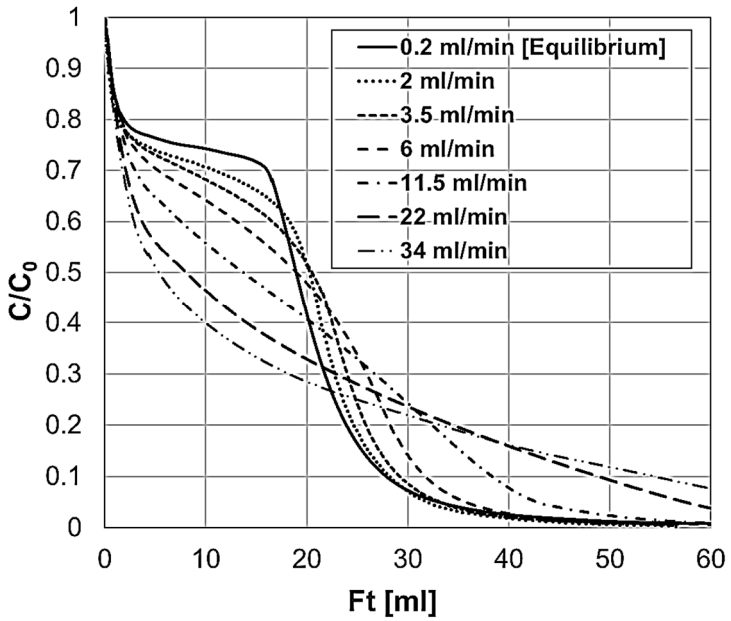

Figure 10.1 – Ft-plot for water vapor on SBA-15. Desorption experiments measured at different flowrate at 308K. Sample mass 1.2 mg.

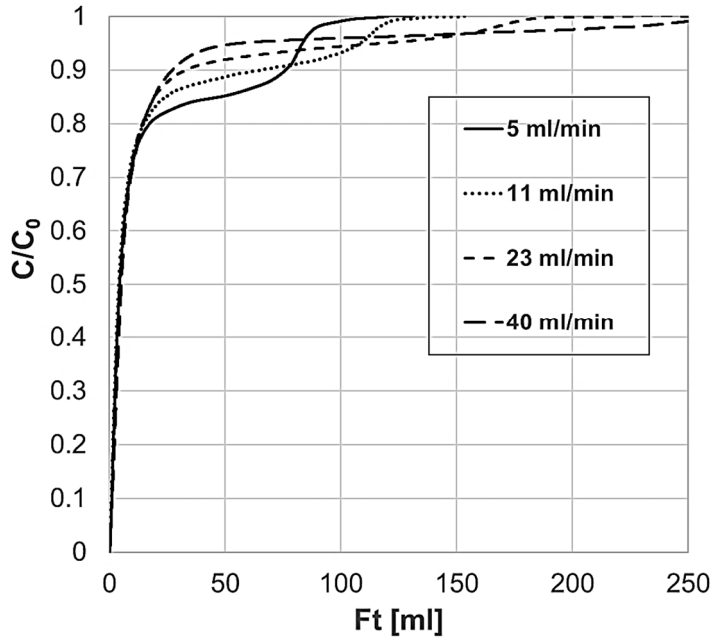

Figure 10.2 – Ft-plot for water vapor on SBA-15. Adsorption experiments measured at different flowrate at 308K. Sample mass 1.2 mg.

An even more efficient way to visualize the dependence of the mass transfer on the concentration is given by the integration of the mass balance. In this case, the equilibrium adsorption-desorption isotherm is obtained from the data measured under equilibrium control conditions while the average amount adsorbed is obtained from the data measured under kinetic control conditions. In fig. 10.3, the integration of the desorption curves shown in fig. 10.1 is

reported. As expected, all the curves start from the same initial adsorbed concentration. This validates the consistency of the mass balance at the different flowrates. The overlapped regions of the curves are under equilibrium control conditions while the regions of the curves that diverge show a limitation from the mass transport kinetics. In this case, the mass transport kinetics limitations are visualized at different average adsorbed amounts. With this representation, it is possible to observe more clearly how the curves tend to diverge starting from the onset of capillary evaporation while the high concentration and the low concentration parts of the isotherm show a faster mass transport. In particular, from the 2 ml/min and 3.5 ml/min experiments, it can clearly be observed that the system starts from equilibrium control conditions. Afterward the system shows kinetic limitations in the capillary evaporation region and finally, it returns to equilibrium conditions in the low concentration region. By increasing the flowrate, the kinetic limitations spread over a bigger concentration range up to low concentrations. Only the first part of the curves, which corresponds to the saturation of the pores, shows extremely fast desorption kinetics.

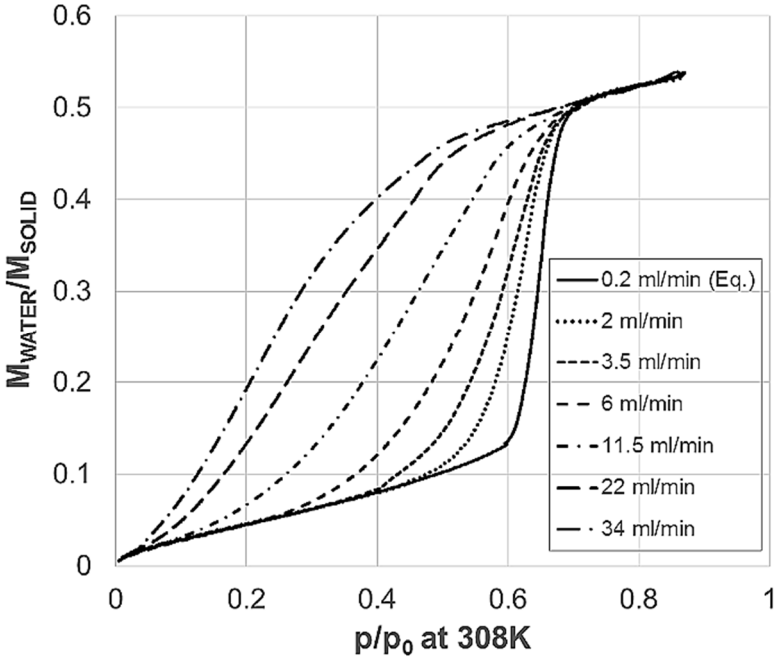

Figure 10.3 – Average amount adsorbed calculated from the different desorption experiments at different flowrate (fig. 10.1). 0.2 ml/min (equilibrium control conditions) corresponds to the equilibrium desorption isotherm.

10.2.1 SBA-15: Equivalent linear driving force model

The application of the semi-experimental procedure to evaluate the LDF model requires the simultaneous solution of the mass balance and the calculation of the time derivative of the experimental concentration signal expressed in section 9.2. The final expression for the

calculation of the equivalent linear driving force mass transfer coefficient was introduced in section 9.2 as:

$$K_{ldf}(\overline{q_{tot}}) = \frac{\gamma\frac{dC_{zlc}}{dt}+LC_{zlc}}{\overline{Q_{tot}}-Q_{eq}} \tag{10.1}$$

The derivative was calculated analytically using localized parabolic functions to piece-wisely filter the experimental concentration signal. The solution of the mass balance is to be calculated for the equilibrium experiment and for the kinetic experiments simultaneously at the same concentration in the gas phase c_{zlc}. The graph in fig. 10.4 shows how the equivalent linear driving force mass transfer coefficient changes with the average amount adsorbed for several desorption flowrates. The k_{ldf} is strongly dependent on the average amount adsorbed and as expected it tends to infinite when the system approaches equilibrium control conditions at low and high concentrations. The k_{ldf} is also strongly dependent on the desorption flowrate and it varies up to a factor of 5 between the highest and smallest flowrate used. These results would already be sufficient to claim that the kinetics cannot be well represented by such a model as the LDF mass transfer coefficient should theoretically be independent on the flowrate and it should depend only on the average amount adsorbed.

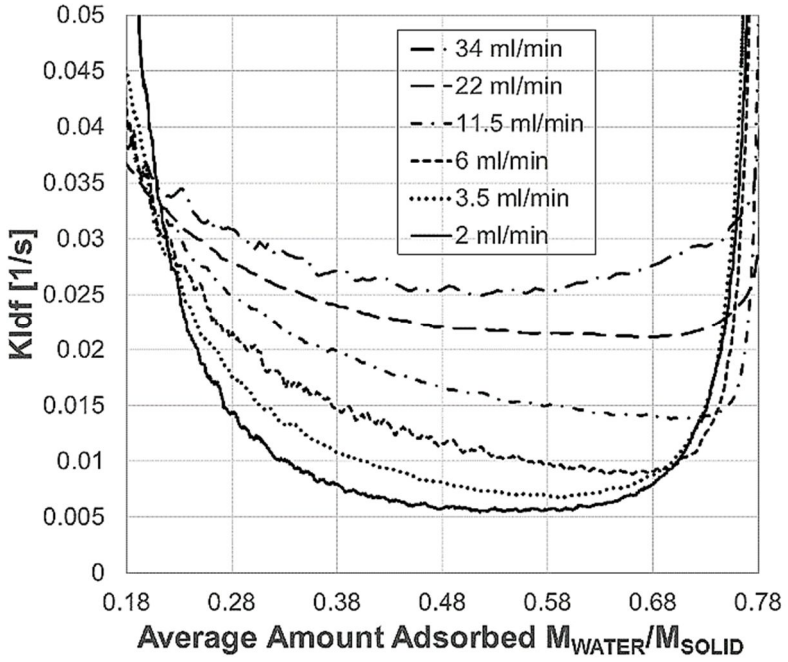

Figure 10.4 – Semi-experimental calculation of the equivalent linear driving force mass transfer coefficients at different flowrates for water vapor on SBA-15.

To further prove the inefficiency of the LDF model, the experimental k_{ldf} calculated at the highest flowrate as a function of the average amount adsorbed was empirically correlated with

a best-fitting rational function and used for the simulation and prediction of the experimental desorption data at the other flowrates. The empirical rational function contains 8 fitting parameters at the numerator and 7 fitting parameters at the denominator. In figs. 10.5-10.10, it is possible to observe the prediction of the linear driving force model for different flowrates. The prediction of the highest flowrate is perfect as expected. However, the prediction becomes worse as the flowrates departs furthermore from the reference one. This proves that the equivalent k_{ldf} depends also on the desorption flowrate and that the linear driving force model is not able to carefully represent the mass transport mechanism. The slowest flowrate shown in fig. 10.10 corresponds to equilibrium control conditions. The prediction is very good because the response desorption curve does not depend on the kinetic model used but only on the shape of the equilibrium isotherm.

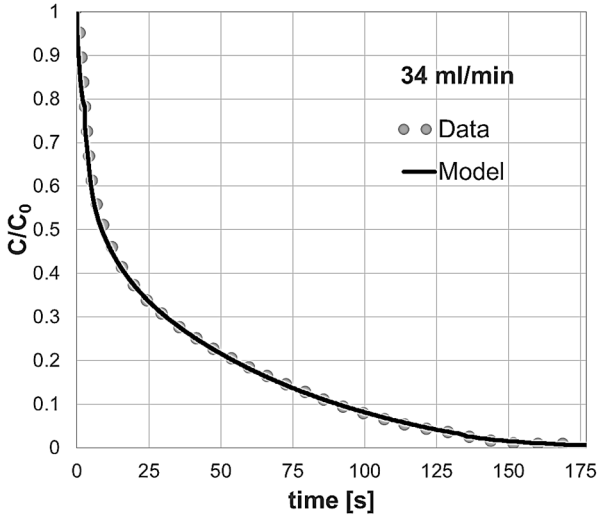

Figure 10.5 – Simulated desorption curve at 34 ml/min using the experimental calculated linear driving force coefficient at 34 ml/min.

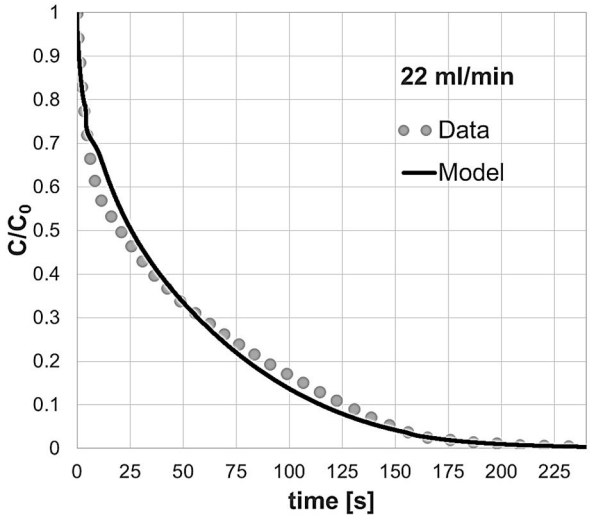

Figure 10.6 – Simulated desorption curve at 22 ml/min using the experimental calculated linear driving force coefficient at 34 ml/min.

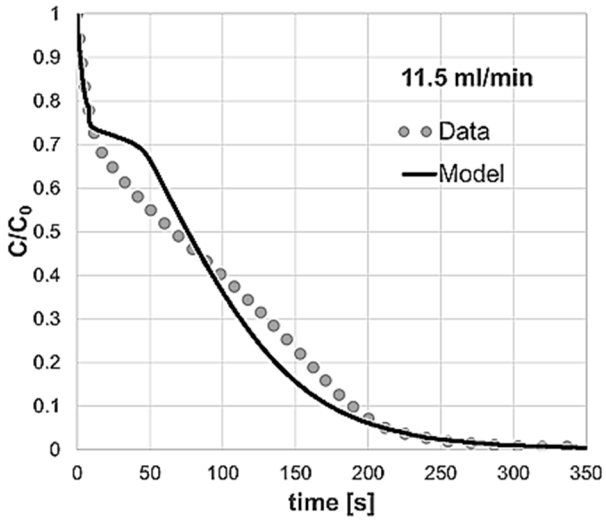

Figure 10.7 – Simulated desorption curve at 11.5 ml/min using the experimental calculated linear driving force coefficient at 34 ml/min.

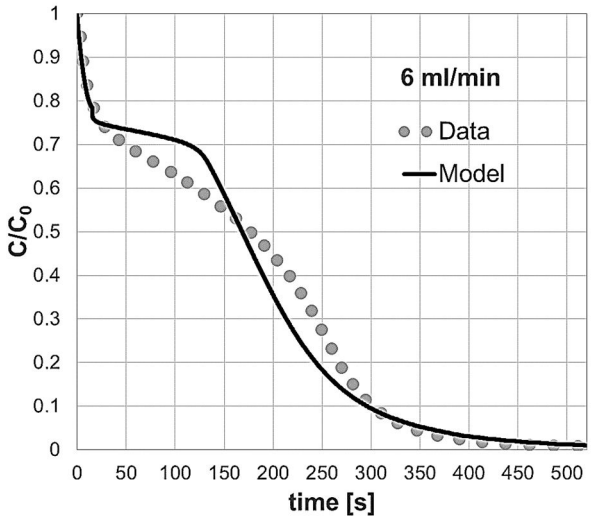

Figure 10.8 – Simulated desorption curve at 6 ml/min using the experimental calculated linear driving force coefficient at 34 ml/min.

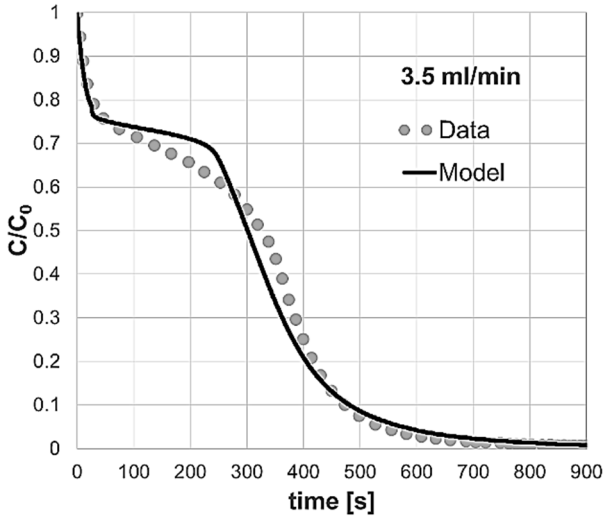

Figure 10.9 – Simulated desorption curve at 3.5 ml/min using the experimental calculated linear driving force coefficient at 34 ml/min.

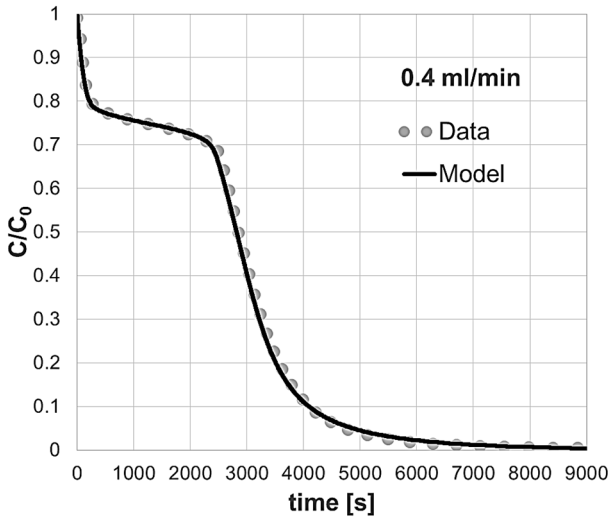

Figure 10.10 – Simulated desorption curve at 0.4 ml/min using the experimental calculated linear driving force coefficient at 34 ml/min. The experiment shown represents equilibrium control conditions.

The contribution of the external mass transfer resistance can be estimated as reported in section 9.2. The sample mass used for the kinetics experiment is equal to 1.2 mg. The density of silica is equal to 2.65 gm/cm^3. The diameter, surface area and volume of the hypothetical single crystal are, therefore, easily calculated respectively as 0.0476 cm, 0.026 cm^{2,} and 4.52*10^{-4} cm^3. The calculation of the external mass transfer coefficient according to Eq. (9.3b).

$$K_{out} = \frac{Sh\ D_m}{2\ R_p}\frac{A_s}{V_s} = 339\ s^{-1}$$

This value is four orders of magnitude larger than the values of K_{ldf} presented in fig. 10.4. Therefore, external contributions to the mass transfer resistance can be considered negligible.

10.2.2 SBA-15: Bed/Macropores diffusion model

In a scenario in which the mass transfer is controlled by the diffusion in the macropores, the concentration inside the mesopores can be considered constant and at equilibrium with the corresponding concentration along the bed/macropore. The differential mass balance for a bed/macropores controlled diffusion process was expressed in section 9.5 as:

$$\frac{\partial C}{\partial \tau} = \frac{1}{1+\frac{1}{\delta}\frac{\partial Q_{eq}}{\partial C}}\left(\frac{\partial^2 C}{\partial {\xi_b}^2} + \frac{geobed}{\xi_b}\frac{\partial C}{\partial \xi_b}\right) \tag{10.2}$$

The only fitting parameter is given by the inverse of the bed/macropores diffusive time constant which was expressed in section 9.3 as:

$$\beta = \frac{D_m}{{L_{bed}}^2} \tag{10.3}$$

In figs. 10.11-10.17, it is possible to observe the prediction of the bed/macropores diffusion model for the different flowrates using two different carrier gas. The experiments performed with two different carrier gases at the same flowrate showed different experimental response curves which can be near-perfectly predicted by changing the two diffusive time constants according to the different molecular diffusivity of water vapor in the two gases [102]. Nitrogen and helium can be considered as inert in this study and the relevant difference in their molecular weight is helpful for the evaluation of eventual macropores diffusion controlling mechanisms. The experimental desorption curves were measured using different flowrates from kinetic control conditions up to equilibrium control conditions. For the five highest flowrates, the response curves were measured using both carrier gases. The effect of the carrier gas on the shape of the response curve is evident, and this proves the controlling effect operated by the diffusive mass transfer in the bed of crystals.

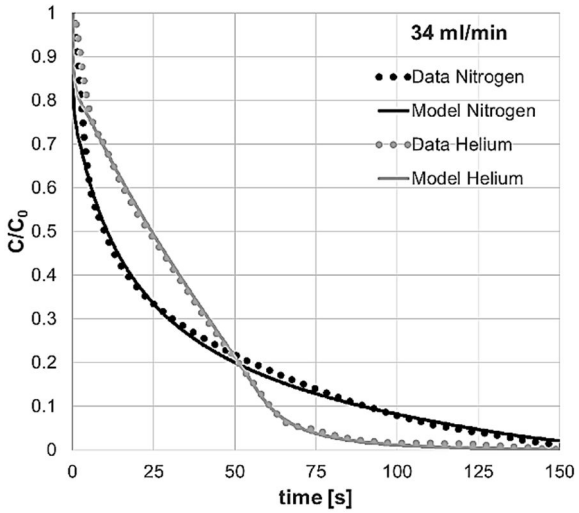

Figure 10.11 – Experimental and predicted response curves for a desorption experiment conducted at 34 ml/min using nitrogen and helium as carrier gas

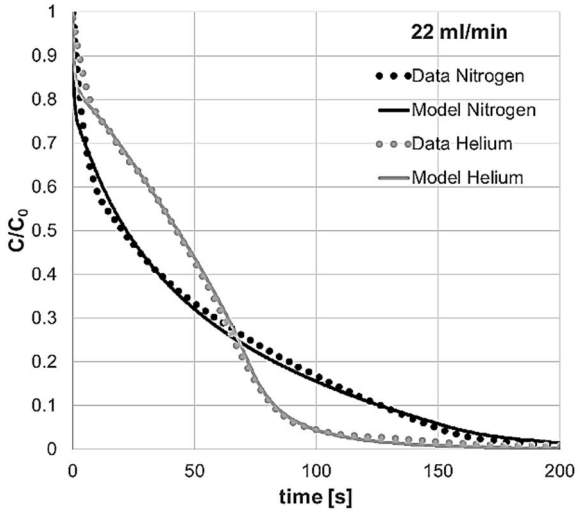

Figure 10.12 – Experimental and predicted response curves for a desorption experiment conducted at 22 ml/min using nitrogen and helium as carrier gas.

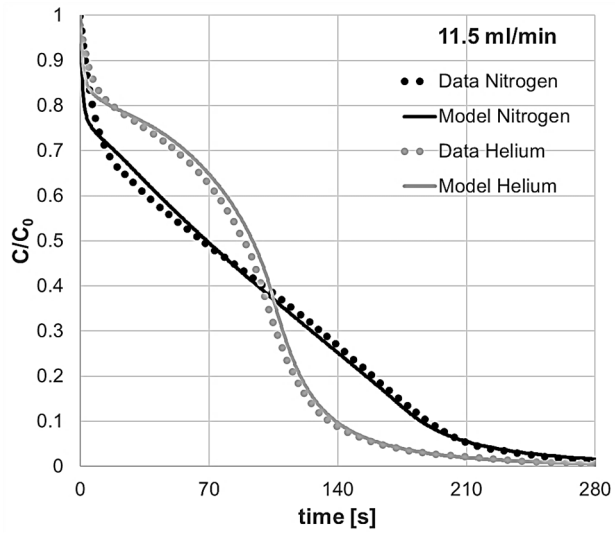

Figure 10.13 – Experimental and predicted response curves for a desorption experiment conducted at 11.5 ml/min using nitrogen and helium as carrier gas.

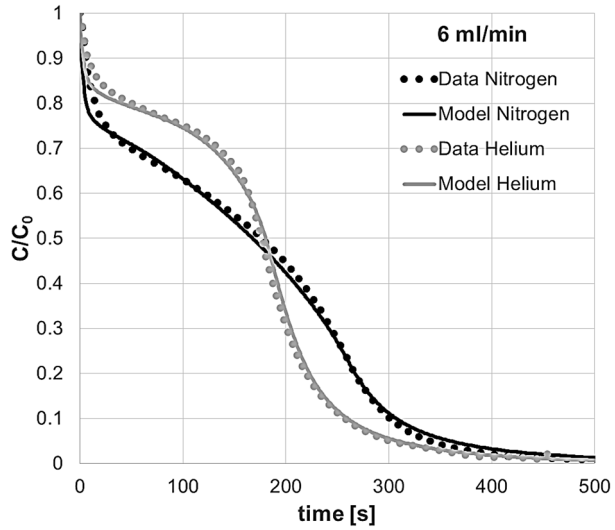

Figure 10.14 – Experimental and predicted response curves for a desorption experiment conducted at 6 ml/min using nitrogen and helium as carrier gas.

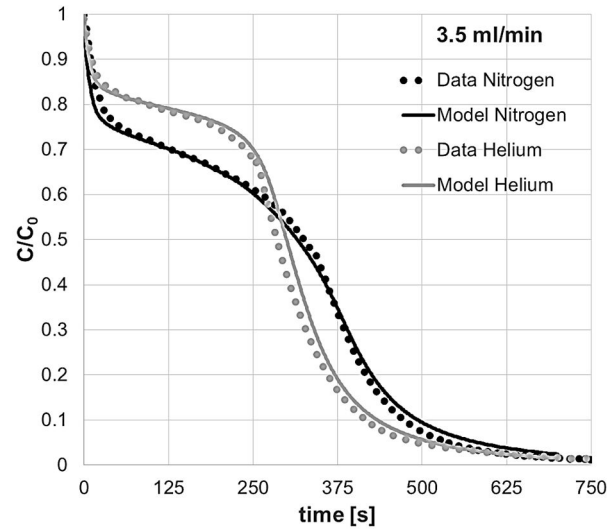

Figure 10.15 – Experimental and predicted response curves for a desorption experiment conducted at 3.5 ml/min using nitrogen and helium as carrier gas and the combined diffusion model. Equilibrium control conditions.

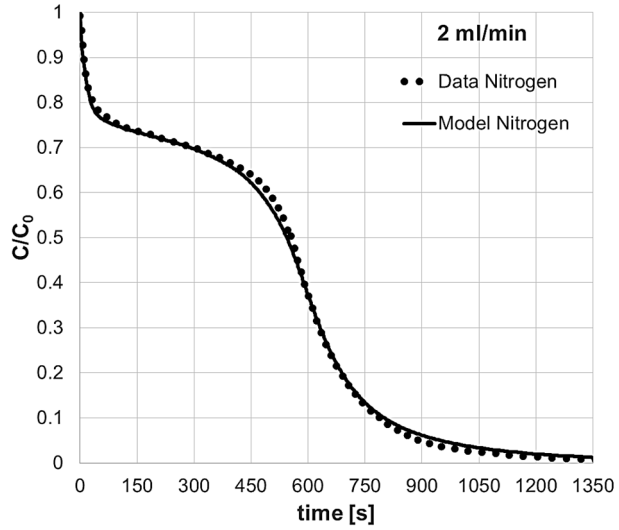

Figure 10.16 – Experimental and predicted response curves for a desorption experiment conducted at 2 ml/min using nitrogen as carrier gas and the bed diffusion model. Equilibrium control conditions.

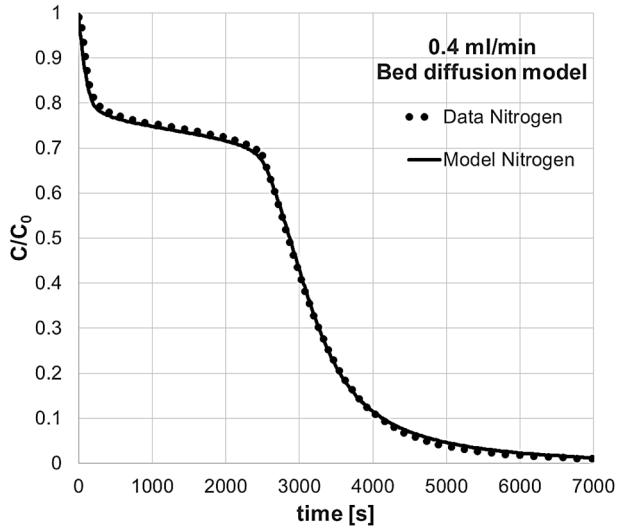

Figure 10.17 – Experimental and predicted response curves for a desorption experiment conducted at 0.4 ml/min using nitrogen as carrier gas and the bed diffusion model. Equilibrium control conditions.

The diffusion model can well predict the response curve for all the flowrates and for both carrier gases. There is only one parameter β to be adjusted for the best correlation of all the experimental curves for both carrier gasses from kinetic up to equilibrium control conditions. All the other dimensionless parameters expressed in the set of differential equations are given by the experimental conditions used and they can be calculated *a priori*.

The values of the parameters used for the simulation of the desorption curves with the two different carrier gas are reported in table 10.1.

Table 10.1 – Values of the parameters used for the simulation of the bed/macroporous diffusion model.

	Desorption N_2	**Desorption He**
***L* (highest flowrate)**	$1.4*10^{-3}$	$3.98*10^{-4}$

γ	0.0262	0.0262
$\beta\ [s^{-1}]$	22.5	79.2
δ	0.0001	0.0001
$geobed$	2	2

The L parameter reported in table 10.1 corresponds to the highest flowrate. The value of the L parameter for the other flowrates can be easily calculated considering that the parameter is linearly proportional to the flowrate. Considering that the diffusion coefficient of water vapour in nitrogen is 0.256 cm^2s^{-1} [102] and assuming a tortuosity factor of 2.5 for the bed of SBA-15 agglomerates, the value of the diffusive time constant in the bed corresponds to a diffusive length of 0.675 mm. This value can be reasonable if one considers how SBA-15 powder is packed inside the column.

Considering these results, a different procedure for the loading of the SBA-15 powder inside the column was adopted with the intention of minimizing the bed diffusion effects. The powder was initially dispersed in rock-wool and then loaded, together with the rock-wool, inside the column. The experimental response curves and the predictions of the models are reported in figs 10.18-10.19. As it is possible to observe, the mass transport kinetics was still strongly controlled by the molecular diffusion in the macroporous bed. The better dispersion of the solid can be observed from the lower value of time constant reported in table 10.2.

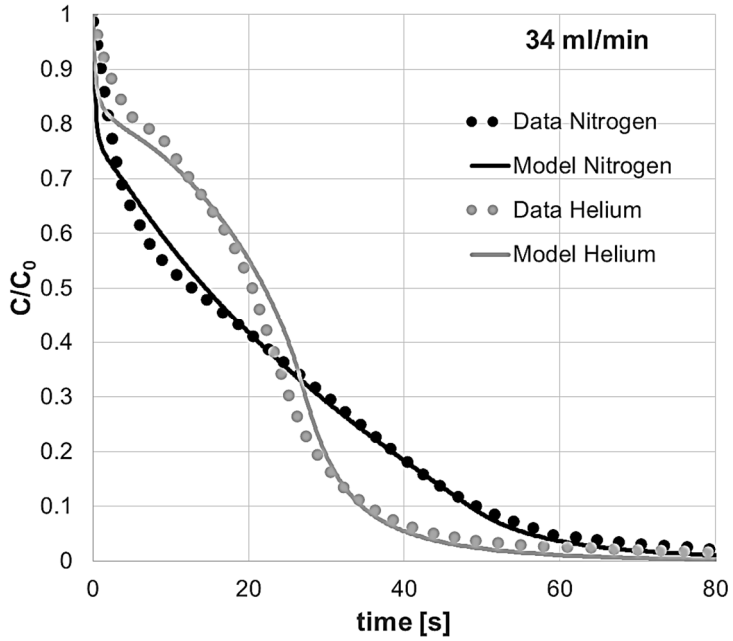

Figure 10.18 – Experimental and predicted response curves for a desorption experiment conducted at 34 ml/min using nitrogen and helium as carrier gas.

The values of the parameters used for the simulation of the desorption curves with the two different carrier gas are reported in table 10.2. The agglomeration of the SBA-15 crystals into bigger particles can be spotted from the SEM pictures collected on the sample. The amount of

sample loaded on the analysis-plate was hardly visible to the naked eye. However, the agglomeration is still quite visible in Figs. 10.20-10.23. This represents a significant indication if one considers that the amount of sample loaded inside the column was considerably higher.

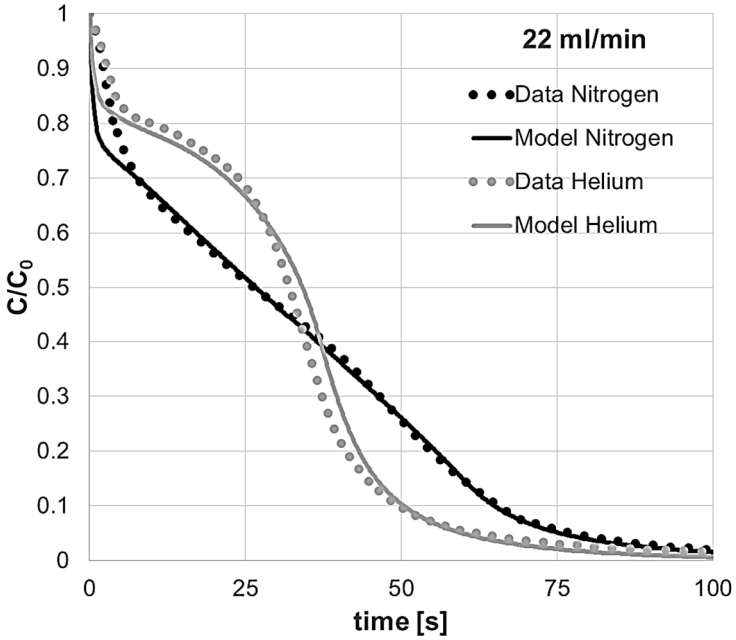

Figure 10.19 – Experimental and predicted response curves for a desorption experiment conducted at 22 ml/min using nitrogen and helium as carrier gas.

Table 10.2 – Values of the parameters used for the simulation of the bed/macroporous diffusion model. These experiments were performed with a better dispersion of the solid inside the column.

	Desorption N_2	**Desorption He**
***L* (highest flowrate)**	$6.31*10^{-4}$	$3.98*10^{-4}$
γ	0.041	0.041
$\beta\ [s^{-1}]$	80	281.6
δ	0.0001	0.0001
geobed	2	2

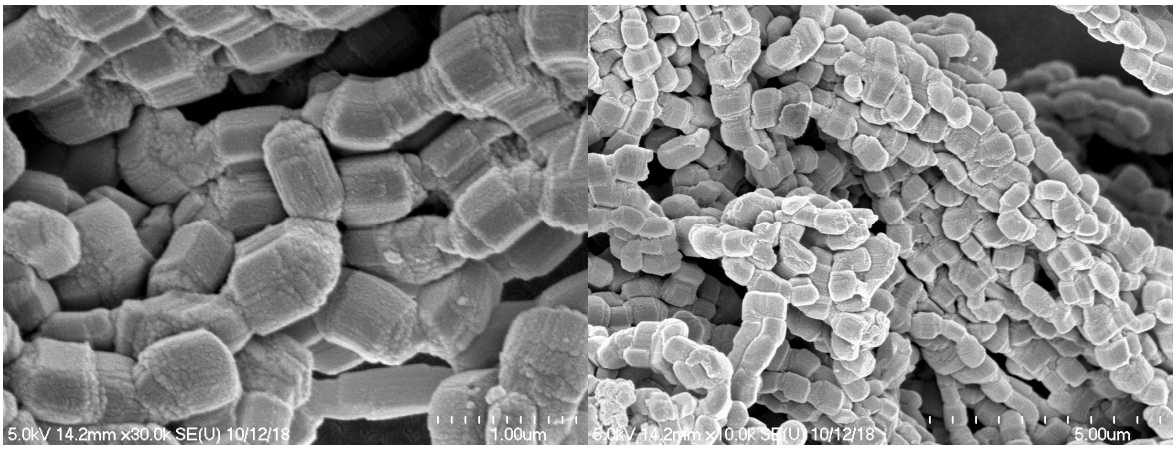

Figure 10.20-21 – SEM pictures on SBA-15 powder.

10.2.3

10.2.3 SBA-15: Heat effects

The energy balance, expressed in section 9.7, was solved using the simulation shown in fig. 10.5. This experiment shows the steepest change of average adsorbed amount with time and therefore it represents the most conservative case for the evaluation of the temperature change of the solid. The temperature change was predicted considering both nitrogen and helium as carrier gas. The equilibrium amount adsorbed and the mass transfer coefficient were considered independent of the temperature. The diameter, external surface area and volume of the solid were estimated as described in section 10.7 and reported in section 10.2.1.

As it is possible to visualize from fig. 10.24, the predicted temperature change is limited 0.65K and 0.15K respectively when using nitrogen and helium as carrier gas. The heat effects are less pronounced with helium due to the higher thermal conductivity of the gas phase. In both simulations, conducted under extremely conservative conditions, the heat effects can be considered negligible and therefore thermal effects can be excluded.

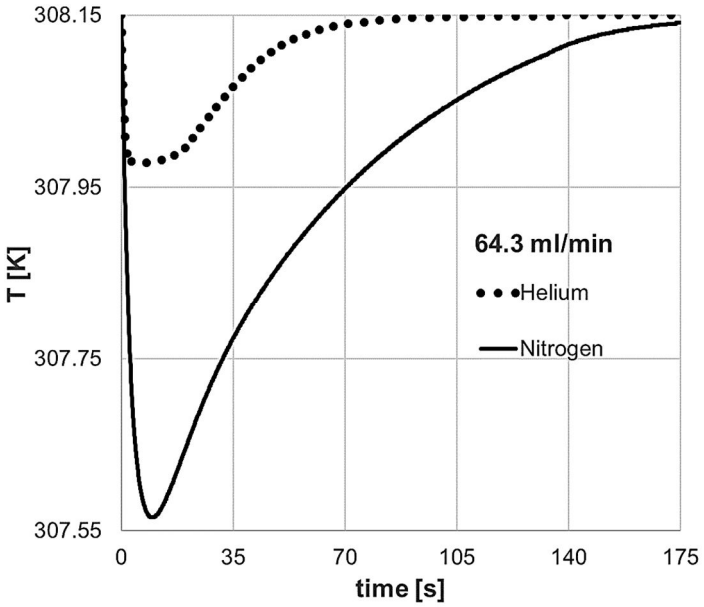

Figure 10.24 – Predicted temperature change of the solid when using nitrogen and helium as carrier gas at the highest desorption flowrate of 34 ml/min.

The values of the parameters used for the simulation of the equivalent linear driving force model and the energy balance are reported in table 10.3.

Table 10.3 – Values of the parameters used for the simulation of the bed/macroporous diffusion model and energy balance in the solid.

	Desorption N_2	**Desorption He**
***L* (highest flowrate)**	0.035	0.01
γ	0.0262	0.0262

$\boldsymbol{\lambda}$	–0.021	–0.021
$\boldsymbol{\sigma}$	0.187	1.001

10.3 Silica-gel

The experimental desorption runs were conducted using a ZLC column packed with 2.6 mg of silica gel beads with an average diameter of 0.165mm. The Ft plot used for the analysis of the control conditions related to the desorption experiments performed at different flowrates is shown in fig. 10.25. The system is under or very close to equilibrium control conditions up to a flowrate of 3.4 ml/min. The water vapour/silica-gel system approaches equilibrium control conditions at higher flowrates when compared to the water vapour/SBA-15 system. This can be spotted from a comparison of the Ft plots given in fig. 10.1 for SBA-15, and in fig. 10.25 for the silica-gel. Therefore, the desorption kinetics of water vapour on silica gel appears to be faster than the desorption kinetics measured on SBA-15. The integration of the experimental desorption signals is shown in fig. 10.26.

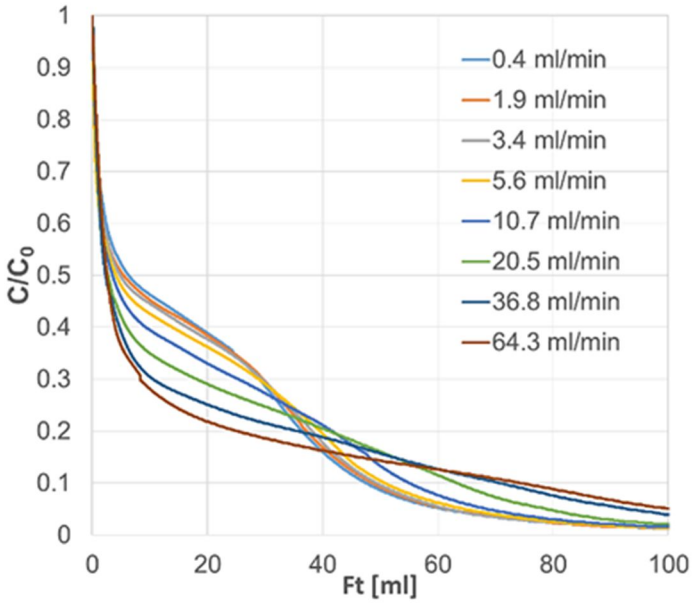

Figure 10.25 – Ft-plot for water vapor on silica gel. Desorption experiments measured at different flowrate at 308K.

As already seen for the integrated SBA-15 desorption curves plotted in fig. 10.3, this representation of the data permits to clearly show the average adsorbed concentration at which the system starts to deviate from equilibrium control condition because of the kinetic limitations. Equally to the SBA-15 scenario, it is possible to observe that the calculated average amount adsorbed starts to diverge from the equilibrium amount adsorbed at the onset of the capillary evaporation, while the highest and the lowest concentrations remain under equilibrium control conditions for longer. When the desorption flowrate is increased, the

difference between the kinetic amount adsorbed and the equilibrium amount adsorbed is enlarged and the kinetic limitations expand up to the lowest concentrations.

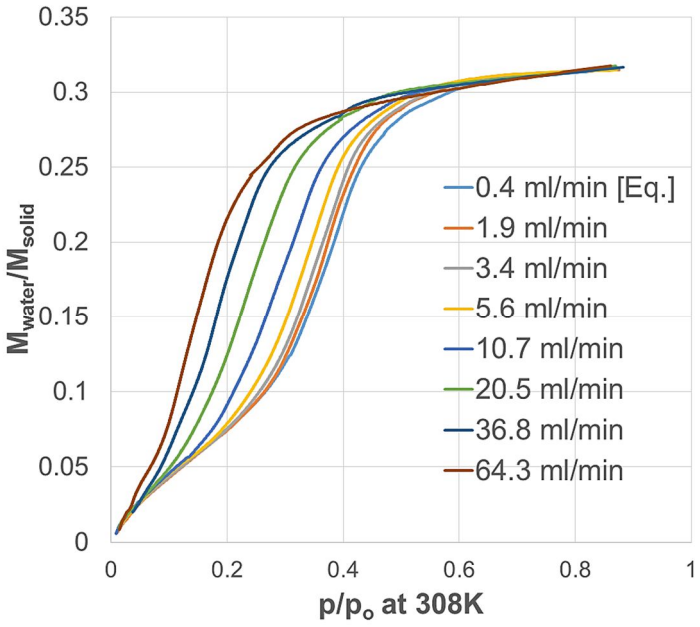

Figure 10.26 – Average amount adsorbed calculated from the different desorption experiments at different flowrate. 0.4 ml/min (equilibrium control conditions) corresponds to the equilibrium desorption isotherm.

10.3.1 Silica-gel: Equivalent linear driving force model

The semi-experimental procedure, applied for SBA-15, was repeated for silica-gel. The aim of this procedure is to assess whether the mass transport mechanism can be well represented by a linear driving force model or not. As discussed already beforehand, the procedure consists in calculating the equivalent linear driving force mass transfer coefficient using the experimental desorption signal and the solution of the mass balance in the ZLC. The final expression for the calculation of the equivalent linear driving force mass transfer coefficient was introduced in section 9.2 as:

$$A_s k_{ldf}(\overline{q_{tot}}) = K_{ldf}(\overline{q_{tot}}) = \frac{V_F \frac{dc_{zlc}}{dt} + F_{out} c_{zlc}}{\overline{q_{tot}} - q_{eq}} \tag{10.4}$$

In fig. 10.27, the calculated k_{ldf} as a function of the average amount adsorbed and for different desorption flowrates is reported. It is interesting to notice that, differently from the SBA-15 case observed previously in fig. 10.4, the k_{ldf} does not show significant variations when changing the desorption flowrate. This aspect can be considered as an indication of the fact that the linear driving force model might represent a good approximation of the mass transport mechanism.

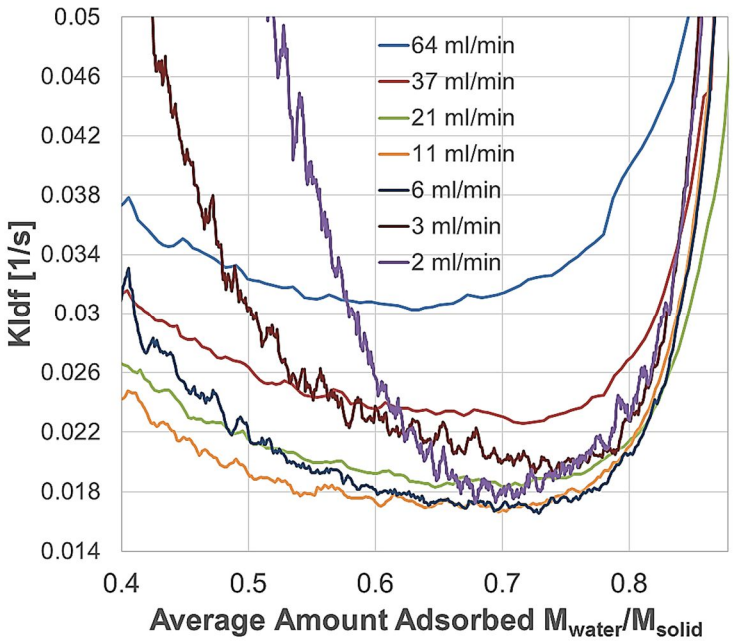

Figure 10.27 – Semi-experimental calculation of the equivalent linear driving force mass transfer coefficients at different flowrates for water vapor on silica gel.

To further investigate this aspect, a rational function was used to best-fit the calculated k_{ldf} as a function of the average amount adsorbed for the highest desorption flowrate. The $k_{ldf}(\bar{Q}_{ave})$ function was then used to simulate the ZLC desorption response curve for all the other flowrates. The simulated desorption response curves at the different flowrates are reported in figs 10.28-10.35. Compared to the SBA-15 scenario shown previously in figs. 10.5-10.10, the prediction of the lower flowrates remains reasonably good. The predictions of the lowest flowrate are very good because the adsorbed concentration is very close to equilibrium and the desorption response curves do not depend on the kinetic model but only on the shape of the isotherm.

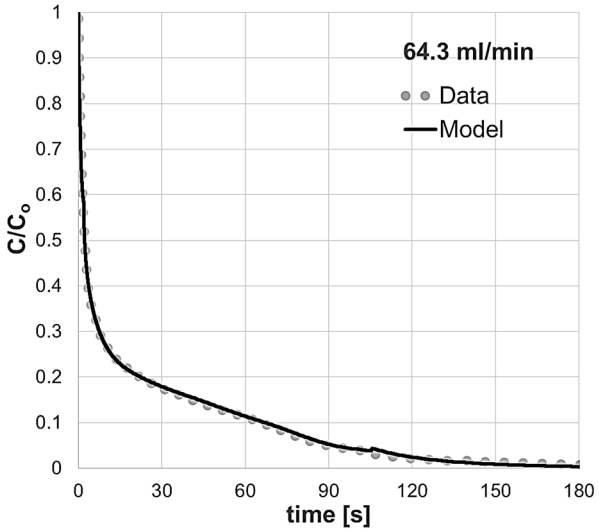

Figure 10.28 – Simulated desorption curve at 64.3 ml/min using the experimental calculated linear driving force coefficient at 64.3 ml/min.

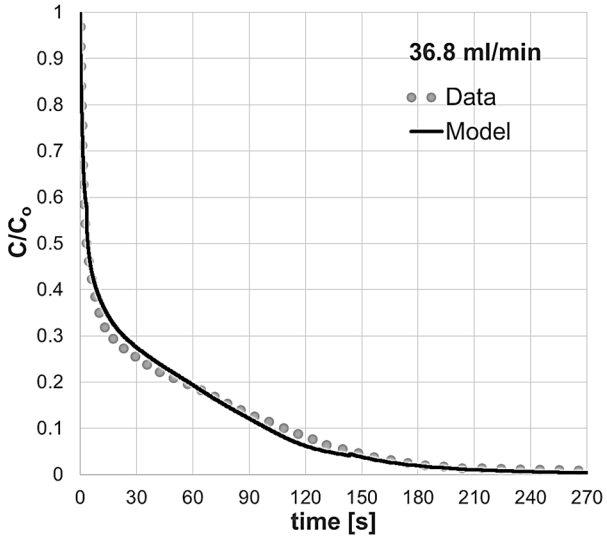

Figure 10.29 – Simulated desorption curve at 36.8 ml/min using the experimental calculated linear driving force coefficient at 64.3 ml/min.

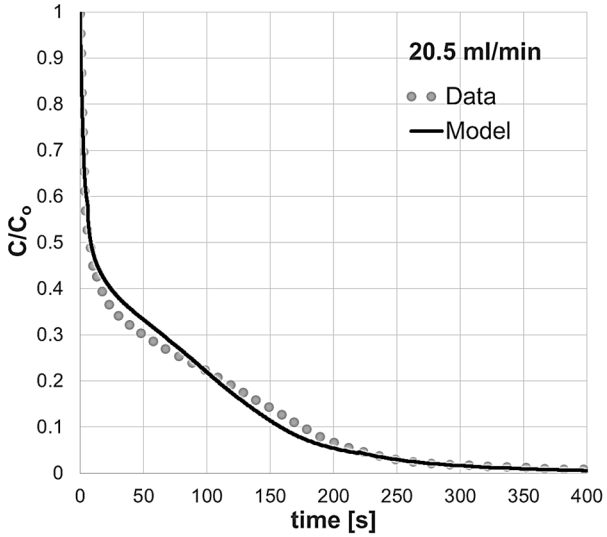

Figure 10.30 – Simulated desorption curve at 20.5 ml/min using the experimental calculated linear driving force coefficient at 64.3 ml/min.

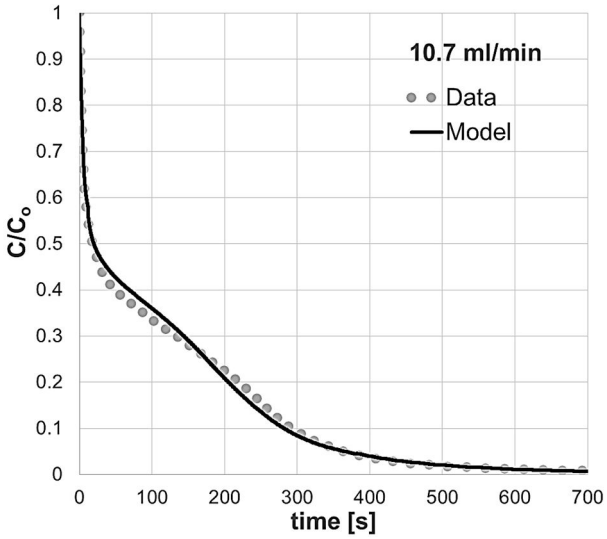

Figure 10.31 – Simulated desorption curve at 10.7 ml/min using the experimental calculated linear driving force coefficient at 64.3 ml/min.

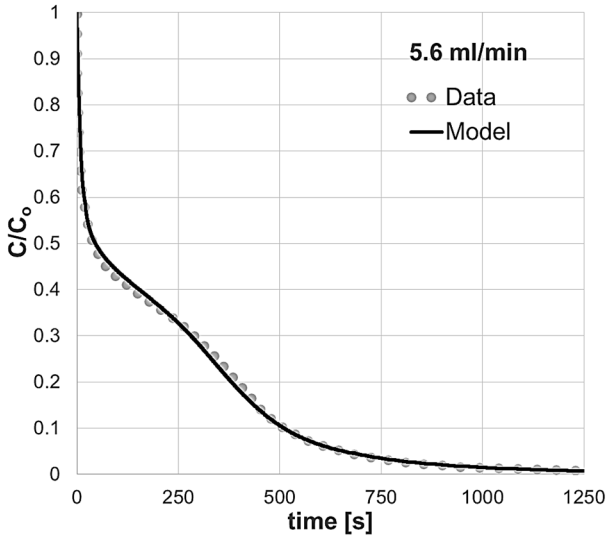

Figure 10.32 – Simulated desorption curve at 5.6 ml/min using the experimental calculated linear driving force coefficient at 64.3 ml/min.

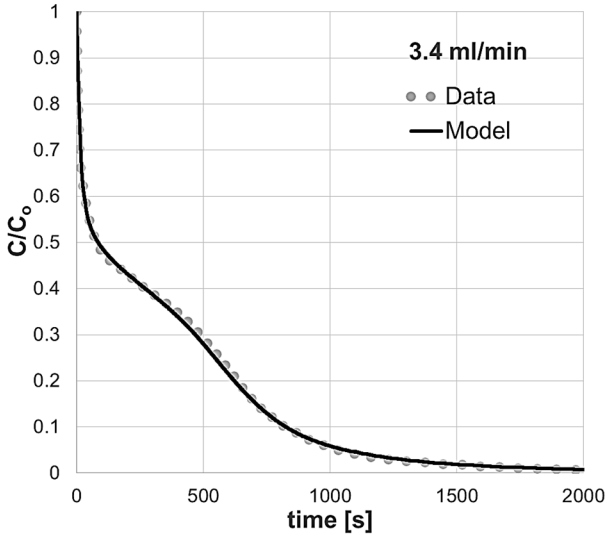

Figure 10.33 – Simulated desorption curve at 3.4 ml/min using the experimental calculated linear driving force coefficient at 64.3 ml/min.

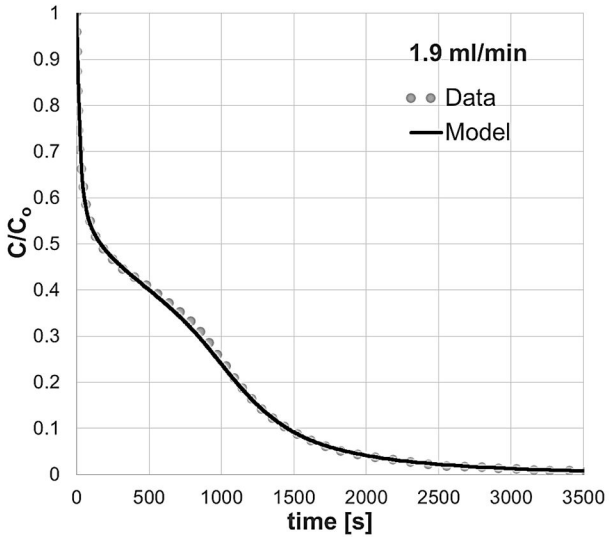

Figure 10.34 – Simulated desorption curve at 1.9 ml/min using the experimental calculated linear driving force coefficient at 64.3 ml/min.

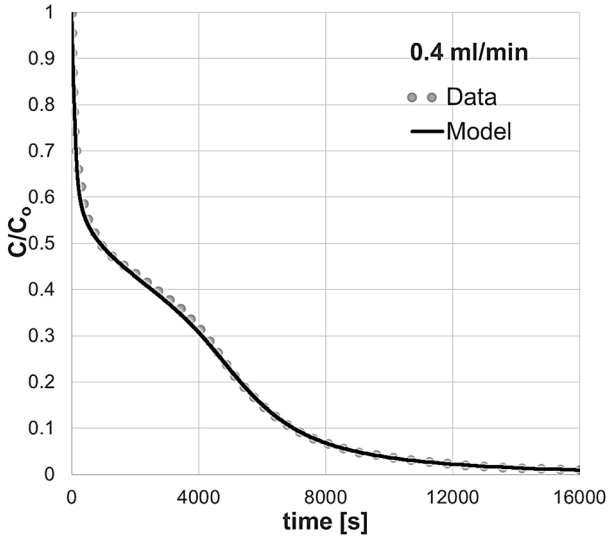

Figure 10.35 – Simulated desorption curve at 0.4 ml/min using the experimental calculated linear driving force coefficient at 64.3 ml/min. The experiment shown represents equilibrium control conditions.

The contribution of the external mass transfer resistance can be estimated as reported in section 9.2. The sample mass used for the kinetics experiment is equal to 2.6 mg. The density of silica is equal to 2.65 gm/cm^3. The diameter, surface area and volume of the hypothetical single crystal are, therefore, easily calculated respectively as 0.616 cm, 0.048 cm^{2,} and 9.79*10^{-4} cm^3. The calculation of the external mass transfer coefficient according to Eq. (9.3b)

$$K_{out} = \frac{Sh\ D_m}{2\ R_p}\frac{A_s}{V_s} = 202\ s^{-1}$$

This value is at least three orders of magnitude larger than the values of K_{ldf} presented in fig. 10.27. Therefore, external contributions to the mass transfer resistance can be considered negligible.

10.3.2 Silica-gel: Linear driving force model and Darken correction factor

Once verified that the linear driving force model can reasonably well represent the mass transport mechanism of desorbing/evaporating water vapor on silica-gel, the aim is to consider a theoretical approach for the prediction of the mass transfer kinetics k_{ldf} for different adsorbed concentrations. The Darken correction factor can be used to correlate the k_{ldf} with the average amount adsorbed and the desorption response curves can be simulated assuming either a linear driving force model or a diffusive model. In this paragraph, the predictions of the linear driving force model are investigated while in the next paragraph a diffusive model will be evaluated.

For the simulation of the ZLC response curves, a system of two ordinary differential equations must be solved. The dimensionless mass balance in the gas phase was already expressed in section 6.2.4 and it can be expressed in dimensionless form as:

$$\frac{d\bar{Q}}{d\tau} + \gamma \frac{dC}{d\tau} = -LC \tag{10.5}$$

While the dimensionless mass balance in the solid phase, considering the introduction of the Darken correction factor is expressed as:

$$\frac{d\bar{Q}}{d\tau} = D_f(Q_{eq} - \bar{Q}) \tag{10.6}$$

Where D_f is the Darken correction factor evaluated at the average amount adsorbed $\bar{Q}$. There is only one fitting parameter for all the desorption experiments and it is given by the linear driving force coefficient at zero concentration k_{ldf_0}, which is included inside the dimensionless time as:

$$\tau = tk_{ldf_0} \tag{10.7}$$

In figs 10.37-10.45, the prediction of the linear driving force model expressed in Eq. (10.3) for the desorption experiments conducted at different flowrate is reported.

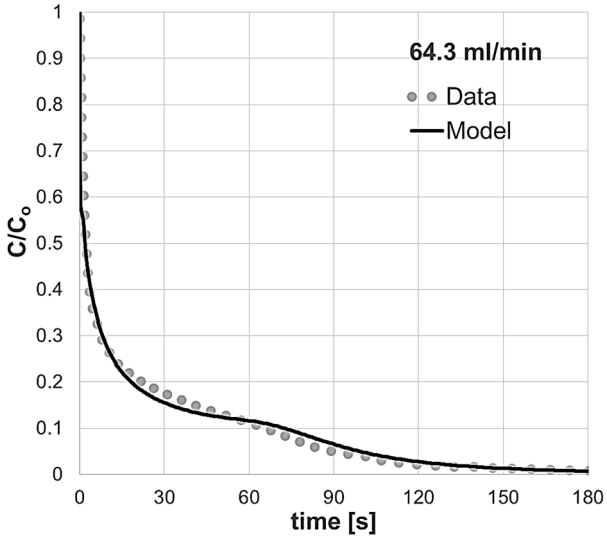

Figure 10.37 – Simulated desorption curve at 64.3 ml/min using the linear driving force model and the Darken correction factor.

The prediction of the linear driving force model, with the use of the Darken correction factor to correlate the k_{ldf} to the average amount adsorbed, provide a good representation of the experimental desorption data at the different flowrates.

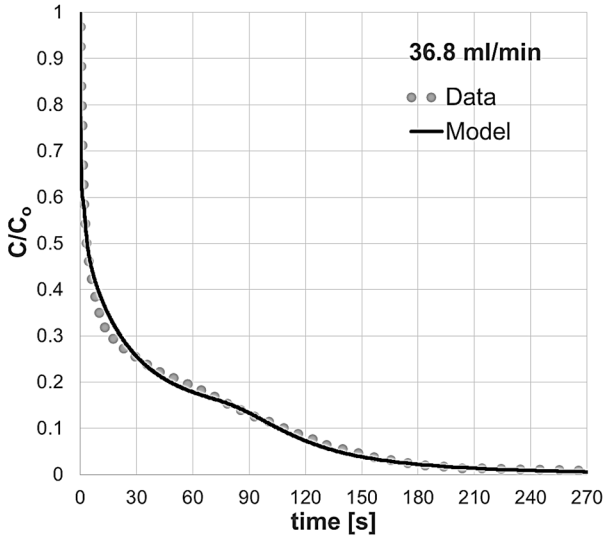

Figure 10.38 – Simulated desorption curve at 36.8 ml/min using the linear driving force model and the Darken correction factor.

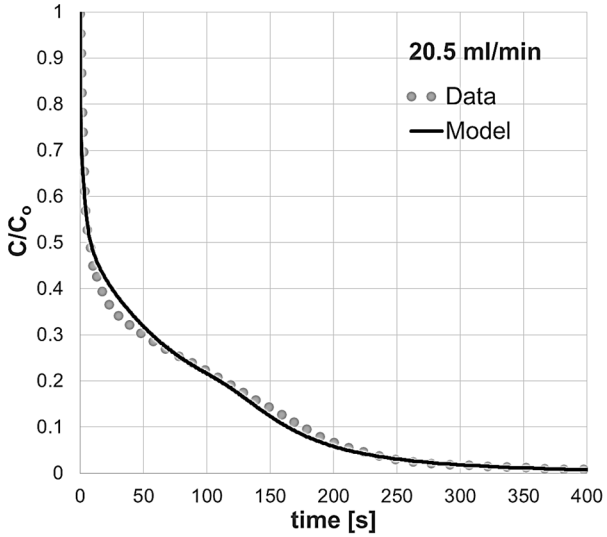

Figure 10.38 – Simulated desorption curve at 20.5 ml/min using the linear driving force model and the Darken correction factor.

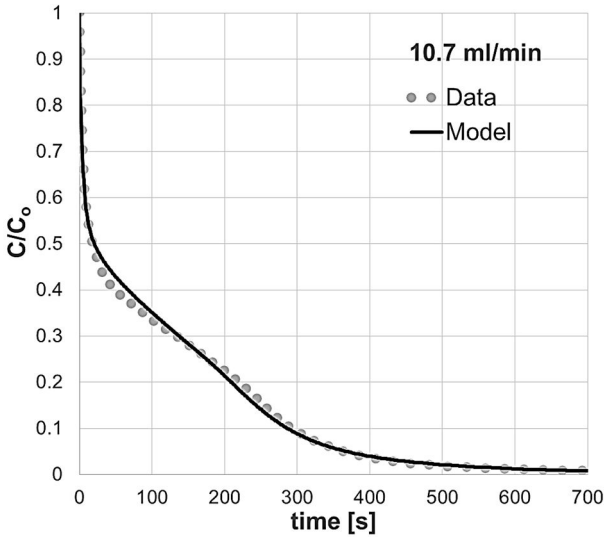

Figure 10.41 – Simulated desorption curve at 10.7 ml/min using the linear driving force model and the Darken correction factor.

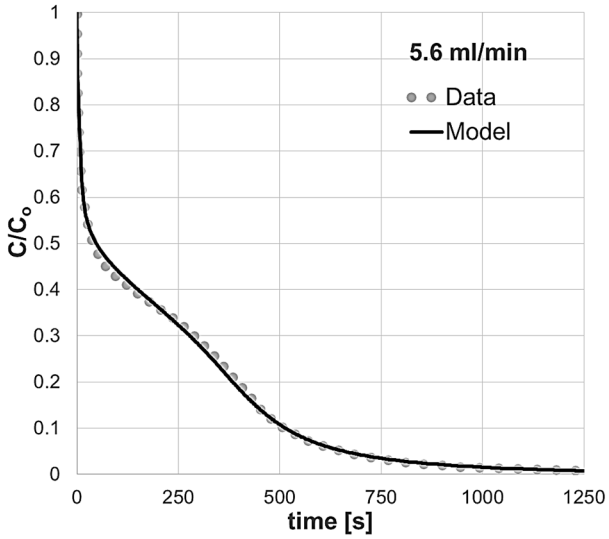

Figure 10.42 – Simulated desorption curve at 5.6 ml/min using the linear driving force model and the Darken correction factor.

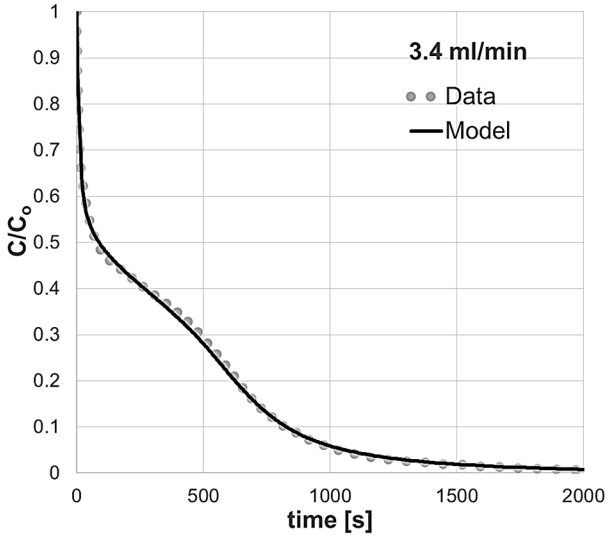

Figure 10.43 – Simulated desorption curve at 3.4 ml/min using the linear driving force model and the Darken correction factor.

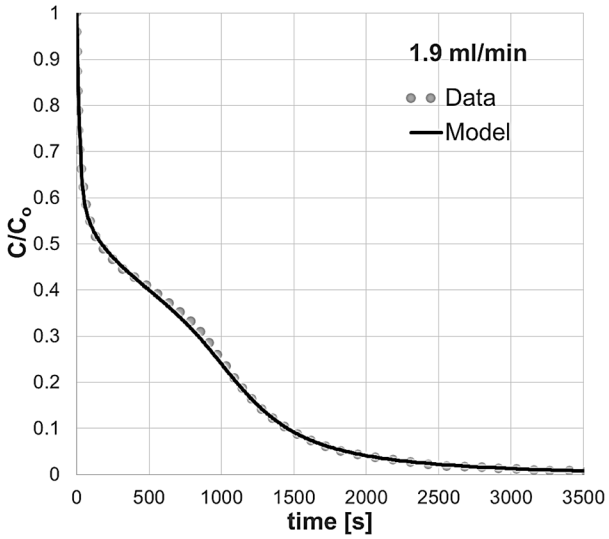

Figure 10.44 – Simulated desorption curve at 1.9 ml/min using the linear driving force model and the Darken correction factor.

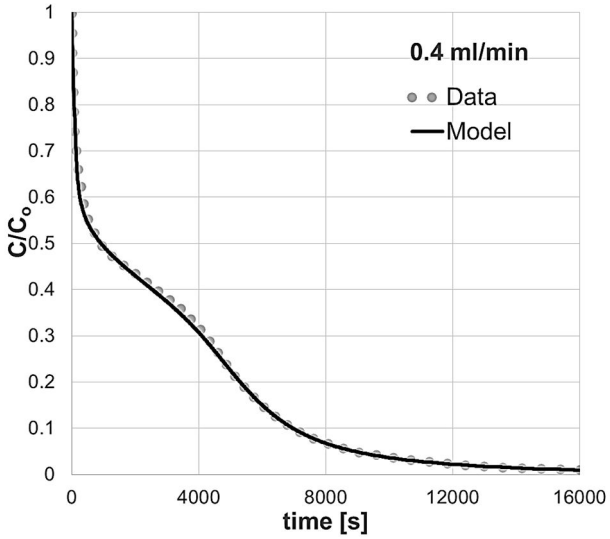

Figure 10.45 – Simulated desorption curve at 0.4 ml/min using the linear driving force model and the Darken correction factor.

The values of the parameters used to simulate the desorption response curves at the different flowrate are reported in table 10.5. The *L* parameter is reported for the highest flowrate. The *L* parameter for the other flowrates is easily computed considering that the parameter is linearly proportional to the flowrate.

Table 10.5 – Values of the parameters used for the solution of the linear driving force model correlated with the Darken correction factor.

	Desorption N_2
***L* (highest flowrate)**	1.17
$\boldsymbol{\gamma}$	0.023
$\boldsymbol{k_{ldf_0}}$ $[\boldsymbol{s^{-1}}]$	0.05

10.3.3 Silica-gel: Bed/Macropores diffusion model

In a scenario in which the mass transfer is controlled by the diffusion in the macropores, the concentration inside the mesopores can be considered constant and at equilibrium with the corresponding concentration along the macropore. The differential mass balance for a bed/macropores controlled diffusion process was expressed in section 9.5 as:

$$\frac{\partial C}{\partial \tau} = \frac{1}{1+\frac{1}{\delta}\frac{\partial Q_{eq}}{\partial C}}\left(\frac{\partial^2 C}{\partial {\xi_b}^2} + \frac{geobed}{\xi_b}\frac{\partial C}{\partial \xi_b}\right) \tag{10.8}$$

The only fitting parameter is given by the inverse of the macropores diffusive time constant which was expressed in section 9.3 as:

$$\beta = \frac{D_m}{{L_{bed}}^2} \tag{10.9}$$

In figs 10.46-10.51, it is possible to observe the prediction of the bed/macropores diffusion model for the different flowrates using two different carrier gas.

The experiments performed with two different carrier gases at the same flowrate showed different experimental response curves which can be near-perfectly predicted by changing the two diffusive time constants according to the different molecular diffusivity of water vapor in the two gases [102]. Nitrogen and helium can be considered as inert in this study and the relevant difference in their molecular weight is helpful for the evaluation of eventual macropores diffusion controlling mechanisms.

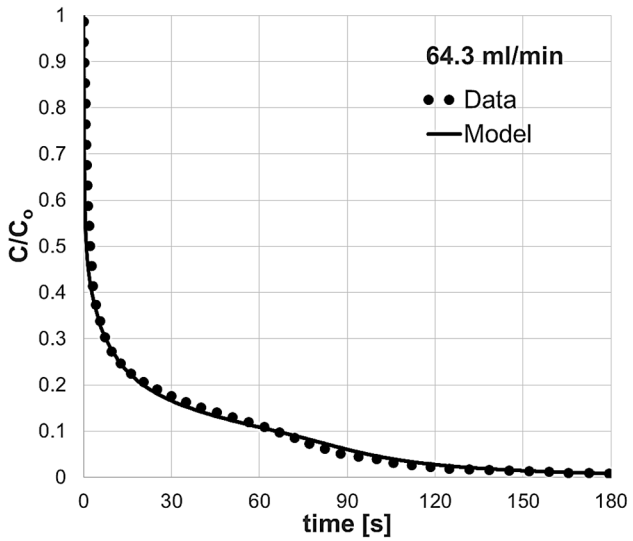

Figure 10.46 – Simulated desorption curve at 64.3 ml/min using the bed/macropores diffusion model.

The experimental desorption curves were measured using different flowrates from kinetic control conditions up to equilibrium control conditions. For the five highest flowrates, the response curves were measured using both carrier gases. The effect of the carrier gas on the shape of the response curve is evident, and this proves the controlling effect operated by the diffusive mass transfer in macroporous channels.

The diffusion model can well predict the response curve for all the flowrates and for both carrier gases. There is only one parameter β to be adjusted for the best correlation of all the experimental curves for both carrier gasses from kinetic up to equilibrium control conditions. All the other dimensionless parameters expressed in the set of differential equations are given by the experimental conditions used and they can be calculated *a priori*.

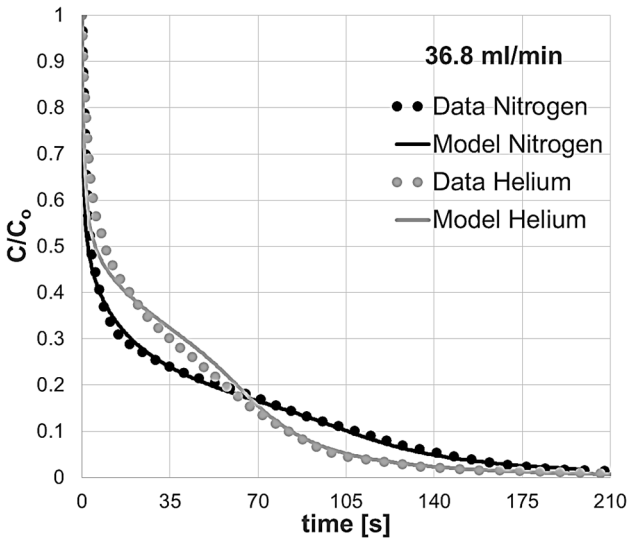

Figure 10.47 – Simulated desorption curve at 36.8 ml/min using the bed/macropores diffusion model

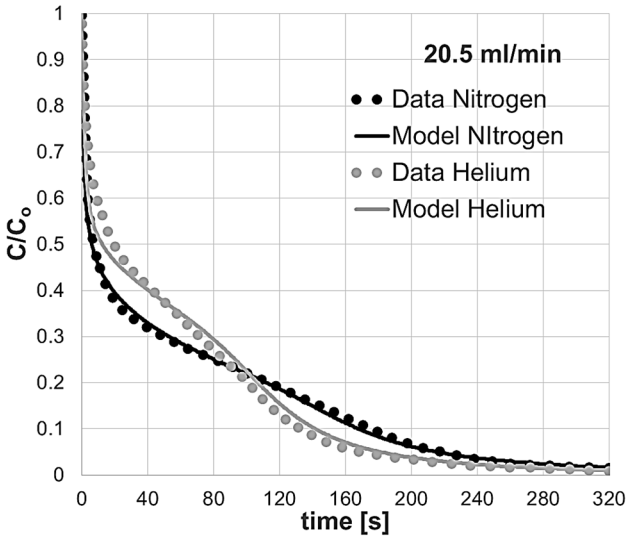

Figure 10.48 – Simulated desorption curve at 20.5 ml/min using the bed/macropores diffusion model.

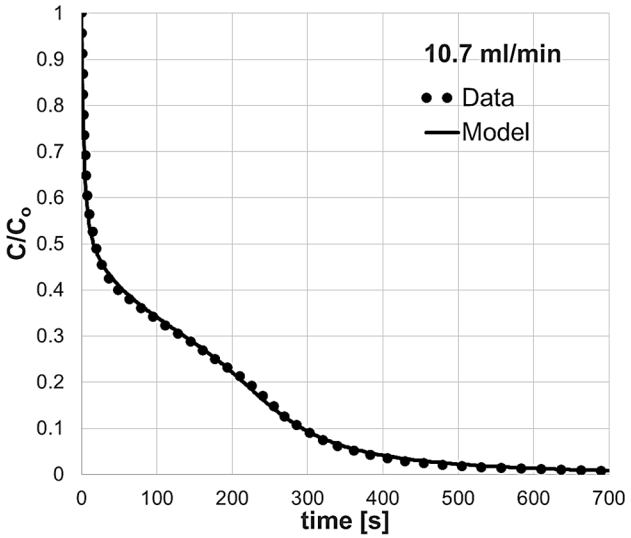

Figure 10.48 – Simulated desorption curve at 20.5 ml/min using the bed/macropores diffusion model.

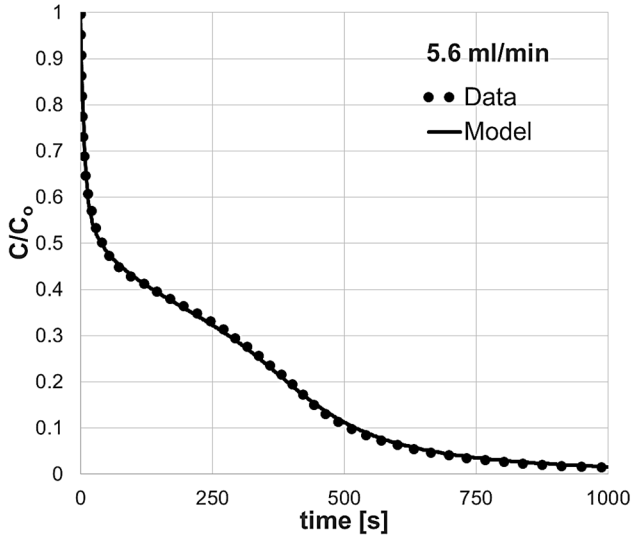

Figure 10.50 – Simulated desorption curve at 5.6 ml/min using the bed/macropores diffusion model.

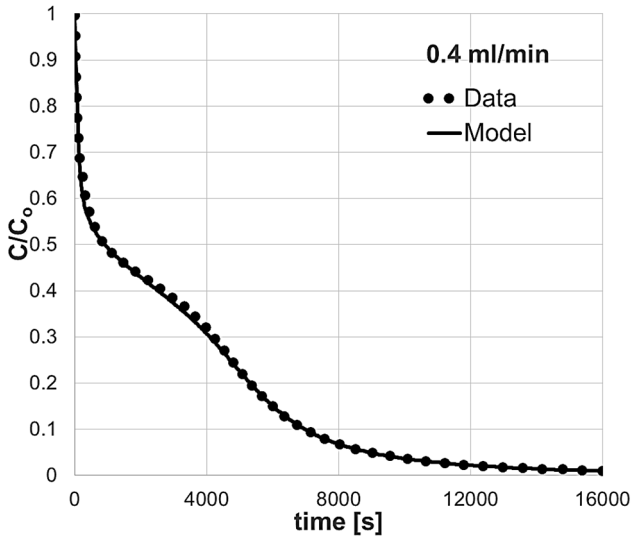

Figure 10.51 – Simulated desorption curve at 0.4 ml/min using the bed/macropores diffusion model.

The values of the parameters used to simulate the desorption response curves at the different flowrate are reported in table 10.6. The *L* parameter is reported for the highest flowrate. The *L* parameter for the other flowrates is easily computed considering that the parameter is linearly proportional to the flowrate.

Table 10.6 – Values of the parameters used for the solution of the solution of bed/macropores diffusion model.

	Desorption N_2	**Desorption He**
***L* (highest flowrate)**	$3.675*10^{-4}$	$6.1*10^{-5}$
$\boldsymbol{\gamma}$	0.023	0.023
$\boldsymbol{\beta}$ $[\mathbf{s^{-1}}]$	160	563.2
$\boldsymbol{\delta}$	0.0001	0.0001
geobed	0	0

Considering that the diffusion coefficient of water vapor in nitrogen is 0.256 cm^2s^{-1} [102] and assuming a tortuosity factor of 2.5 for the bed of silica-gel pellets, the value of the diffusive time constant in the bed corresponds to a diffusive length of 0.253 mm. This value can be reasonable if one considers how silica-gel pellets are packed inside the column.

10.3.4 Silica-gel: Heat effects

The energy balance expressed in section 9.7 was solved using the simulation shown in fig. 10.28. This experiment shows the steepest change of average adsorbed amount with time and therefore it represents the most conservative case for the evaluation of the temperature change of the solid. The temperature change was predicted considering both nitrogen and helium as carrier gas. The equilibrium amount adsorbed and the mass transfer coefficient were considered independent of the temperature. The diameter, external surface area and volume of the solid were estimated as described in section 10.7 and reported in section 10.2.1.
As it is possible to visualize from fig. 10.36, the predicted temperature change is limited 1.5 K and 0.55 K respectively when using nitrogen and helium as carrier gas. The heat effects are less pronounced with helium due to the higher thermal conductivity of the gas phase. In both simulations, conducted under extremely conservative conditions, the heat effects can be considered negligible and therefore thermal effects can be excluded.

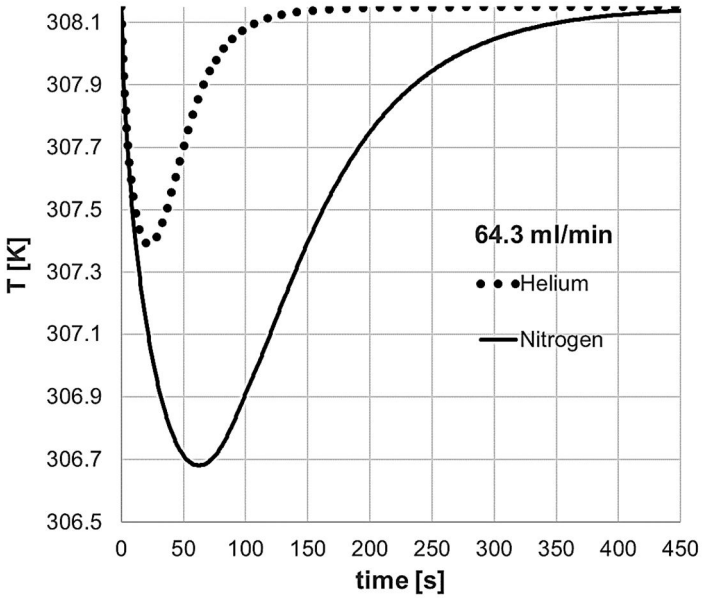

Figure 10.36 – Predicted temperature change of the solid when using nitrogen and helium as carrier gas at the highest desorption flowrate of 64.3 ml/min.

The values of the parameters used for the simulation of the equivalent linear driving force model and the energy balance are reported in table 10.7.

Table 10.7 – Values of the parameters used for the simulation of the equivalent LDF model and energy balance in the solid.

	Desorption N_2	**Desorption He**
***L* (highest flowrate)**	0.059	0.017
γ	0.0234	0.0234
λ	–0.01046	–0.01046
σ	0.0141	0.0755

If the extremely conservative conditions assumed for the evaluation of the thermal effects correspond to the actual experimental conditions, the simulation of the desorption response curve shown in fig. 10.28 can be repeated considering the thermal effects on the equilibrium desorption isotherm and diffusive time constant.

The effect of the temperature on the equilibrium desorption isotherm was shown in section 8.1.4 and can be observed in fig. 8.12. The average difference in the amount adsorbed between two isotherms measured with a temperature difference of 10 K is around 2.6 % in mass. Although the maximum temperature reduction shown in fig. 10.36 is 1.5 K, a conservative assumption of an equilibrium isotherm with a 2.6 % higher adsorbed amount can be made for the new simulation. The effect of the temperature on the time constant can be considered performing a linear interpolation between the values of diffusivity at two different temperatures [102], which results in a decrease of 1.2 % of the diffusivity of water vapor in Nitrogen. The comparison between the response curves simulated at the two different temperatures (fig. 10.36a) confirms the negligible effects of the predicted temperature change and, therefore, permits to exclude any influence of thermal effects on the shape of the response curves shown in figs 10.28-10.35.

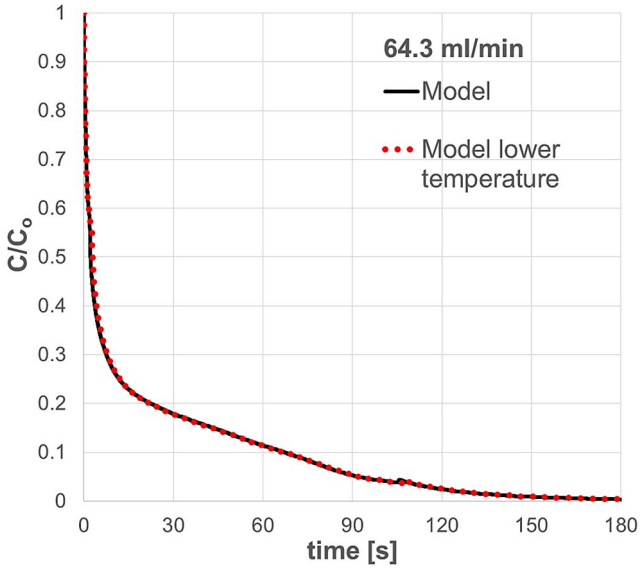

Figure 10.36a – Simulated desorption curve at 64.3 ml/min using the experimental calculated linear driving force coefficient at 64.3 ml/min for two different temperatures. Temperature difference 1.5 K.

10.4 Reproducibility of the ZLC experiments

Figs 10.52-10.53 show two different sets of data measured at different flowrates. The data refer to SBA-15 desorption curves and show the excellent reproducibility of both the equilibrium and kinetic runs.

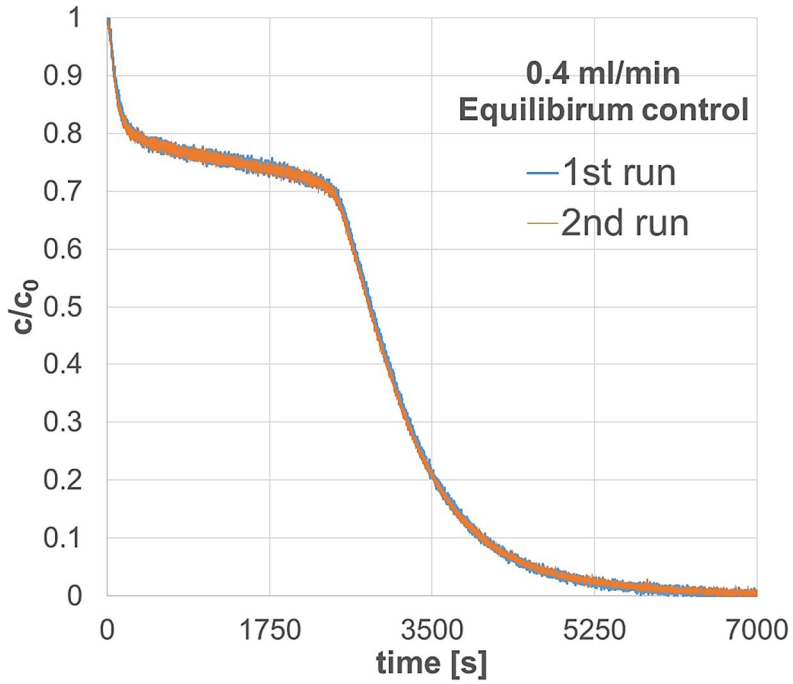

Figure 10.52 – Experimental desorption curves at 0.4 ml/min.

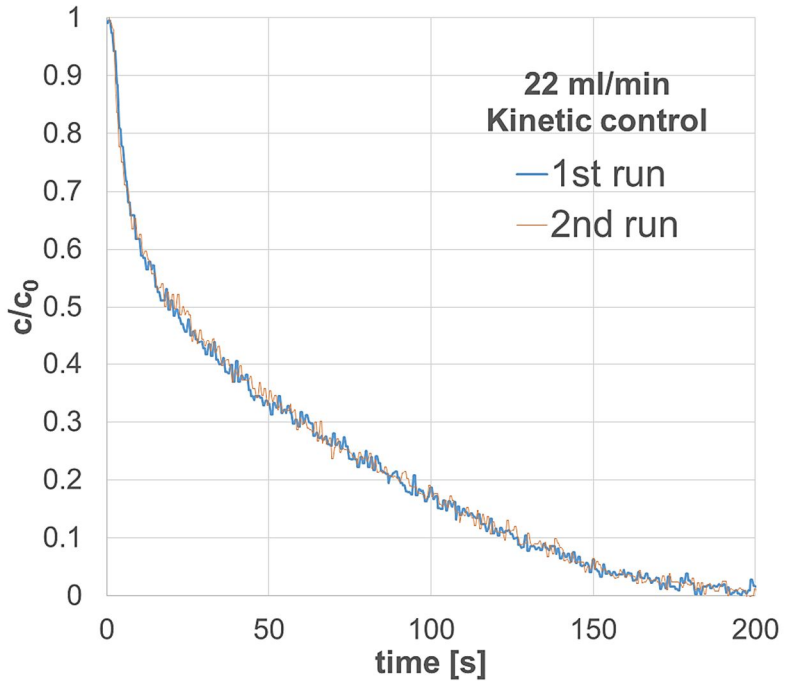

Figure 10.52 – Experimental desorption curves at 22 ml/min.

10.5 Conclusions

The analysis of the desorption response curves obtained with the ZLC technique was carried out to investigate the mass transfer kinetics of condensable water vapor on SBA-15 powder and silica-gel pellets at 308K. Desorption experiments at different flowrates were performed to assess the kinetic control regime of the system. The desorption experiments were carried out throughout the range of adsorbed concentration, from full saturation of the mesopores up to dry solid. Distinct experiments using nitrogen and helium as carrier gas were performed to evaluate the possible influence of the carrier gas on the mass transfer kinetics of water vapor in the two solids. A simple and extremely conservative energy balance on the solid adsorbents was formulated to evaluate the heat effect generated during the desorption process. The heat effects were predicted to be negligible.

A semi-experimental procedure was introduced and adopted for the rapid assessment of the largely used linear driving force model. This model was tested for the correlation of the kinetic experimental data. The LDF model can provide a good correlation for the water vapor experimental data measured on silica-gel. However, the model fails to represent the mass transport mechanism of water vapor in SBA-15. In this case, the equivalent LDF mass transfer coefficient was experimentally found to strongly depend not only on the average amount of adsorbed phase but also on the desorption flowrate. The strong dependence on the flowrate indicates that the LDF model cannot represent the actual mass transfer mechanism for water vapor on SBA-15. ZLC desorption simulations, using the semi-experimental LDF model, were carried out to further prove this concept. The simulations can reasonably well represent the experimental data obtained on silica-gel. On the other hand, the simulations are clearly not able to represent the experimental data obtained on SBA-15.

Several diffusion models were derived to better represent the physical and geometrical characteristics of the adsorption system. The bed/macropores diffusion model was able to correlate the experimental response curves for both solid adsorbents under different control regimes using two different carrier gas. The good correlation of the experimental data proved that the mass transport mechanism of water vapor in both solid adsorbents was controlled by a molecular diffusion process in macroporous channels. For the case of SBA-15, these channels are generated by the agglomeration of the crystals into bigger particles. This leads to the formation of a macroporous bed of SBA-15 particles. As regards silica-gel, the macroporous channels can either be due to the formation of a bed of particles or to the macropores eventually present inside each pellet.

11 Conclusions

In this work, the Zero Length Column (ZLC) technique was used for the first time for the measurement of water vapor adsorption equilibrium and kinetics on mesoporous materials at high relative humidity.

The innovative and unprecedented use of the ZLC technique showed relevant advantages for the measurement of the adsorption equilibrium and kinetic properties when compared to the traditional techniques. The technique was applied to the measurement of water vapor equilibrium and kinetics on two different mesoporous materials as SBA-15 and silica-gel.

The possibility to obtain continuous adsorption-desorption isotherms in a single day represents a significant advantage for rapid and efficient characterization of the solid adsorbents. The ZLC was able to reproduce the same experiments conducted in a commercial gravimetric system in 1/10 of the time taken by the commercial system. The possibility to observe a continuous isotherm represents a significant advantage for the accurate investigation of the pore structure of the solid.

The technique was successfully used for the measurement of type IV isotherms, which are well known for being characterized by complex shapes and a hysteresis loop. The main adsorption-desorption curves of the isotherm and the adsorption-desorption scanning curves inside the hysteresis loop were measured on SBA-15 showing the relevant flexibility of the technique. The capabilities of the technique were also confirmed by the measurement of the main adsorption-desorption curves of the isotherm on silica-gel.

The experimental equilibrium data were correlated using a new analytical equilibrium model for type IV-V isotherms. The model can extraordinarily correlate the experimental data in the entire range of concentration. The model can correlate the main adsorption-desorption branch of the isotherms and the adsorption-desorption scanning curves inside the hysteresis loop. Three formulations of the model were derived for the accurate correlation of the equilibrium data on SBA-15 and silica-gel.

The ZLC was used for the measurement of water vapor adsorption kinetics on SBA-15 powder and silica-gel pellets. Considering the particular structural characteristic of these solid adsorbents, the initial aim was to investigate the mass transport mechanism an adsorbing-condensing vapor inside a well-defined mesoporous channel and inside a mesoporous pore-network. However, the mass transport mechanism of water vapor in both solids was clearly

controlled by the molecular diffusion in macroporous channels. Experiments conducted with two different carrier gas showed the evident influence of a molecular diffusion mechanism on the mass transport of water vapor inside the solid. The different response curves obtained from experiments conducted with different carrier gas can be predicted by simply switching the molecular diffusion coefficient of water vapor in the two carrier gas. For the case of SBA-15, the agglomeration of the crystals inside the column causes the formation of SBA-15 particles which represent the controlling resistance for the mass transfer. For the case of silica-gel, the macroporous channels are either due to the formation of a bed of particles or to the macropores inside the silica-gel pellets.

The ZLC kinetics response was modeled assuming different mechanisms for the mass transport of water vapor inside the solids. A combined diffusion model was derived first and the two subsequent models for bed/macropores diffusion control and mesopore diffusion control were derived as extreme cases of the initial model.

A semi-experimental procedure for the evaluation of the linear driving force model was introduced and adopted for the first time. The procedure provides the equivalent linear driving force coefficient as a function of the average amount adsorbed in the solid. The calculation of such coefficient for different flowrates can assess if the linear driving is a good approximation of the mass transfer mechanism or if more complex models are required. Simulations of the ZLC response curve were carried out using the LDF model to verify the results obtained with the semi-experimental procedure.

As future work, a more efficient procedure for the dispersion of powdery adsorbents can be developed when the measurement of the mass transfer kinetics inside the crystals is needed. The experimental system used in this work is a traditional ZLC system which was upgraded for the adsorption measurements of any condensable vapors up to high relative concentrations of the gas phase. The designing of a dedicated water vapor ZLC system could be thought and developed. The new system would be much more compact and considerably cheaper if compared to the traditional system used in this work. In this scenario, the ZLC system can be considered an efficient and promising technique for the adsorption equilibrium and kinetic measurements of water vapor on any solid adsorbents.

12 Nomenclature

$x_{c_{min}}$	Minimum condensation pressure
$x_{e_{min}}$	Minimum evaporation pressure
ΔH_{ads}	Heat of adsorption (J/mol)
$\Delta H_{condensation}$	Entalphy of condensation (J/mol)
$\Delta H_{first\ layer}$	Enthalpy of adsorption of the first layer (J/mol)
ξ_m	Dimensionless mesopores spatial coordinate
A_s	Solid surface (m^2)
C_{expout}	Normalized exponential function
C_{in}	Forcing function of the detector
C_{norm}	Normalized experimental signal
D_0	Corrected diffusivity (m^2/s)
D_f	Darken correction factor
D_k	Knudsen diffusivity (m^2/s)
D_m	Molecular diffusivity (m^2/s)
D_s	Surface diffusivity (m^2/s)
F_{in}	Inlet flowrate (m^3/s)
F_j	Condensation-evaporation function of the sub-pore j
F_{out}	Outlet flowrate (m^3/s)
$\tilde{G}(s)$	Transfer function in the Laplace domain
$G_{detector}$	Transfer function of the detector in the time domain
K_{ldf}	Linear driving force coefficient (s^{-1})
k_{ldf}	Linear driving force coefficient (m/s)
k'_{ldf}	Linear driving force coefficient (m^3/s)
K_{out}	External mass transfer coefficient (s^{-1})
L_{bed}	Diffusive length of the bed (m)
$L_{fitting}$	Inverse of the washout time of the fitting (s^{-1})
L_m	Length of the mesopores (nm)
L_{meso}	Diffusive length of the mesopores (m)
M_a	Relative amount adsorbed (mg/mg)
M_s	Mass of solid (kg)
N_{max}	Maximum number or allowed adsorbed layers
N_r	Number of pores with radius r
P_{des}	Fraction of empty pores during a desorption process
$\bar{Q}$	Dimensionless average adsorbed concentration
Q^*	Dimensionless equilibrium adsorbed concentration
Q_{eq}	Dimensionless equilibrium concentration
Q_m^*	Dimensionless monolayer adsorbed concentration
Q_s^*	Dimensionless saturation concentration
S_{i-equi}	Equilibrium surface occupied by an adsorbate molecule on the layer i (nm^2)
S_{i-geom}	Geometrical surface occupied by an adsorbate molecule on the layer i (nm^2)
$\bar{T}$	Average temperature of the solid (K)
T_g	Gas phase temperature (K)
V_{cond}	Volume of capillary condensed liquid in the mesopores (nm^3)

V_{diff}	Diffusive volume (m^3)
V_f	Volume of the gas phase in the ZLC (m^3)
V_i	Volume occupied by an adsorbate molecule (nm^3)
V_m	Volume of the first adsorbed layer (nm^3)
V_{meso}	Mesoporous volume (nm^3)
V_{micro}	Microporous volume (nm^3)
V_{mix}	Mixing volume of the fitting (m^3)
V_{ml}	Volume of the adsorbed multilayer phase (nm^3)
V_{mol}	Molar volume (m^2/mol)
V_s	Volume of solid adsorbent (m^3)
V_{s-tot}	Total pore volume of the solid (nm^3)
V_{total}	Total volume of adsorbate in the mesopores (nm^3)
X_{aux}	Solution of the percolation auxiliary equation
c_0	Initial gas phase concentration in the ZLC (mol/m^3)
c_{in}	Inlet concentration of water (mol/m^3)
c_{meso}	Concentration in the gas phase inside the mesopore (mol/m^3)
f_c	Fraction of cavitating pores
f_i	Numerical fraction of the main pore i
f_r	Numerical fraction of pores with radius r
g_j	Numerical fraction of the sub-pore j
k_{ldf}	Linear driving force coefficient (m/s)
m_{dry}	Mass of the dry sample (mg)
m_{dry}	Mass of dry sample on the crucible (mg)
m_s	Mass of the wet sample (mg)
m_s	Mass of sample on the crucible (mg)
m_{sat}	Saturation capacity of the solid (mg/mg)
$m_{s-micro}$	Saturation capacity of the micropores (mg/mg)
m_{solid}	Mass of sample packed in the ZLC (Kg)
n_{max}	Maximum number or adsorbed layers
p_0	Saturation pressure of water (Pa)
p_0	Saturation pressure of water vapour (Pa)
p_{ads}	Fraction of pores allowed to empty in an adsorption process
p_{des}	Fraction of pores allowed to empty in a desorption process
$\bar{q}$	Average concentration of adsorbate in the solid (mol/m^3)
q_0	Initial adsorbed phase concentration in the solid (mol/m^3)
q_{eq}	Equilibrium adsorbate concentration in the solid (mol/m^3)
r_c	Radius condensation function (nm)
r_e	Radius evaporation function (nm)
r_m	Radius of curvature of the meniscus (m)
r_{max}	Maximum radius of the pore size distribution (nm)
r_{min}	Minimum radius of the pore size distribution (nm)
v_i	Specific volume of an adsorbate molecule on the layer i (nm^3/ nm^2)
x_{0ads}	Starting concentration of an adsorption scanning curve
x_{0des}	Starting concentration of a desorption scanning curve
y_0	Initial molar fraction of water in the column
y_{in}	Molar fraction of water in the inlet stream

$\alpha_{fitting}$	Inverse of the time constant of the diffusive volume (s^{-1})
β_{BET}	BET dimensionless parameter
$\beta_{Langmuir}$	Langmuir dimensionless parameter
$\gamma_{fitting}$	Relative accumulation parameter of the fitting
γ_s	Surface tension (J/ m^2)
ε_{meso}	Mesopores voidage
θ_s	Dimensionless temperature of the solid
ξ_b	Dimensionless bed spatial coordinate
ρ_0	Liquid bulk density (kg/m^3)
ρ_r	Relative density of the capillary condensed liquid
h	Gas phase heat transfer coefficient (W/m^2 K)
C	Equilibrium constant of the BET model
C	Dimensionless gas phase concentration
Cp	Heat capacity of the solid (J/K kg)
D	Gas phase or adsorbed phase diffusivity (m^2/s)
J	Anderson surface reduction coefficient
K	Langmuir equilibrium constant (Pa^{-1})
K	Henry law constant
L	Control conditions parameter ZLC
N	Number of mesopores
N	Number of sub-pore inside each main pore
R	Gas constant (J/mol K)
X	Diffusive length of the fitting (m)
a	Inverse of the time constant of the mixing volume (s^{-1})
c	Outlet concentration of water (mol/m^3)
d	Thickness of a single adsorbed layer (nm)
dA	Adsorbate differential surface
dV	Adsorbate differential volume
g	Equilibrium constant for the last adsorbed layer of the BET model
$geobed$	Bed geometrical factor
$geomeso$	Mesopore geometrical factor
n	Number of main pores
p	Partial pressure of water vapour (Pa)
r	Radius of mesopore (nm)
t	Thickness of the multilayer phase (nm)
$timeEXP$	Time at which the exponential integration begins (s)
x	Relative humidity
z	Coordination number of the lattice
α	Inverse of the diffusive time constant in the solid (s^{-1})
β	Inverse of the diffusive time constant in the bed of particles (s^{-1})
γ	Relative accumulation parameter of the ZLC
δ	Relative accumulation parameter in the solid
ε	Bed voidage
θ	Contact angle between the solid and liquid surface (degree)
κ	Isothermal compressibility of the capillary condensed liquid (Pa^{-1})
μ	Mean of the log-normal or normal distribution

ρ	Capillary condensed liquid density (Kg/m^3)
σ	Dispersion of the log-normal or normal distribution
τ	Dimensionless time

13 References

[1] F.C. Krebs, Carbon dioxide—a themed issue, Energy Environ. Sci. 5 (2012) 7238. doi:10.1039/c2ee90018a.

[2] N. MacDowell, N. Florin, A. Buchard, J. Hallett, A. Galindo, G. Jackson, C.S. Adjiman, C.K. Williams, N. Shah, P. Fennell, An overview of CO2 capture technologies, Energy Environ. Sci. 3 (2010) 1645. doi:10.1039/c004106h.

[3] M.E. Boot-Handford, J.C. Abanades, E.J. Anthony, M.J. Blunt, S. Brandani, N. Mac Dowell, J.R. Fernández, M.-C. Ferrari, R. Gross, J.P. Hallett, R.S. Haszeldine, P. Heptonstall, A. Lyngfelt, Z. Makuch, E. Mangano, R.T.J. Porter, M. Pourkashanian, G.T. Rochelle, N. Shah, J.G. Yao, P.S. Fennell, Carbon capture and storage update, Energy Environ. Sci. 7 (2014) 130–189. doi:10.1039/C3EE42350F.

[4] H.A.A. Farag, M.M. Ezzat, H. Amer, A.W. Nashed, Natural gas dehydration by desiccant materials, Alexandria Eng. J. 50 (2011) 431–439. doi:10.1016/j.aej.2011.01.020.

[5] Ruzhu Wang; Liwei Wang; Jingyi Wu, Adsorption Refrigeration Technology: Theory and Application, Copyright © 2014 John Wiley & Sons, Singapore Pte. Ltd., Singapore, 2014. doi:10.1002/9781118197448.

[6] M. Thommes, J. Morell, K.A. Cychosz, M. Fröba, Combining nitrogen, argon, and water adsorption for advanced characterization of ordered mesoporous carbons (CMKs) and periodic mesoporous organosilicas (PMOs), Langmuir. 29 (2013) 14893–14902. doi:10.1021/la402832b.

[7] L. Sarkisov, A. Centineo, S. Brandani, Molecular simulation and experiments of water adsorption in a high surface area activated carbon: Hysteresis, scanning curves and spatial organization of water clusters, Carbon N. Y. 118 (2017) 127–138. doi:10.1016/j.carbon.2017.03.044.

[8] J.F. Young, Humidity control in the laboratory using salt solutions—a review, J. Appl. Chem. 17 (2007) 241–245. doi:doi:10.1002/jctb.5010170901.

[9] H.F. G., Principles of adsorption & adsorption processes, by D. M. Ruthven, John Wiley & Sons, 1984, xxiv + 433 pp, AIChE J. 31 (2018) 523–524. doi:10.1002/aic.690310335.

[10] M. Eic, D.M. Ruthven, A new experimental technique for measurement of intracrystalline diffusivity, Zeolites. 8 (1988) 40–45. doi:10.1016/S0144-2449(88)80028-9.

[11] F. Brandani, D. Ruthven, C.G. Coe, Measurement of adsorption equilibrium by the zero length column (ZLC) technique part 1: Single-component systems, Ind. Eng. Chem. Res. 42 (2003) 1451–1461. doi:10.1021/ie020572n.

[12] F. Brandani, D. Ruthven, C.G. Coe, Measurement of adsorption equilibrium by the zero length column (ZLC) technique part 1: Single-component systems, Ind. Eng. Chem. Res. 42 (2003) 1451–1461. doi:10.1021/ie020572n.

[13] G. Zhao, Z. Zhao, J. Wu, D. Ye, Synthesis of hydrophobic mesoporous material MFS and its adsorption properties of water vapor, J. Spectrosc. 2014 (2014).

doi:10.1155/2014/965037.

[14] V. Chaudhary, S. Sharma, An overview of ordered mesoporous material SBA-15: synthesis, functionalization and application in oxidation reactions, J. Porous Mater. 24 (2017) 741–749. doi:10.1007/s10934-016-0311-z.

[15] N. Rahmat, A.Z. Abdullah, A.R. Mohamed, A Review : Mesoporous Santa Barbara Amorphous-15 , Types , Synthesis and Its Applications towards Biorefinery Production Norhasyimi Rahmat , 2 Ahmad Zuhairi Abdullah , 2 Abdul Rahman Mohamed Faculty of Chemical Engineering , University Technology MARA , S, Am. J. Appl. Sci. 7 (2010) 1579–1586. doi:10.3844/ajassp.2010.1579.1586.

[16] T. Yanagisawa, T. Shimizu, K. Kuroda, C. Kato, The preparation of alkyltrimethylammonium-kanemite complexes and their conversion to microporous materials, Bull. Chem. Soc. Jpn. 63 (1990) 988–992. doi:10.1246/bcsj.63.988.

[17] M. Ferdousi, M. Pazouki, F.A. Hessari, M. Kazemzad, Simultaneous control of rod length and pore diameter of SBA-15 for PPL loading, J. Porous Mater. 23 (2016) 453–463. doi:10.1007/s10934-015-0099-2.

[18] A. Galarneau, M. Nader, G. Flavien, F. Di Renzo, A. Gedeon, Understanding the stability in water of mesoporous SBA-15 and MCM-41, J. Phys. Chem. C. 111 (2007) 8268–8277. doi:10.1021/jp068526e.

[19] R.A. Pollock, G.Y. Gor, B.R. Walsh, J. Fry, I.T. Ghampson, Y.B. Melnichenko, H. Kaiser, W.J. Desisto, M.C. Wheeler, B.G. Frederick, Role of liquid vs vapor water in the hydrothermal degradation of SBA-15, J. Phys. Chem. C. 116 (2012) 22802–22814. doi:10.1021/jp303150e.

[20] B. Grünberg, T. Emmler, E. Gedat, I. Shenderovich, G.H. Findenegg, H.H. Limbach, G. Buntkowsky, Hydrogen bonding of water confined in mesoporous silica MCM-41 and SBA-15 studied by 1H solid-state NMR, Chem. - A Eur. J. 10 (2004) 5689–5696. doi:10.1002/chem.200400351.

[21] B. Gouze, J. Cambedouzou, S. Parrès-Maynadié, D. Rébiscoul, How hexagonal mesoporous silica evolves in water on short and long term: Role of pore size and silica wall porosity, Microporous Mesoporous Mater. 183 (2014) 168–176. doi:10.1016/j.micromeso.2013.08.041.

[22] M. Erko, D. Wallacher, G.H. Findenegg, O. Paris, Repeated sorption of water in SBA-15 investigated by means of insitu small-angle x-ray scattering, J. Phys. Condens. Matter. 24 (2012). doi:10.1088/0953-8984/24/28/284112.

[23] V.M. Gun'ko, V. V. Turov, A. V. Turov, V.I. Zarko, V.I. Gerda, V. V. Yanishpolskii, I.S. Berezovska, V.A. Tertykh, Behaviour of pure water and water mixture with benzene or chloroform adsorbed onto ordered mesoporous silicas, Cent. Eur. J. Chem. 5 (2007) 420–454. doi:10.2478/s11532-007-0010-3.

[24] J. Pires, M. Pinto, J. Estella, J.C. Echeverría, Characterization of the hydrophobicity of mesoporous silicas and clays with silica pillars by water adsorption and DRIFT, J. Colloid Interface Sci. 317 (2008) 206–213. doi:10.1016/j.jcis.2007.09.035.

[25] Z. L.T., The surface chemistry of amorphous silica, Zhuravlev Model. Colloids Surfaces A. 173 (2000) 1.

[26] C. Pirez, J.C. Morin, J.C. Manayil, A.F. Lee, K. Wilson, Sol-gel synthesis of SBA-15:

Impact of HCl on surface chemistry, Microporous Mesoporous Mater. 271 (2018) 196–202. doi:10.1016/j.micromeso.2018.05.043.

[27] M. Kruk, M. Jaroniec, C.H. Ko, R. Ryoo, Characterization of the porous structure of SBA-15, Chem. Mater. 12 (2000) 1961–1968. doi:10.1021/cm000164e.

[28] S. Maaz, M. Rose, R. Palkovits, Systematic investigation of the pore structure and surface properties of SBA-15 by water vapor physisorption, Microporous Mesoporous Mater. 220 (2016) 183–187. doi:10.1016/j.micromeso.2015.09.005.

[29] W.S. Chiang, E. Fratini, P. Baglioni, D. Georgi, J.H. Chen, Y. Liu, Methane Adsorption in Model Mesoporous Material, SBA-15, Studied by Small-Angle Neutron Scattering, J. Phys. Chem. C. 120 (2016) 4354–4363. doi:10.1021/acs.jpcc.5b10688.

[30] P.A. Monson, Understanding adsorption/desorption hysteresis for fluids in mesoporous materials using simple molecular models and classical density functional theory, Microporous Mesoporous Mater. 160 (2012) 47–66. doi:10.1016/j.micromeso.2012.04.043.

[31] S. Brandani, D.M. Ruthven, Analysis of ZLC desorption curves for gaseous systems, Adsorption. 2 (1996) 133–143. doi:10.1007/BF00127043.

[32] S. Brandani, Effects of nonlinear equilibrium on zero length column experiments, Chem. Eng. Sci. 53 (1998) 2791–2798. doi:10.1016/S0009-2509(98)00075-X.

[33] S. Brandani, M.A. Jama, D.M. Ruthven, ZLC measurements under non-linear conditions, Chem. Eng. Sci. 55 (2000) 1205–1212. doi:10.1016/S0009-2509(99)00411-X.

[34] S. Brandani, Analytical solution for ZLC desorption curves with bi-porous adsorbent particles, Chem. Eng. Sci. 51 (1996) 3283–3288. doi:10.1016/0009-2509(95)00399-1.

[35] W.L. Duncan, K.P. Moller, The effect of a crystal size distribution on ZLC experiments, Chem. Eng. Sci. 57 (2002) 2641–2652. doi:10.1016/S0009-2509(02)00161-6.

[36] S. Brandani, On the chromatographic measurement of equilibrium isotherms using large concentration steps, Adsorption. 11 (2005) 231–235. doi:10.1007/s10450-005-5929-0.

[37] H. Wang, S. Brandani, G. Lin, X. Hu, Flowrate correction for the determination of isotherms and Darken thermodynamic factors from Zero Length Column (ZLC) experiments, Adsorption. 17 (2011) 687–694. doi:10.1007/s10450-011-9364-0.

[38] E. Mangano, S. Brandani, D.M. Ruthven, Analysis and interpretation of zero length column response curves, Chemie-Ingenieur-Technik. 85 (2013) 1714–1718. doi:10.1002/cite.201300083.

[39] S. Brandani, A Simple Graphical Check of Consistency for Zero Length Column Desorption Curves, Chem. Eng. Technol. 39 (2016) 1194–1198. doi:10.1002/ceat.201500634.

[40] F. Brandani, D. Ruthven, Measurement of Adsorption Equilibria by the Zero Length Column (ZLC) Technique Part 2: Binary Systems, Ind. Eng. Chem. Res. 42 (2003) 1462–1469. doi:10.1021/ie020573f.

[41] D. Friedrich, E. Mangano, S. Brandani, Automatic estimation of kinetic and isotherm parameters from ZLC experiments, Chem. Eng. Sci. 126 (2015) 616–624. doi:10.1016/j.ces.2014.12.062.

[42] S. Brandani, Analysis of the piezometric method for the study of diffusion in microporous solids: Isothermal case, Adsorption. 4 (1998) 17–24. doi:10.1023/A:1008831202564.

[43] M. Thommes, K. Kaneko, A. V. Neimark, J.P. Olivier, F. Rodriguez-Reinoso, J. Rouquerol, K.S.W. Sing, Physisorption of gases, with special reference to the evaluation of surface area and pore size distribution (IUPAC Technical Report), Pure Appl. Chem. 87 (2015) 1051–1069. doi:10.1515/pac-2014-1117.

[44] K.A. Cychosz, R. Guillet-Nicolas, J. García-Martínez, M. Thommes, Recent advances in the textural characterization of hierarchically structured nanoporous materials, Chem. Soc. Rev. 46 (2017) 389–414. doi:10.1039/c6cs00391e.

[45] J. Landers, G.Y. Gor, A. V. Neimark, Density functional theory methods for characterization of porous materials, Colloids Surfaces A Physicochem. Eng. Asp. 437 (2013) 3–32. doi:10.1016/j.colsurfa.2013.01.007.

[46] S. Brunauer, l. S. Deming, W.E. Deming, E. Teller, July, 1940 THEORY, J. Am. Chem. Soc. 62 (1940) 1723–1732. doi:10.1021/ja01864a025.

[47] D.H. Everett, W.I. Whitton, A general approach to hysteresis, Trans. Faraday Soc. 48 (1952) 749–757. doi:10.1039/tf9524800749.

[48] G.A. Tompsett, L. Krogh, D.W. Griffin, W.C. Conner, Hysteresis and scanning behavior of mesoporous molecular sieves, Langmuir. 21 (2005) 8214–8225. doi:10.1021/la050068y.

[49] R. Cimino, K.A. Cychosz, M. Thommes, A. V. Neimark, Experimental and theoretical studies of scanning adsorption-desorption isotherms, Colloids Surfaces A Physicochem. Eng. Asp. 437 (2013) 76–89. doi:10.1016/j.colsurfa.2013.03.025.

[50] K. Morishige, Dependent Domain Model of Cylindrical Pores, J. Phys. Chem. C. 121 (2017) 5099–5107. doi:10.1021/acs.jpcc.6b12566.

[51] A.H. Wootters, R.B. Hallock, Hysteretic Behavior of Superfluid Helium in Anopore, J. Low Temp. Phys. 121 (2000) 549–554. doi:10.1023/A:1017599024229.

[52] B. Coasne, K.E. Gubbins, R.J.M. Pellenq, Domain theory for capillary condensation hysteresis, Phys. Rev. B - Condens. Matter Mater. Phys. 72 (2005) 1–9. doi:10.1103/PhysRevB.72.024304.

[53] D.H. Everett, F.S. Stone, The Structure and properties of porous materials; proceedings of the tenth symposium of the Colston Research Society held in the University of Bristol, March 24th-March 27th, 1958. Edited by D.H. Everett and F.S. Stone., in: Butterworths Scientific Publications, London, 1958.

[54] X.J. Liu, Y.F. Shi, M.A. Kalbassi, R. Underwood, Y.S. Liu, A comprehensive description of water vapor equilibriums on alumina F-200: Adsorption, desorption, and H2O/CO2binary adsorption, Sep. Purif. Technol. 133 (2014) 276–281. doi:10.1016/j.seppur.2014.06.052.

[55] S. Sircar, Capillary condensation theory for adsorption of vapors on mesoporous

solids, Surf. Sci. 164 (1985) 393–402. doi:https://doi.org/10.1016/0039-6028(85)90754-X.

[56] D.D. Do, H.D. Do, A Model for water adsorption in activated carbon, 38 (2015) 767–773. doi:10.1016/S0008-6223(99)00159-1.

[57] J.S. Oh, W.G. Shim, J.W. Lee, J.H. Kim, H. Moon, G. Seo, Adsorption Equilibrium of Water Vapor on Mesoporous Materials, J. Chem. Eng. Data. 48 (2003) 1458–1462. doi:10.1021/je0301390.

[58] P. Rajniak, R.T. Yang, A Simple Model and Experiments for Adsorption- Desorption Hysteresis : Water Vapor on Silica Gel, 39 (1993).

[59] S. Brunauer, L.S. Deming, W.E. Deming, E. Teller, On a Theory of the van der Waals Adsorption of Gases, J. Am. Chem. Soc. 62 (1940) 1723–1732. doi:10.1021/ja01864a025.

[60] P. Rajniak, R.T. Yang, A simple model and experiments for adsorption-desorption hysteresis: Water vapor on silica gel, AIChE J. 39 (1993) 774–786. doi:10.1002/aic.690390506.

[61] J.D. Moore, A. Serbezov, Correlation of adsorption equilibrium data for water vapor on F-200 activated alumina, Adsorption. 11 (2005) 65–75. doi:10.1007/s10450-005-1094-8.

[62] M. Hefti, M. Mazzotti, Modeling water vapor adsorption/desorption cycles, Adsorption. 20 (2014) 359–371. doi:10.1007/s10450-013-9573-9.

[63] M. Hefti, L. Joss, D. Marx, M. Mazzotti, An Experimental and Modeling Study of the Adsorption Equilibrium and Dynamics of Water Vapor on Activated Carbon, Ind. Eng. Chem. Res. 54 (2015) 12165–12176. doi:10.1021/acs.iecr.5b03445.

[64] Y.F. Shi, X.J. Liu, Heat and Mass Transport Characteristics of Pressure Swing Adsorption for the Removal of High-Level Moisture along with CO2from Air, Ind. Eng. Chem. Res. 57 (2018) 6464–6476. doi:10.1021/acs.iecr.8b00601.

[65] I. Park, K.S. Knaebel, Adsorption breakthrough behavior: Unusual effects and possible causes, AIChE J. 38 (1992) 660–670. doi:10.1002/aic.690380504.

[66] R.B. Anderson, Modifications of the Brunuaer, Emmet and Teller equations, Am. Chem. Soc. 68 (1946) 686–691. https://pubs.acs.org/doi/pdf/10.1021/ja01208a049.

[67] K. Morishige, N. Tarui, Capillary condensation of nitrogen in ordered mesoporous silica with bicontinuous gyroid structure, J. Phys. Chem. C. 111 (2007) 280–285. doi:10.1021/jp064946s.

[68] A.H. Wootters, R.B. Hallock, Hysteretic Behavior of Superfluid Helium in Anopore, J. Low Temp. Phys. 121 (2000) 549–554. doi:10.1023/A:1017599024229.

[69] R.B. Anderson, Modifications of the Brunuaer, Emmet and Teller equations, Am. Chem. Soc. 68 (1946) 686–691.

[70] S. Brunauer, J. Skalny, E.E. Bodor, Adsorption on nonporous solids, J. Colloid Interface Sci. 30 (1969) 546–552. doi:10.1016/0021-9797(69)90423-8.

[71] J.J. Fripiat, L. Gatineau, H. Van Damme, Multilayer physical adsorption on fractal surfaces, Langmuir. 2 (1986) 562–567. doi:10.1021/la00071a006.

[72] S. Brunauer, L.S. Deming, W.E. Deming, E. Teller, On a Theory of the van der Waals Adsorption of Gases, J. Am. Chem. Soc. 62 (1940) 1723–1732. doi:10.1021/ja01864a025.

[73] R.S. Schechter, W.H. Wade, J.A. Wingrave, Sorption isotherm hysteresis and turbidity phenomena in mesoporous media, J. Colloid Interface Sci. 59 (1977) 7–23. doi:10.1016/0021-9797(77)90333-2.

[74] D.D. Do, H.D. Do, Model for water adsorption in activated carbon, Carbon N. Y. 38 (2000) 767–773. doi:10.1016/S0008-6223(99)00159-1.

[75] M. Parlar, Y.C. Yortsos, Percolation theory of vapor adsorption-desorption processes in porous materials, J. Colloid Interface Sci. 124 (1988) 162–176. doi:10.1016/0021-9797(88)90337-2.

[76] M. Parlar, Y.C. Yortsos, Nucleation and pore geometry effects in capillary desorption processes in porous media, J. Colloid Interface Sci. 132 (1989) 425–443. doi:10.1016/0021-9797(89)90257-9.

[77] G. Mason, The Effect of Pore-Space Connectivity on the Hysteresis of Capillary Condensation in Adsorption Desorption Isotherms, Journal.of.Colloid and.Interface Sci. 88 (1982) 36–46. doi:10.1016/0021-9797(82)90153-9.

[78] G. Mason, A Model of Adsorption-Desorption Hysteresis in which Hysteresis is Primarily Developed by the Interconnections in a Network of Pores, Proc. R. Soc. A Math. Phys. Eng. Sci. 390 (1983) 47–72. doi:10.1098/rspa.1983.0122.

[79] G. Mason, Determination of the pore-size distributions and pore-space interconnectivity of Vycor porous glass from adsorption-desorption hysteresis capillary condensation, Proc. R. Soc. London. Ser. A. 415 (1988) 453–486. doi:10.3978/j.issn.1000-9604.2015.06.01.

[80] H. Liu, L. Zhang, N.A. Seaton, Analysis of sorption hysteresis in mesoporous solids using a pore network model, J. Colloid Interface Sci. 156 (1993) 285–293. doi:10.1006/jcis.1993.1113.

[81] A. V Neimark, Percolation Theory, (1991) 67–74. doi:10.1007/978-3-662-02403-4_5.

[82] H. Liu, L. Zhang, N.A. Seaton, Determination of the connectivity of porous solids from nitrogen sorption measurements - II. Generalisation, Chem. Eng. Sci. 47 (1992) 4393–4404. doi:10.1016/0009-2509(92)85117-T.

[83] L. Sarkisov, P.A. Monson, Modeling of adsorption and desorption in pores of simple geometry using molecular dynamics, Langmuir. 17 (2001) 7600–7604. doi:10.1021/la015521u.

[84] P.I. Ravikovitch, A. V. Neimark, Experimental confirmation of different mechanisms of evaporation from ink-bottle type pores: Equilibrium, pore blocking, and cavitation, Langmuir. 18 (2002) 9830–9837. doi:10.1021/la026140z.

[85] Quantachrome, Quantachrome Instruments Monosorb, (1999) 1. http://www.quantachrome.com/technical/dft.html (accessed October 22, 2018).

[86] S. Brandani, D.M. Ruthven, Moments Analysis of the Zero Length Column Method, Ind. Eng. Chem. Res. 35 (1996) 315–319. doi:10.1021/ie950287m.

[87] L. Liu, S. (Johnathan) Tan, T. Horikawa, D.D. Do, D. Nicholson, J. Liu, Water adsorption on carbon - A review, Adv. Colloid Interface Sci. 250 (2017) 64–78. doi:10.1016/j.cis.2017.10.002.

[88] A.M. Ribeiro, T.P. Sauer, C.A. Grande, R.F.P.M. Moreira, J.M. Loureiro, A.E. Rodrigues, Adsorption Equilibrium and Kinetics of Water Vapor on Different Adsorbents, Ind. Eng. Chem. Res. 47 (2008) 7019–7026. doi:10.1021/ie701732x.

[89] T.G. Glover, Y. Wang, M.D. Le Van, Diffusion of condensable vapors in single adsorbent particles measured via concentration-swing frequency response, Langmuir. 24 (2008) 13406–13413. doi:10.1021/la802222r.

[90] D.N. Jaguste, S.K. Bhatia, Combined surface and viscous flow of condensable vapor in porous media, Chem. Eng. Sci. 50 (1995) 167–182. doi:10.1016/0009-2509(94)00226-H.

[91] H. Rhim, S. tak Hwang, Transport of capillary condensate, J. Colloid Interface Sci. 52 (1975) 174–181. doi:10.1016/0021-9797(75)90314-8.

[92] H. Tamon, M. Okazaki, R. Toei, Flow mechanism of adsorbate through porous media in presence of capillary condensation, AIChE J. 27 (1981) 271–277. doi:10.1002/aic.690270214.

[93] J.M. Haynes, R.J.L. Miller, Surface diffusion and viscous flow during capillary condensation, Elsevier Scientific Publishing Company, 1982. doi:10.1016/S0167-2991(09)61360-4.

[94] T.-F. Lin, J.C. Little, W.W. Nazaroff, Transport and Sorption of Organic Gases in Activated Carbon, J. Environ. Eng. 122 (1996) 169–175. doi:10.1061/(ASCE)0733-9372(1996)122:3(169).

[95] M. Šoóš, P. Rajniak, F. Štěpánek, Percolation models of adsorption-desorption equilibria and kinetics for systems with hysteresis, Colloids Surfaces A Physicochem. Eng. Asp. 300 (2007) 191–203. doi:10.1016/j.colsurfa.2006.10.056.

[96] P. Rajniak, M. Soós, R.T. Yang, Unified network model for adsorption-desorption in systems with hysteresis, AIChE J. 45 (1999) 735–750. doi:10.1002/aic.690450409.

[97] D.M. Ruthven, Principles of Adsorption and Adsorption Processes, Wiley, 1984. https://books.google.co.uk/books?id=u7wq21njR3UC.

[98] J. Kärger, D.M. Ruthven, D.N. Theodorou, Diffusion in Nanoporous Materials, Copyright © 2012 Wiley-VCH Verlag GmbH & Co. KGaA, Weinheim, Germany, 2012. doi:10.1002/9783527651276.

[99] C. Chmelik, J. Kärger, The predictive power of classical transition state theory revealed in diffusion studies with MOF ZIF-8, Microporous Mesoporous Mater. 225 (2016) 128–132. doi:10.1016/j.micromeso.2015.11.051.

[100] S. Brandani, C. Cavalcante, A. Guimaraes, D.M. Ruthven, Heat Effects in ZLC Experiments, Adsorption. 4 (1998) 275–285. doi:Doi 10.1023/A:1008837801299.

[101] A. Chakraborty, B.B. Saha, S. Koyama, K.C. Ng, K. Srinivasan, Adsorption thermodynamics of silica gel-water systems, J. Chem. Eng. Data. 54 (2009) 448–452. doi:10.1021/je800458k.

[102] F.A. Schwertz, J.E. Brow, Diffusivity of water vapor in some common gases, J. Chem. Phys. 19 (1951) 640–646. doi:10.1063/1.1748306.

14 Conferences

SCCS Conference 2015, Edinburgh, UK

ETP Conference 2015, Glasgow, UK

ETP Conference 2016, Aberdeen, UK

ETP Conference 2017, Edinburgh, UK

AICHE Meeting 2017, Minneapolis, USA

PSE Forum 2018, London, UK

AICHE Meeting 2018, Pittsburgh, USA (not attended)

CPM-8, Delray Beach, USA (not attended)

15 Publications

L. Sarkisov, A. Centineo, S. Brandani, Molecular simulation and experiments of water adsorption in a high surface area activated carbon: Hysteresis, scanning curves and spatial organization of water clusters, Carbon N. Y. 118 (2017) 127–138. doi:10.1016/j.carbon.2017.03.044.

A. Centineo, H. G. T. Nguyen, Laura Espinal, J. C. Horn, S. Brandani, An experimental and modelling study of water vapour adsorption on SBA-15, Microporous Mesoporous Mater., **(Submitted)**

A. Centineo, S. Brandani, The innovative application of the ZLC technique for the measurement of water vapour adsorption isotherms on SBA-15 at high relative humidity, Ind. Eng. Chem. Res, **(Submitted)**